8-18-2015

Low Thermal Conductivity YSZ-based Thermal Barrier Coatings with Enhanced CMAS Resistance

Chen Jiang
University of Connecticut - Storrs, chenjiang.chn@gmail.com

Low Thermal Conductivity YSZ-based

Thermal Barrier Coatings with Enhanced CMAS Resistance

Chen Jiang, Ph.D.

University of Connecticut, 2015

Advanced thermal barrier coatings (TBC) are crucial to improved energy efficiency in next generation gas turbine engines. The use of traditional topcoat materials, e.g. yttria-stabilized zirconia (YSZ), is limited at elevated temperatures due to (i) the accelerated undesirable phase transformations, and (ii) high temperature corrosive attacks from calcium-magnesium-aluminum-silicate (CMAS) deposits and moisture.

In this research, the Solution Precursor Plasma Spray (SPPS) process was employed first to further reduce the thermal conductivity of conventional YSZ TBCs by introducing a microstructural feature of layered porosity, called the inter-pass boundaries (IPBs), that disrupts heat conduction in the coatings. Process optimization involving extensive scanning electron microscopy (SEM) characterization and laser-flash measurements on hundreds of spray trials, yielded a thermal conductivity as low as 0.623 $W \cdot m^{-1}K^{-1}$ in SPPS YSZ TBCs, which equated an approximately 50% reduction than the standard air-plasma-sprayed (APS) TBCs. At the same time, other engine critical properties of the low thermal conductivity SPPS TBCs, such as cyclic durability, erosion resistance and sintering resistance, were characterized to be equivalent or better than the APS baselines.

To enhance the high temperature capability of SPPS TBCs, modifications were introduced to the SPPS YSZ TBCs so as to improve their resistance to CMAS and moisture under harsh IGCC

environments. Several mitigation approaches were explored, including doping the coatings with Al_2O_3 and TiO_2, applying a CMAS infiltration-inhibiting surface layer, and filling topcoat cracks with blocking substances. The efficacy of these modifications on CMAS resistance was assessed with a set of novel CMAS-TBC interaction tests, while the moisture resistance was evaluated in a custom-built high-temperature moisture rig.

In the end, the optimal coating system was evaluated to be consisted of a thick inner layer of SPPS YSZ having the low thermal conductivity, and a high-temperature stable CMAS resistant gadolinium zirconate (GZO) protective surface layer made by the SPPS process. Noteworthy was the fact that the YSZ to GZO interface made by the SPPS process was not the failure location as had been observed in similar APS TBCs.

Low Thermal Conductivity YSZ-based

Thermal Barrier Coatings with Enhanced CMAS Resistance

Chen Jiang

B.S., Beijing Institute of Technology, 2010

A Dissertation

Submitted in Partial Fulfillment of the

Requirements for the Degree of

Doctor of Philosophy

at the

University of Connecticut

2015

APPROVAL PAGE

Doctor of Philosophy Dissertation

Low Thermal Conductivity YSZ-based Thermal Barrier Coatings with Enhanced CMAS Resistance

Presented by

Chen Jiang, B.S.

Major Advisor _____

Eric H. Jordan

Associate Advisor _____

Maurice Gell

Associate Advisor _____

Mark Aindow

University of Connecticut

2015

PREFACE

This thesis serves as the documentation of my study during fall 2011 to fall 2014 in the Department of Materials Science and Engineering at Institute of Materials Science, University of Connecticut. This work is supported by US Department of Energy National Energy Technology Lab under the Award DE-FE-0007382, *Low Thermal Conductivity, and High Durability Thermal Barrier Coatings for IGCC Environments*.

Part of the work is accepted for journal publications in the following:

EH Jordan, **C Jiang**, J Roth and M Gell, "Low Thermal Conductivity Yttria-Stabilized Zirconia Thermal Barrier Coatings Using the Solution Precursor Plasma Spray Process," *Journal of Thermal Spray Technology* **23** (2014), pp 849-859 [*Journal of Thermal Spray Technology* Volume 23 Best Paper Award]

EH Jordan, **C Jiang**, M Gell and J Roth, "Low Thermal Conductivity YSZ Thermal Barrier Coatings Made by the Solution Precursor Plasma Spray Process," *ASME Turbo Expo 2014: Turbine Technical Conference and Exposition* **6** (2014), pp V006T02A005, Düsseldorf Germany, June 16–20

C Jiang, EH Jordan, AB Harris, M Gell and J Roth, "Double-layer Gadolinium Zircornate/ Yttria-Stabilized Zirconia Thermal Barrier Coatings Deposited by the Solution Precursor Plasma Spray Process", *Journal of Thermal Spray Technology* **24** (2015), pp 895-906

ACKNOWLEGEMENTS

First, I'd like to express my sincere gratitude to Prof. Eric H. Jordan, my major advisor, for having supported me from the very beginning and trusted me with several projects. It's been really fortunate for me to work with such a knowledgeable and innovative mentor over the past five years, by whom I've been constantly inspired to become a better researcher. I'd also like to extend the profound thanks to my associate advisors, Prof. Maurice Gell and Prof. Mark Aindow, without whose valuable time and expertise the accomplishment of this study would not be possible. Special appreciation goes to Mr. Jeff Roth, our beloved thermal spray technician. Words can't express what it meant to an international student, when he voluntarily helped me out of many difficulties both in and outside the work, and warmly welcomed me to his beautiful house and lovely family. He is a true friend who I will always cherish.

The success of each member in the Institute of Materials Science depends on the hard work of others, since we all are a cooperative team. For this, I'd like to thank Dr. Lichun Zhang, Dr. Roger Ristau, Dr. Jack Gromek, Dr. Laura Pinatti, Mr. Gary Lavigne and Dr. Richard Perez Moyet for their professional assistance with the lab instrumentation, which in many cases was critical to my research. In addition, the indispensable administrative work of all IMS/MSE staff is also greatly appreciated.

Besides, I'd like to acknowledge all present and previous group members for making the past five years of mine a pleasant journey: Mr. Alan H. Harris, Mr. Rishi Kumar, Dr. Jiwen Wang, Dr. Chigozie K. Muoto, Dr. Jacquelynn M. Garofano, Dr. Wen Ma, Mr. Mike DiRe, Dr. Shayan Ahmadian, Mr. Nirav Patel, Mr. Jordan Parley, Mr. Noveen Delaram, Ms. Rheanna Ward and Mr. Wiesio Kapalczynski. As Confucius once said, *when I walk along with two others, they may always serve as my teachers*, what I've learned from each of you will be my valuable knowledge

as well! Furthermore, I'd like to deliver my special acknowledgement to all UConn *Keramos* Chapter founding members, Ms. Sapna Gupta, Mr. Alan B. Harris, Mr. Austin McDannald, Mr. Nasser Khakpash and Prof. Prabhakar Singh. Looking back at where we first started, I'm impressed by what we've accomplished in only two years, and am proud to be among this supportive group to witness this gratifying growth.

Finally, I will dedicate this thesis to my family. The unconditional love of my grandparents has made me who I am, and I always feel stronger knowing they all have great faith in me. I'd also like to thank my dad, Min-Ning Jiang, and mom, Hui-Ying Shen, for making all of this possible. I understand it was hard not to be strict parents when competition had imposed such significant peer pressure to all of us. Nonetheless, I'm grateful for what I've learned in the early years, and the rewards it has brought ever since!

TABLE OF CONTENTS

LIST OF FIGURES

LIST OF TABLES

LIST OF ABBREVIATIONS

APS	Air Plasma Spray
CMAS	Calcium-Magnesium-Aluminosilicate
DI	Deionized
DSC	Differential Scanning Calorimetry
DVC	Dense Vertically-Cracked
EB-PVD	Electron-beam Physical Vapor Deposition
EDS	Energy Dispersive X-ray Spectroscopy
FEA	Finite Element Analysis
FOD	Foreign Object Damage
GZO	Gadolinium Zirconate
HVOF	High Velocity Oxygen Fuel
IGCC	Integrated Gasification Combined Cycle
IPB	Inter-pass Boundaries
LFA	Laser-flash Analysis
LMP	Larson-Miller Parameter
LPPS	Low Pressure Plasma Spray
OEM	Original Equipment Manufacturer
PSL	Protective Surface Layer
SEM	Scanning Electron Microscopy
SPPS	Solution Precursor Plasma Spray
SPS	Suspension Plasma Spray
TBC	Thermal Barrier Coating
TEM	Transmission Electron Microscopy
TGA	Thermogravimetric Analysis
TGO	Thermally Grown Oxide
UConn	University of Connecticut
XRD	X-ray Diffraction
YSZ	Yttria-stabilized Zirconia

LIST OF SYMBOLS

Symbols

Nu	Nusselt Number
Oh	Ohnesorge Number
Re	Reynold Number
Sh	Sherwood Number
St	Stokes Number
We	Webber Number
Z'	Dimensionless Number
B_M	Spalding Mass Transfer Number
B_T	Spalding Heat Transfer Number
OOF	Finite Element Analysis Software
a, b	Sides of a square piece
c	Cubic
c_d	Drag Coefficient
C_p	Specific Heat
d	Diameter
D	Mass Diffusivity
g	Small Depth into Planar Solids
h	Heat Transfer Coefficient
k_c	Boltzmann Constant
K	Thermal Conductivity
K^*	Normalized Thermal Conductivity
l	Thickness
L	Latent Heat
m	Monoclinic
$\dot{m}$	Mass Flow Rate
Q	Radiant Heat
$\dot{Q}$	Heat Transfer Rate
t	Time
t/t'	Tetragonal/Tetragonal Prime
$t_{o.5}$	Time for Reaching 50% Maximum Temperature
T	Temperature
v	Velocity
α	Thermal Diffusivity
μ	Dynamic Viscosity
ρ	Density
σ	Surface Tension
χ	Mass Fraction
C, n, V, ω	Designated Coefficients

Subscripts

o	Original
g	Gas Phase
l	Liquid Phase
M	Maximum
p	Particle
s	At the Surface
∞	Far Field
ax	Axial
BL	Flow Boundary Layer
tr	Transverse
pl	Plasma

Chapter 1. Introduction, Background and Objectives

1.1 Introduction

The primary goal of this research is to develop optimal thermal barrier coatings (TBCs) for the advanced Integrated Gasification Combined Cycle (IGCC) power plants. IGCC (**Fig. 1-1**) is a sophisticated technology that employs the gasification processes to convert coal into a syngas (synthetic gas, composed primarily of CO and H_2), and generates electricity from the subsequent combined-cycle power process utilizing that syngas [1]. Impurities in the raw coal, such as sulfur and mercury, are typically removed and recycled prior to the combustion process so that the emission of environmental hazards is minimized. The harvest of the energy is realized through multiple gas and steam turbine engines, in which the dissipated heat is also collected rendering a more efficient energy conversion. Gas turbine engines, being the core component for the IGCC power generation as well as the aircraft propulsion, have thereby seen a growing demand for technology advancement over the recent years, in terms of higher engine operating temperatures, improved efficiency and enhanced corrosion resistance [2, 3].

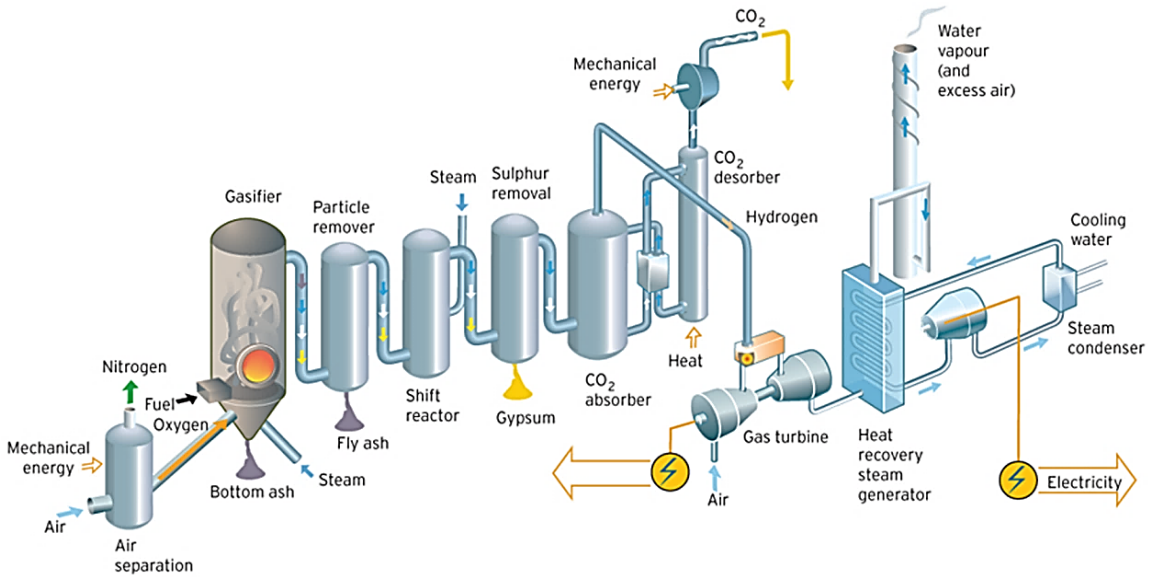

Fig. 1-1 A typical IGCC process [4]

Gas turbine engines are basically Carnot engines, and their efficiency and the core power are directly determined by the gas temperature entering the turbine section [3]. Tremendous efforts have been dedicated in the past few decades to improved engine efficiency, and remarkable increases in engine operating temperatures (**Fig. 1-2**) were achieved through three major breakthroughs [5, 6]:

(i) The discovery of new superalloy compositions that exhibit enhanced creep and oxidation resistance;

(ii) The state-of-art fabrication technology for large single-crystal superalloy components with intricate internal cooling designs; and

(iii)The implementation of advanced TBCs.

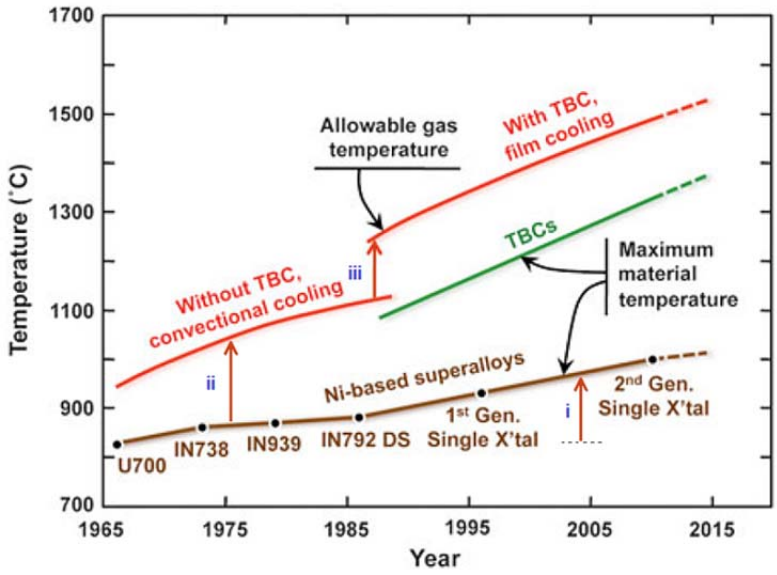

Fig. 1-2 Progression of temperature capabilities of Ni-based super-alloys and thermal barrier coating (TBC) materials over the past 50 years [3]

The first focus of this thesis is to improve the current TBC system by further reducing its thermal conductivity (Chapter 3). This is to be achieved by an extensive microstructure optimization

using a novel Solution Precursor Plasma Spray process. Then the high temperature corrosion issue of TBCs is to be addressed through the exploration of several mitigation methods (Chapters 4-6). The evaluation of all modified SPPS YSZ-based TBCs is later performed with different experimental setups (Chapters 7-8). The results are carefully studied and utilized in the selection of an optimized TBC for the IGCC environments (Chapter 9), with specific emphases on the resistance to both CMAS and high temperature moisture.

1.2 Background

1.2.1 Thermal barrier coatings

The most recent increases in the operating temperatures of turbine engines were enabled by the deposition of the multi-layer multi-functional TBCs [7, 8]. TBCs (**Fig. 1-3**), consisting of a thermal-insulating ceramic top layer, an aluminum-rich metallic bond-coat and a thermally-grown oxide (TGO) layer, are routinely employed on internally-cooled metallic gas turbine components to prevent the underlying materials experiencing extreme temperatures. An up to 300^{o}C temperature drop can be achieved across all TBC layers, depending on the chemistry, microstructure, and processing details for each individual layer [9, 10].

1.2.1.1 Bond-coat layer

The application of the so-called bond-coat layer (**Fig. 1-3**) on the alloy components was originally introduced in the TBC development stage to enhance the bonding between substrates and ceramic topcoats, and thus to obtain viable coatings that remained adherent upon high temperature exposures [5]. However, later studies suggested that the improved adherence was more likely to be the result of an increased high temperature oxidation/corrosion resistance from the formation of a thin TGO layer at the ceramic to bond-coat interface [11] than the

strengthened bonding between the deposited topcoat and the underlying alloy. Over the course of time, a consensus on good metallic bond-coats has been reached that in addition to enhanced bonding, they should also be capable of forming a protective, stable and slow-growing oxide layer to prevent the alloy from oxidative attacks, while maintaining sufficient morphological stability to minimize the occurrence of any interface defects. Two major classes of bond-coat alloys have thereby developed, namely the platinum-modified nickel aluminide (PtNiAl) and the MCrAlY alloys (M=Co, Ni, Fe or any combination [12, 13, 14, 15]), the selection of which is primarily determined by the prior use before the deposition of ceramic topcoats, for either oxidation or corrosion resistance purposes.

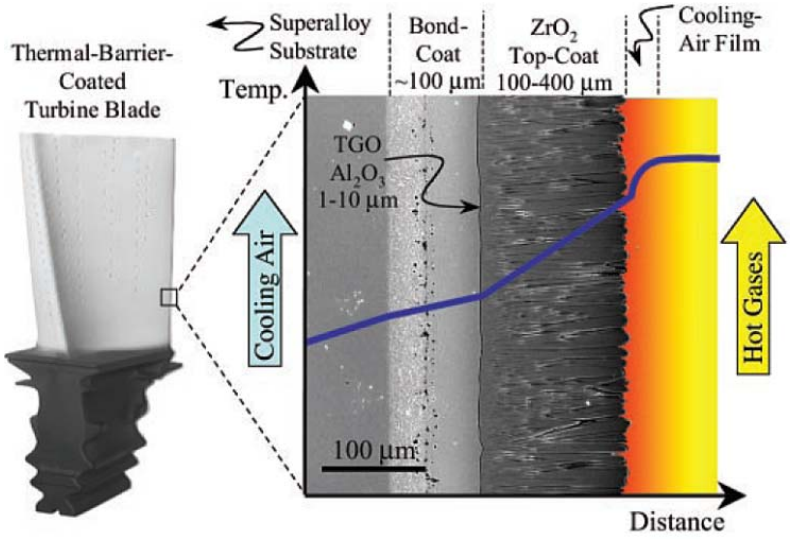

Fig. 1-3 Cross-section of the thermal barrier coating applied on a gas-turbine blade [9]

1.2.1.2 TGO layer

Regardless of bond-coat compositions, an α-Al_2O_3 TGO layer is always formed during high temperature exposures on advanced metallic bond-coat alloys. This is a crucial feature for the stability of TBC systems, because: (i) Al_2O_3 is more thermodynamically phase compatible with the current topcoat material, YSZ, than any other possible oxide formations, e.g. nickel oxide,

nickel-chromium spinel or chromium oxide [16]; (ii) the very low oxygen diffusivity of Al_2O_3 [17] is critical for achieving a suppressed high-temperature oxide growth and a minimal morphology change of the bond-coat interface over a long term, which in return improves TBC durability, providing zirconia itself is a fast-ion oxygen conductor.

1.2.1.3 Topcoat layer

The ceramic topcoat (**Fig. 1-3**), which is primarily made of refractory oxide, is responsible for nearly all the temperature reduction among all TBC layers. The requirements on the physical properties of topcoat materials are exceptionally demanding [5], so that a reliable performance in the harsh engine environments can be ensured. Generally speaking, a topcoat material should demonstrate:

(i) A low thermal conductivity from room temperatures to designated operating temperatures,
(ii) Capability of accommodating the strains associated with the thermal expansion mismatch between different layers of materials,
(iii) Thermodynamic compatibility with the TGO layer,
(iv) Phase stability up to the maximum operating temperature,
(v) High erosion resistance and
(vi) Resistance to various corrosive attacks, especially of the moisture and airborne species that are common in IGCC environments.

Currently, the material of choice for TBC topcoats is yttria-stabilized zirconia (YSZ), as it exhibits a combination of several attractive properties including the relatively comparable thermal expansion coefficient to base metals, exceptionally high fracture toughness and relatively low thermal conductivity.

1.2.1.4 Failure mechanisms

In light of the complicated nature of the TBC system and the harsh environments it applies to, understanding TBC failure mechanisms and predicting the service lifetime is not straightforward, yet the endeavor can nevertheless provide considerable insight into producing advanced TBCs systems for higher operating temperatures. Substantial experimental evidence has indicated that many TBC failures are related to the oxidation of the bond-coat alloy [18], therefore critical TGO thickness and aluminum depletion in the bond-coat are occasionally employed for TBC life prediction. However, these models can't explain the broad life distribution of TBCs under the same cyclic conditions, especially when TGO of some samples haven't even reached their critical values yet. Providing the prevailing mode of TBC failure is observed to be coating buckling/spallation [19], bond-coat surface imperfections, namely surface roughening, are considered to be another factor leading to the nucleation of interface separation and TBC failures. Many mechanisms have been proposed to explain the observed surface roughening, such as the *ratcheting* phenomenon caused by the lateral compressive stress associated with the TGO growth under thermal cyclic conditions [20], and the surface displacement associated with aluminum-depletion-induced volumetric changes [21]. Other works [22, 23] have also suggested that the void formation in the bond-coat layer over an extended service time could cause superposed features on its interface, rendering the TBC spallation. These failure mechanisms characterized by the strain misfits within TBC constituent materials are generally called the TBC *intrinsic* failure mechanisms, while other factors, such as foreign object damage (FOD) and molten deposits (to be discussed later), can also lead to the occurrence of the failed performance and are categorized as the *external* mechanisms [24]. All TBC failure mechanisms identified up-to-date are illustrated in **Fig. 1-4** on an EB-PVD TBC system.

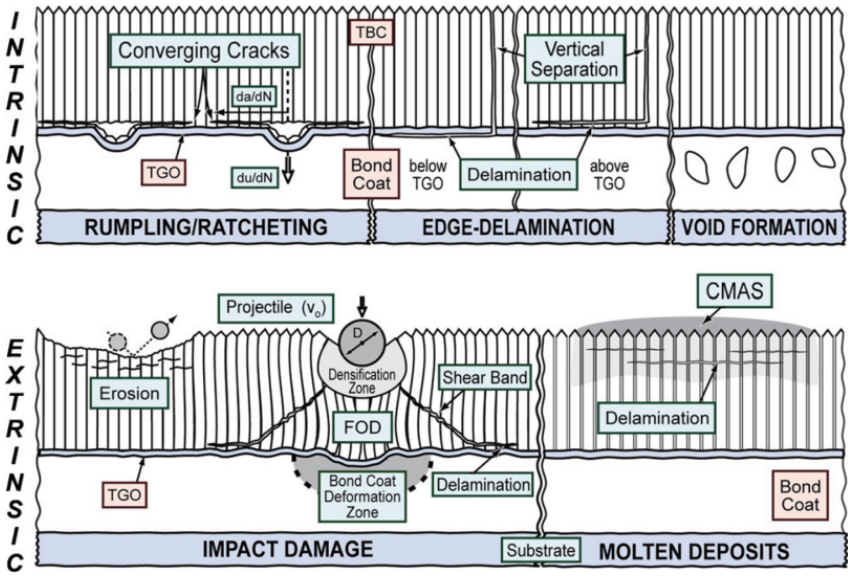

Fig. 1-4 A summary of current TBC failure mechanisms [24]

1.2.2 Challenges for advanced TBC ceramic topcoats

1.2.2.1 Temperature limitation

In current YSZ topcoats, the 6-8wt% yttria content is capable of inhibiting the detrimental *t-m* phase transformation that leads to ~4% volumetric change and crack formation, by stabilizing a metastable non-transformable *t'* phrase of zirconia. Besides, 6-8wt% YSZ exhibits exceptionally high facture toughness [25], which also contributes to the typically superior durability under thermal cycling [26]. But such stabilization has an upper temperature limit (~1200^{o}C [27]), above which the *t'* phase will still inevitably transform into a mixture of tetragonal and cubic phases due to an accelerated diffusion [28, 29]. In addition, the poor sintering performance of current YSZ TBCs restricts their applications at elevated temperatures, because (i) the elastic modulus of the topcoat increases as the densification occurs, leading to the loss of strain tolerance, and (ii) the low thermal conductivity is compromised as the porosity volume faction decreases.

1.2.2.2 Corrosion limitation

New degradation modes emerge on TBCs at elevated operating temperatures as well. Airborne particles (e.g. sand, dust, volcanic ashes, runway debris), though constituting only a tiny volumetric faction of ingested air, can produce a significant amount of deposit accumulation in gas turbine engines over the time. In some special turbine engines that either utilize *dirty* fuels or face harsh service environments (e.g. deserts), the significant amount of accumulation of environmental deposits has caused imminent challenges. When the operating temperatures are *cooler*, these ingested particles in the turbine engines may bounce off coating surfaces causing erosion damages (FOD), which have already been remedied by the advanced coating processing techniques and the adoption of erosion-resistant materials, YSZ being the most common choice. However, under *hotter* conditions, these accumulated environmental deposits can form a eutectic molten glass, namely the calcium-magnesium-aluminosilicate (CMAS), that sticks to coating surfaces, penetrates the microstructure and attacks TBCs leading to premature failures [30, 31, 32] (**Fig. 1-4**). The molten CMAS fills in all topcoat cracks, and increases TBCs' stiffness upon cooling, costing the mechanical strain tolerance of the coatings. In the case of YSZ TBCs, CMAS is also known to attack the ceramic topcoat chemically through a dissolution-reprecipitation process that literally *extracts* yttria stabilizer into the glass melt, and triggers the undesirable *t-m* phase transformation in the re-precipitated zirconia (**Fig. 1-5**). Studies on mitigation methods for CMAS attacks have thereby drawn an increasing amount of attention, thanks to the growing demand for hotter and more efficient engines.

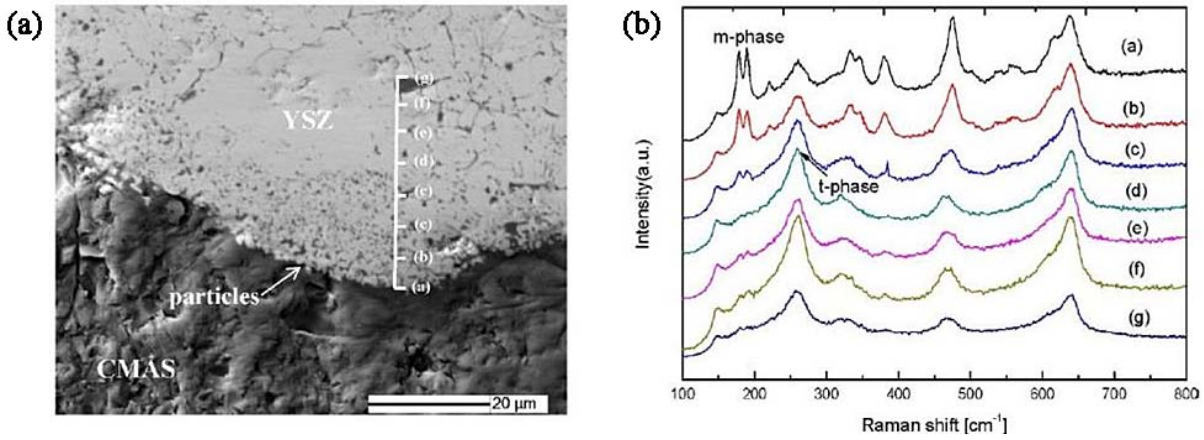

Fig. 1-5 The interaction between YSZ TBC and CMAS deposits [33]

1.2.3 Alternative topcoat materials

1.2.3.1 Improving high temperature capability

In order to obtain an advanced TBC system that better suits the hotter engine environment, many alternative topcoat materials have been studied. Spinel ($MgAl_2O_4$) [27] and perovskite ($SrZrO_3$) [34, 35] have known high melting points, which can help to maintain a reliable mechanical performance and alleviate sintering issues at elevated temperatures. Rare-earth zirconate pyrochlores (e.g. $La_2Zr_2O_7$, $Gd_2Zr_2O_7$ and $Nd_2Zr_2O_7$) have exhibited high temperature phase stability, and low thermal conductivity [36, 37], which will eliminate the concerns about the undesirable phase transformation in YSZ TBCs. Yttrium aluminum garnet ($Y_3Al_5O_{12}$) is another promising topcoat candidate material that has demonstrated much improved phase stability and cyclic durability in comparison to conventional YSZ TBCs [38, 39]. But in general, the thermal expansion coefficient mismatch of most alternative materials to the base metals (16×10^{-6} K^{-1} for alloy substrate and 17.5×10^{-6} K^{-1} for the NiCrAlY bond-coat [40]) is still large [41], which will contribute to greater thermal stresses and consequently inferior durability under thermal cyclic conditions. For some alternative materials, the low coating toughness is also found responsible

for poor erosion resistance [42]. Moreover, some compositions utilize as much as 50mol% rare-earth elements; in comparison YSZ, which contains only 7wt% (~4mol%) Y_2O_3, is more economically favorable.

1.2.3.2 Enhancing CMAS resistance

To alleviate the adverse effects of CMAS, different approaches involving modifications on topcoat material compositions have also been proposed to either (i) capture the molten environmental deposits by freezing it into crystalline phases, or (ii) form stable by-products with CMAS that blocks the pathways for further penetration. In both contexts, fast and effective inhibition reactions are considered to be one of the key factors. Therefore, the concept of optical basicity has been suggested in providing a quantitative chemical screening for CMAS-resistant topcoat compositions [43, 44]. Restricted by the number of qualified TBC topcoat materials though, few alternative material systems have actually been reported effective to enhance the TBC CMAS-resistance. The two most promising systems so far have been gadolinium zirconate [30] and Al_2O_3/TiO_2-doped YSZ [45], which correspond respectively to optical basicity values of 1.16 [43] and 0.83 [43, 44, 46] with respect to 0.49-0.75 of most CMAS compositions [43] indicating good reactivity. Gadolinium zirconate (GZO), being one of the low-thermal-conductivity rare-earth zirconates, was observed to form stable apatite silicate, $Ca_2RE_8(SiO_4)_6O_4$, upon the interaction with CMAS [47, 48], which is readily efficacious in blocking the further penetration pathways for CMAS. Considering the other appealing properties of rare-earth zirconates, gadolinium zirconate is currently considered to be the most effective CMAS-resistant system, and has seen extensive research as well as engine services [5, 30, 47, 49, 50, 51, 52, 53]. In Al_2O_3/TiO_2-doped YSZ TBCs, the metastable alumina solute in the zirconia solid solution was

engineered to shift the CMAS composition to the anorthite ($CaAl_2Si_2O_8$) fields in the ternary Al_2O_3-CaO-SiO_2 phase diagram, while TiO_2 acted as a nucleating agent allowing anorthite to quickly crystalize [54], thus froze the CMAS melt from further attacking. The direct benefit of doping Al_2O_3/TiO_2 in YSZ TBCs is the reduced usage of expensive rare-earth elements. Additionally, the YSZ-based matrix provides better erosion resistance, given the fracture toughness of GZO is comparatively lower [55].

1.2.4 Deposition techniques for ceramic topcoats

Another viable approach to obtaining suitable TBCs for elevated operating temperatures is to modify the conventional YSZ TBCs through structural and processing engineering, at the same time retaining the favorable properties of YSZ. Among all properties that can be further optimized, thermal conductivity is of great interest [56, 57]. Reduced thermal conductivity provides a greater temperature drop for a given coating thickness, which can translate to increased component durability [58], or a thinner coating for a given temperature drop, which translates to reduced weight (particularly important for high speed rotating parts) and reduced costs [59, 60]. It has been estimated that a 50% reduction in topcoat thermal conductivity would result in an approximately 55^{o}C temperature reduction on the base alloy, which would be equivalent to the high temperature capability improvements achieved over the span of 20 years through the developments of single-crystal superalloys [49].

At the moment, ceramic TBC topcoats are commercially deposited using two widely-adopted methods, either by the air plasma spray (APS) or the electron beam-physical vapor deposition (EB-PVD) processes (**Fig. 1-6**). In the APS process, premade particles are injected into the plasma jet, rapidly melted and accelerated into a stream of molten droplets, and then propelled

onto the substrates to form coatings. Experience has shown that the low inertia to surface force ratio of fine particles causes extreme difficulties in feeding the materials into the plasma jet, therefore only particles with larger sizes (usually 10-100 microns) are typically used for the APS process. Accordingly, the as-deposited coatings exhibit coarse microstructures, consisting of large dense splats and horizontal splat boundaries (**Fig. 1-6a**). Alternatively, by altering the deposition conditions, a dense vertically segmented microstructure can also be obtained, which provides improved topcoat tolerance to the strain caused by CTE mismatch between ceramic and metallic bond-coat. In general, the APS YSZ coatings can reach 80-86% theoretical density of the bulk material [11] and the resulted thermal conductivity of APS YSZ falls in the range of 0.8-1.7 $Wm^{-1}K^{-1}$ [61].

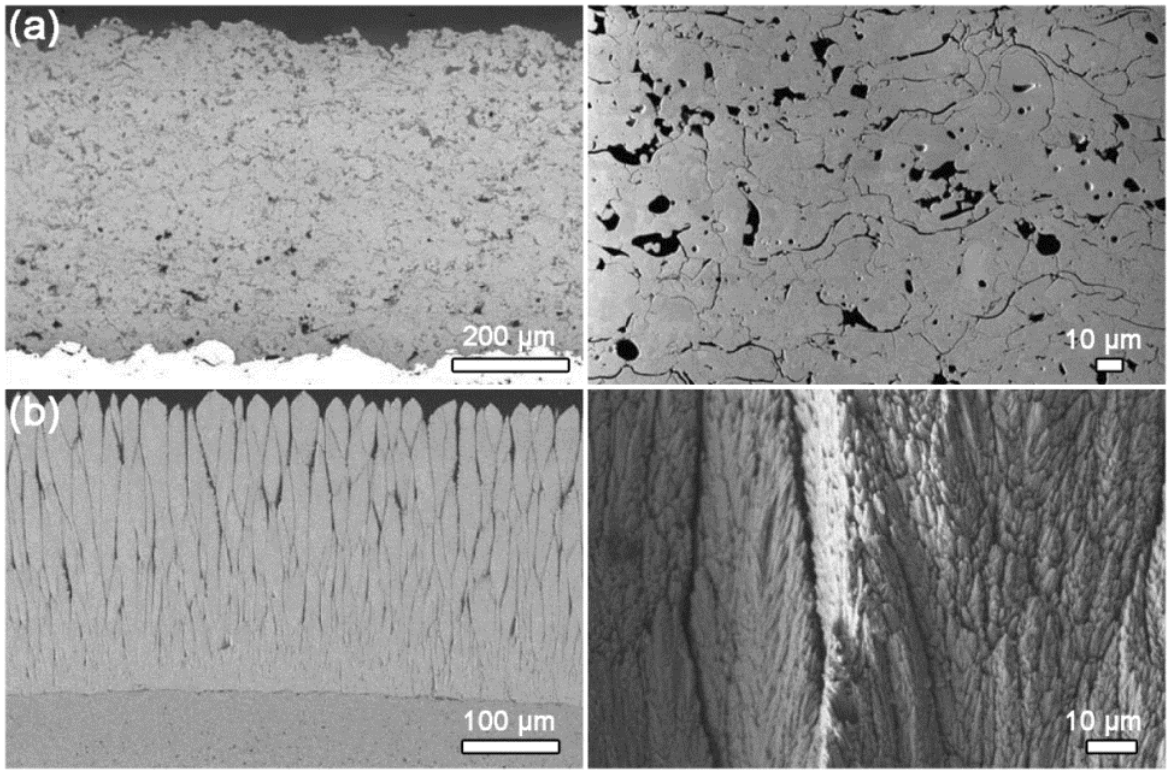

Fig. 1-6 (a) Cross-section of APS TBCs demonstrating the dense splats and the horizontal splat boundaries, and (b) the EB-PVD TBC featuring dense columnar grains and vertical channels [11]

As for the EB-PVD process, atoms ejected from the target anode are transferred in a gaseous phase under high vacuums, and directed onto the substrates forming desired coatings. Typical microstructures of EB-PVD TBCs are composed of ultra-dense columnar grains and fine vertical channels present in between [9] (**Fig. 1-6b**). With the absence of horizontal features that disrupt the heat flow, the thermal conductivity of EB-PVD YSZ topcoats is generally higher than their plasma-sprayed counterparts of the same composition, 1.5-2 $W \cdot m^{-1}K^{-1}$ [62], but the mechanical compliance is significantly improved due to the columnar microstructure.

Despite the popularity of the two TBC deposition techniques, APS and EB-PVD processes each possess certain disadvantages. For the APS process, the powder preparation often requires the tedious spray-drying procedures, and thereby any alteration of the powder chemistry typically costs tremendous development efforts. Furthermore, the dense horizontal splat microstructure provides no sufficient strain tolerance, and thus yields inferior durability performance during engine services. The APS dense vertically-cracked (DVC) coatings can improve strain tolerance, but such DVC microstructure can only be fabricated in relatively dense coatings (>88%) under exceptionally high processing temperatures [63], which in return limits its applicability. In the EB-PVD process, the coating deposition process rate is normally low, yet the equipment is expensive largely due to the high vacuum requirements. Therefore the EB-PVD process is more economically demanding compared to the APS process, or the thermal spraying in large.

1.2.5 The solution precursor plasma spray process

The Solution Precursor Plasma Spray (SPPS, **Fig. 1-7**) process is one of the recent variations in the conventional plasma spraying technology, and shares many characteristics with the common APS process. Unlike the APS process though, liquid precursor solutions made from various

organic/inorganic salts and solvents are used as the feedstock materials, rather than the premixed powders. This innovation enables the following intuitive benefits:

(i) Chemical homogeneity in the as-sprayed coatings is easily achievable, as the liquid precursor solutions allow the constituents chemicals to be mixed at a molecular level;

(ii) The ease of liquid solution preparation allows new coating compositions, as well as complex composite coatings, to be obtained quickly, avoiding the time-consuming spray-drying procedures for APS powders;

(iii) The complicated deposition characteristics in the SPPS process provide additional engineering opportunities for various beneficial microstructural features as well as new functionalities to be incorporated in the as-sprayed coatings.

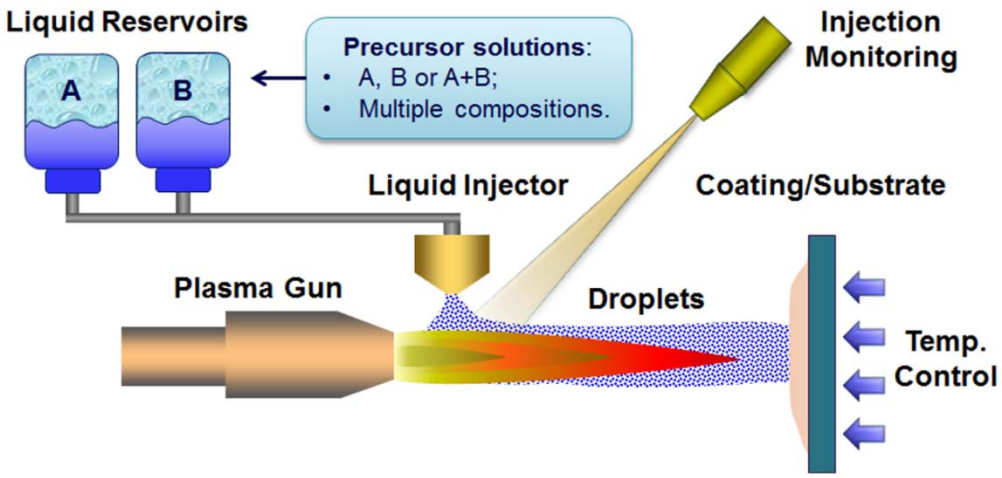

Fig. 1-7 A schematic illustration of the SPPS process

On the other hand, since the time-temperature history of each individual droplet in the plasma jet determines the nature of deposited particles [64], it's also expected to be rather challenging to manage the degree of pyrolysis in injected precursor droplets and to repeatedly produce desired microstructures. Numerous precedent efforts have been devoted to the characterization of this novel coating deposition technology and as a result spawned many invaluable insights.

1.2.5.1 Precursor solution

Generally speaking, solution viscosity, surface tension and density are relatively sensitive to the solute loading variation in precursor solutions, which would influence different aspects of the SPPS process. Besides, solutions typically reflect the fluid behavior of the solvent, e.g. retaining Newtonian fluid properties until the pyrolysis takes place [65]. In fact, solvents were found directly affecting the droplet pyrolysis, as the high surface tension and high boiling point solvent can cause incomplete liquid evaporation, leading to unpyrolyzed deposits [66]. In addition, the chemical reactions associated with the solute decomposition may introduce another perspective to particle-plasma interaction in the jet, in a sense that precursors exhibiting significant endothermic reactions in the early stages of heating can delay the particle melting event to the cooler downstream of the plasma jet. To mitigate this undesirable effect, addition of reactive chemicals has been proposed by Muoto et al [67] to alter the thermal characteristic of precursor pyrolysis.

1.2.5.2 Plasma torch

The thermal spray plasma guns (**Fig. 1-7**) are routinely used as the plasma spray heat source, in which an electrical arc is initiated between the cathode and anode by a high voltage discharge, energizing a mixture of gases to form a plasma jet. The plasma-forming (primary) gas, Ar, N_2 or the combination of the two, constitutes the most portion of the gas mixture, while the secondary gas, usually H_2 or He, adjusts the plasma thermal and electrical characteristics. By selecting the ratio and species in the primary/secondary gas combinations, the plasma conditions can be manipulated [68, 69], therefore affects the properties of as-deposited coatings directly.

1.2.5.3 Liquid delivery

The delivery of the precursor solutions to the injection nozzle is usually achieved by either a pressurized tank (**Fig. 1-7**) or a peristaltic pump [70] in the SPPS process. The pressurized tank provides an additional back pressure at the injection nozzle that is beneficial for the droplet break-up and entrainment. However, sometimes the feed rate in this case is rather sensitive to the fluid properties, and transporting highly viscous fluids is difficult. Peristaltic pumps, as a good substitution to the pressurized tanks, handle the slurries/shear-sensitive fluids effortlessly. Besides, a constant feed rate can also be easily maintained. The disadvantages though are the pulsating flow and potentially poor entrainment to the high-momentum plasma plume. The selection of the most suitable liquid delivery system largely depends on the precursor properties and equipment availability.

1.2.5.4 Precursor injection

In the SPPS process, the precursor injection can be performed either externally or internally. For the external injection, liquid precursors are usually atomized by compressed gas prior to the transverse injection into the plasma jet ([71], **Fig. 1-7**). Another possible external injection mode is to utilize a stream of the precursor solution [72], which can be instantaneously atomized at the contact of the transverse high-flow plasma gases. Ozturk et al showed that the droplets produced by a commercial atomizer exhibited an average size of 40μm with a narrow size distribution, and the droplets acquired sufficient momenta to fully penetrate into the hot plasma core [73]. From a quantitative perspective, droplet break-up during the precursor injection can be described by different dimensionless numbers, *Z'*, Weber number (*We*), Reynold number (*Re*) or Ohnesorge

number *(Oh*), depending on the injection mode and fluid properties (Newtonian or non-Newtonian to be specific) [65, 72]:

(i) Atomization injection (Newtonian fluid):

$$We \overset{\text{def}}{=} \frac{\text{Inertial forces}}{\text{Surface tension forces}} = \frac{\rho_g \times \left(v_g - v_l\right)^2 \times d_l}{\sigma_l} \qquad (1)$$

$$\begin{cases} 12 \leq We \leq 100, \text{vibratinal breakup} \\ 100 \leq We \leq 350, \text{stripping of liquid by shear stress} \\ We \geq 350, \text{catastrophic breakup} \end{cases}$$

(ii) Atomization injection (non-Newtonian fluid):

$$Oh \overset{\text{def}}{=} \frac{\text{Viscous forces}}{\text{Inertial and surface tenstion forces}} = \frac{\mu_l}{\sqrt{\rho_l \sigma_l d_l}} \qquad (2)$$

(iii)Stream injection:

$$Re \overset{\text{def}}{=} \frac{\text{Inertial forces}}{\text{Viscous forces}} = \frac{\rho_l d_l \left(v_l - v_g\right)}{\mu_l} \qquad (3)$$

$$Z' \overset{\text{def}}{=} \frac{\text{Viscous forces}}{\text{Surface tension forces}} = \frac{\sqrt{We}}{Re} \qquad (4)$$

Where ρ = density, v = velocity, d = droplet diameter, μ = dynamic viscosity and σ = surface tension (subscripts: g = gas, l = liquid). Extensive fragmentation can adversely affect the droplet entrainment into the plasma jet, for the injection forces imposed on the droplets are significantly reduced as the droplet volume and surface area decreases, and as a result, the droplet momentum can't match up to the momentum of the plasma jet, leading to the failure of droplet penetration into the plume. Therefore, the selection of the appropriate injection conditions is crucial to the

success of the SPPS process. As a reminder, a good entrainment scenario is generally characterized as $\rho_l v_l^2 \gg \rho_{pl} v_{pl}^2$ (pl = plasma) [74].

Given the challenges associated with the external injection of precursor solutions, an alternative approach of feeding precursor solution axially from the rear of the plasma gun has been considered [75, 76], and applications were typically found in the suspension plasma spray (SPS) process using the Northwest Mettech Axial III axial-feeding torch [77, 78], in which reasonably dense coatings were produced.

1.2.5.5 Droplet in-flight break-up, evaporation and precipitation

The injected precursor droplets generally undergo a sequence of transformations in the plasma plume, such as secondary droplet break-up, solvent evaporation, particle precipitation and pyrolysis, particle sintering and melting, and in some rare cases recrystallization, before impacting the substrate and forming a coating.

The drag force imposed on the injected precursor droplets by the plasma jet creates shear deformation of the droplet, leading to further atomization of the droplets, called the *secondary* or the *aerodynamic* break-up. Whether it be the vibrational [79] or the stripping breakup [80], the secondary break-up in the SPPS process is usually not observed directly; however, the size of in-flight particles collected by Bhatia et al were measured to be no more than 2μm, much smaller in comparison to the theoretical particle size of 8μm if only the primary atomization by the atomizing nozzle was present, and the average atomized droplet size was around 38μm, thereby confirming the existence of secondary break-up [81]. The dynamics of the droplets after the secondary break-up can be characterized by the equation of motion, with considerations of drag forces [82, 83]:

$$\text{Axial velocity: } \frac{\partial v_{ax}}{\partial t} = \frac{3c_d\rho_\infty}{8d_{l,s}\rho_l}\left|v_{ax,\infty} - v_{ax}\right|\left(v_{ax,\infty} - v_{ax}\right) \qquad (5)$$

$$\text{Transverse velocity: } \frac{\partial v_{tr}}{\partial t} = \frac{3c_d\rho_\infty}{8d_{l,s}\rho_l} v_{tr}^2 \qquad (6)$$

$$\text{Drag coefficient: } c_d = \frac{24}{Re(1 + B_M)} \qquad (7)$$

$$\text{Spalding mass transfer number: } B_M = \frac{\chi_{g,\infty} - \chi_{g,s}}{1 - \chi_{g,s}} \qquad (8)$$

Where c_d = drag coefficient and χ = mass fraction (subscripts: *ax* = axial, *tr* = transverse, ∞ = far field, *s* = at the droplet surface).

Three routes were then proposed by Basu et al. [84] as following that characterize the solvent evaporation and solid precipitation for the atomized droplets (**Fig. 1-8)**:

(a) Uniform solute concentration and precipitation in solution droplets leads to the formation of solid particles;

(b) The super-saturation of solute near the droplet surface leads to the formation of an inelastic shell, which can be either fragmented or not depending on the permeability of the shell. *Scenario I* corresponds to a low permeability shell that gets fragmented, while *Scenario II* corresponds to a high permeability shell that remains intact. The formation of an impermeable shell followed by internal heating and out-gassing is described in *Scenario III*.

(c) The super-saturation of solute near the droplet surface followed by the formation of elastic shell is simulated to be inflated and subsequently deflated by solid consolidation.

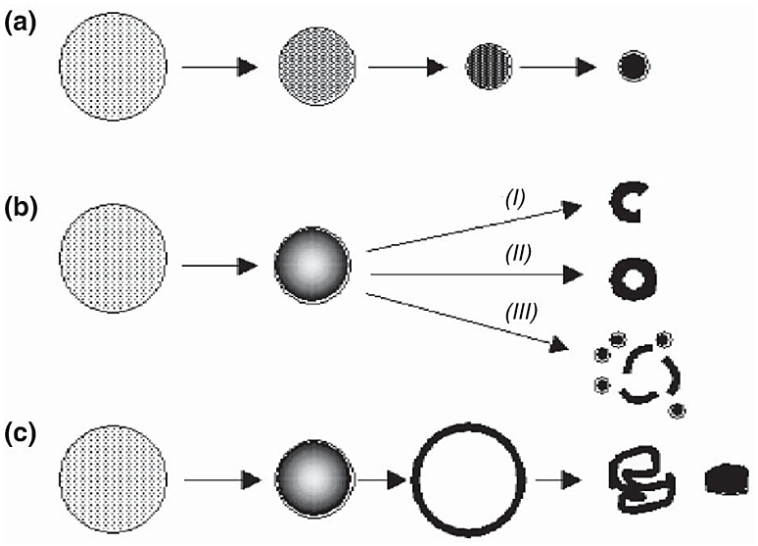

Fig. 1-8 Evaporation and precipitation routes for a solution droplet [84]

The droplet evaporation/precipitation can be quantitatively described with a cluster of equations [73]:

$$\text{Droplet radius change: } \frac{\partial d_l}{\partial t} = -\frac{\dot{m}}{4\pi\rho_l d_l^2} \qquad (9)$$

$$\text{The mass vaporization rate: } \dot{m} = 2\pi\rho_g D_g d_{l,s} Sh^* \ln(1 + B_M), \qquad (10)$$

$$\dot{m} = 2\pi \frac{K_g}{C_{p,gs}} d_{l,s} Nu^* \ln(1 + B_T) \qquad (11)$$

$$\text{Spalding heat transfer number: } B_T = C_{p,g} \frac{T_\infty - T_s}{L_l - \frac{\dot{Q}_l}{\dot{m}}} \qquad (12)$$

$$\text{Sherwood number: } Sh \stackrel{\text{def}}{=} \frac{\text{Mass diffusivity}}{\text{Molecular diffusivity}} = \frac{k_c d}{D} \qquad (13)$$

$$\text{Nusselt number: } Nu \stackrel{\text{def}}{=} \frac{\text{Total heat transfer}}{\text{Conductive heat tranfer}} = \frac{hd}{K} \qquad (14)$$

Where $\dot{m}$ = mass vaporization rate, D = diffusivity, C_p = heat capacity, $\dot{Q}$ = heat transfer rate, L = latent heat, k_c = Boltzmann constant, h = heat transfer coefficient and T = temperature. Unfortunately, the mass vaporization rate can't be solved directly from these equations as they ar3 coupled [75]. To fully solve this equation cluster, the Clausius-Clapeyron equation and Raoult's Law have to be supplemented, and droplet surface temperature as well as surface vapor concentration can be then calculated in addition to the mass vaporization rate. By utilizing the non-dimensional conservation equations of energy and chemical potentials, with the surface temperature and mass vaporization rate being the boundaries conditions, Ozturk et al. and Basu et al. have demonstrated that it is possible for the typical temperature and mass concentration profiles to be realistically simulated for individual in-flight precursor droplets, under various injection conditions [73, 75, 79, 84].

1.2.5.6 Particle trajectory

In-flight droplet break-up, precipitation and pyrolysis generate fine particles in the plasma jet, and the trajectory of these fine particles is influenced by various factors. In a gas medium, the thermophoresis force typically drives small particles in the direction of decreasing temperature under temperature gradients [85], and thereby it's discovered that nanoparticles can be ejected from plasma core to plume periphery, when they approach the high thermal gradient zones [86]. Moreover, fine particle also tend to follow the plasma gas streamline and flow in parallel to the substrate surface, instead of impacting it. Stokes number, *St*, is found to be extremely helpful in predicting the particle trajectory in this situation [87]:

$$St \stackrel{\text{def}}{=} \frac{\rho_p d_p^2 v_p}{\mu_g l_{BL}} \qquad (15)$$

$$\begin{cases} St < 1, Particles\ stay\ in\ the\ gas\ flow \\ St > 1, particles\ reach\ the\ substrate \end{cases}$$

Where l_{BL} = thickness of the flow boundaries layer. VanEvery et al [88] have shown that the droplet trajectories close the substrate surface with $St < 1$ experience apparent shadowing effects, leading to the formation of coarse columnar microstructure in SPS TBCs.

1.2.5.7 Coating formation and splat/deposit morphology

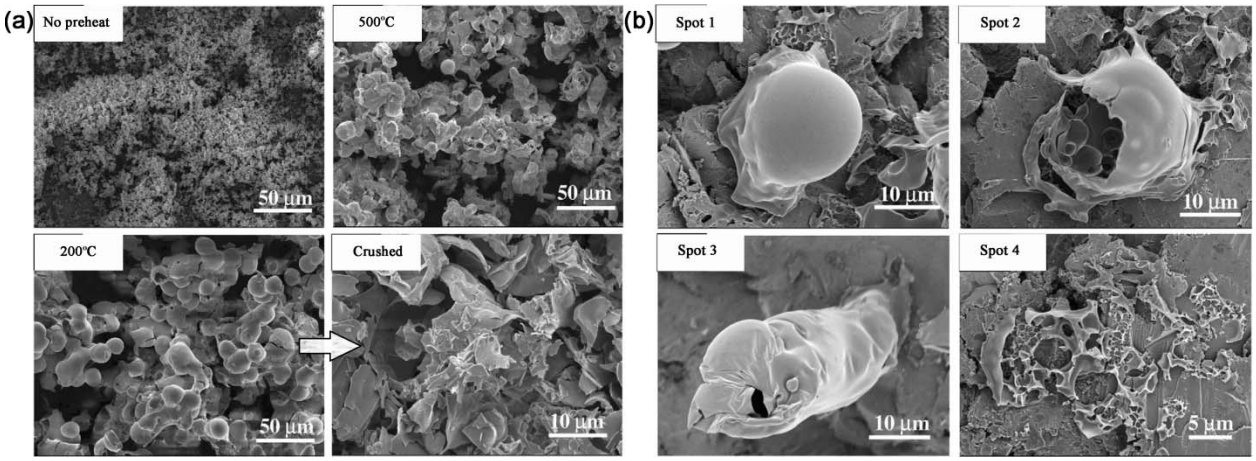

Fig. 1-9 Different deposit morphologies observed in the SPPS process due to (a) different substrate preheat temperatures and (b) different particle in-flight temperature-time history [92].

The dense thermally-sprayed coatings are generally considered to be formed by the layering and solidification of molten splats from the impaction of single or agglomerated particles. As the building blocks of the coating microstructure, deposited splats in fact exhibit a wide range of shapes and can affect the final coating microstructures directly. The morphology of as-deposited splats are known to be influenced by the droplet properties, such as dimensions, temperature, velocity, density and viscosity, as well as substrate conditions, which include surface roughness, chemical composition, wettability, temperature and contact resistance [89, 90, 91]. Being a variation of the thermal spray technology, the SPPS process shares the same characteristic; in fact as demonstrated in an earlier work by Xie et al. [92], variations in the deposit morphology

were distinctly affected by both the substrate preheat temperature and the particle temperature-time history in the plasma plume (**Fig. 1-9**).

One difference between the SPPS process and other plasma spraying processes in terms of splat morphology is that not only the ultrafine molten splats (<5μm) ([93], **Fig. 1-10c**) but also non-flattened micro-cracked "clusters" [94] are typically deposited on the substrate, which in together allow detailed microstructural features to form (e.g. micron and nanoscale interconnected porosity). Besides, the solute concentration in precursor solutions was shown by Chen et al. to cause varied splat morphology, thus leading to drastically different coating microstructures [95].

The initial layer of splat deposited on the substrates were shown by Li et al [96] to be amorphous and transparent, indicative of a rapid quenching, while the subsequent splats exhibited some degrees of crystallinity and discernable crack networks in overlapped areas. The splat solidification in the thermal spraying occurs simultaneously as the particles are deposited onto the substrates, and can be greatly affected by the cooling rates of deposited splats, leading to various coating microstructure and crystallization. If the heat conduction into the substrate is faster than the heat release from the crystallization, the solidification will then be determined by the continued nucleation, resulting in a fine equiaxed crystalline structure [97]. Ideally a uniform microstructure would be obtained if the temperature of incoming splats quickly decreases to the temperature of the underlying materials, but in reality, to manage a constant deposition temperature involves controlling multiple in-process variables, which include substrate heating, ceramic/substrate thermal properties, additional cooling and the thickness of underlying coating. Based on previous experience this is not an easy task.

1.2.5.8 Microstructures and properties of SPPS coatings

Because of the difference in deposition mechanisms, several unique microstructural features are present in the SPPS coatings. Through-thickness vertical cracks (**Fig. 1-10a**), being one of the most apparent features, can be easily acquired by the SPPS process, with less demanding coating and processing requirements in comparison to DVCs in some APS TBCs. The vertical cracks in SPPS process are formed by the pyrolysis and subsequent volume shrinkage of semi-decomposed coating materials during the deposition process [98], unlike the thermal shock for the DVC vertical cracks, but are capable of providing the similar strain tolerance. In addition, the ultrafine splat morphology and micron/nanoscale porosity in SPPS TBCs [99] are also capable of some enhanced mechanical/thermal properties.

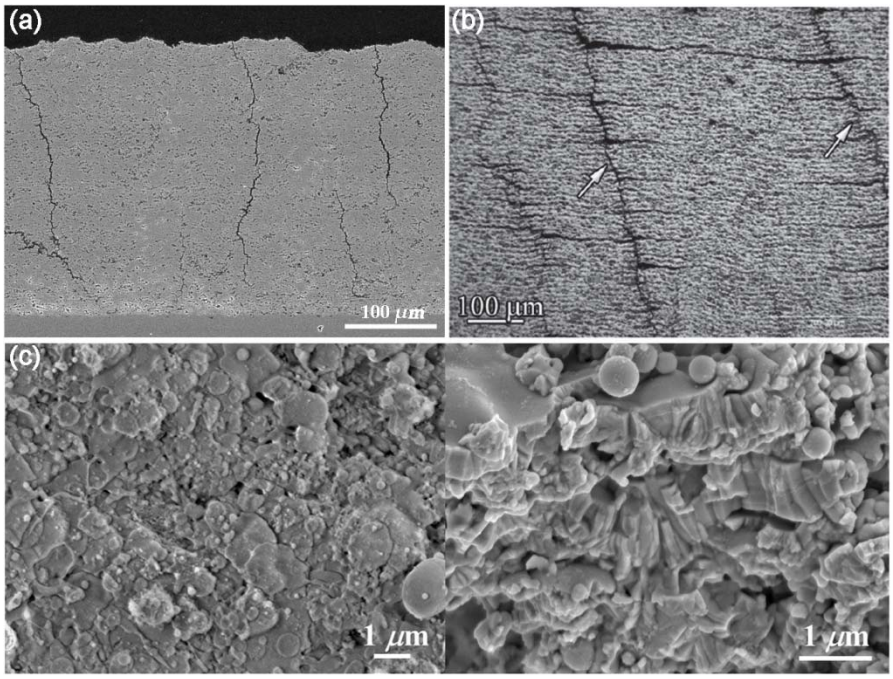

Fig. 1-10 (a) Through thickness vertical cracks [64], (b) the layered porosity, IPBs [100], and (c) the ultra-fine splat structures in the SPPS TBCs [93].

Crystallization in as-deposited coatings is critical to engineering materials, and it has been shown that both crystalline solid solutions (*t'*-YSZ [81]) and line compounds ($Y_3Al_5O_{12}$ [38]) can be

successfully deposited through the SPPS process, with limited concerns about in-process element volatilization. As stated earlier, thermal conductivity is also of great importance for ceramic coatings, especially in the application of TBCs. The thermal conductivity of regular SPPS TBCs has been found to be much lower than EB-PVD TBCs, but higher than conventional APS coatings [64] due to the finer microstructure and high splat-to-splat contact area [101]. The thermal conductivity in SPPS coatings can be significantly reduced by engineering the coating porosity into a layered fashion (**Fig. 1-10b**) [100] or co-doping with rare-earth oxides [102]. Furthermore, the bond strength and cyclic durability of SPPS TBCs have been shown to be notably superior to APS or even EB-PVD counterparts [103, 104, 58]. The stability of microstructures as well as crystalline phases have been confirmed by Xie et al [105], while Chen et al later demonstrated that SPPS YSZ TBC has a higher initiation temperature (1500^{o}C) for the accelerated grain growth and phase transformation to occur than other coatings sprayed by the conventional APS process (1400^{o}C) [106]. As for the mechanical properties, extensive studies by Jadhav et al showed that SPPS coatings generally exhibit higher toughness, less modulus and better hardness than APS coatings, though the anisotropic nature of the SPPS vertical cracking can give rise to a greater deviation between in-plane and out-of-plane properties [58, 107].

1.2.5.9 Application of the SPPS process

Having the advantage of quick chemistry alteration to the precursor solutions, the SPPS process has been adopted to fabricate coatings with a large variety of compositions, such as TiO_2 [108, 109], rare-earth zirconate [110], YAG and Y_2O_3 phosphors [111, 112], LSM perovskites [113] and doped YSZ [114]. From an economic standpoint, the cost of SPPS deposition, given the current practices and deposition efficiencies, is significantly less than the EB-PVD process but

slightly higher than the APS process [115]. The lower deposition rate in SPPS process, which is responsible for the higher cost than APS coatings, can be remedied by the use of larger, more powerful plasma guns, such as Mettech Axiall III, Metco Triplex, or Praxiar Plazjet [64]. Overall, the SPPS process makes a promising alternative technology for the advanced TBC development and potential industrial production.

1.3 Research objectives

In this project, the SPPS process (**Fig. 1-7**) is used first for depositing low thermal conductivity durable YSZ-based TBC topcoats. Due to the fact that liquid solutions, instead of oxide powders, are injected into the plasma plume, complicated physical/chemical transformations (e.g. solvent evaporation, solute precipitation, particle break-up, decomposition, melting) occur on the injected droplets during a short in-flight time. By tuning the process parameters, we will show that coatings' microstructure can respond readily, and among all microstructural changes, it's our primary goal to engineer the morphology of porosity in SPPS TBCs from a semi-uniform distribution to a layered manner, which is termed the Inter-Pass Boundaries (IPBs, **Fig. 1-10b**) [100]. IPBs, unique to the SPPS process, are effective in disturbing the heat conduction path and thereby reduce thermal conductivity. In an earlier study conducted in our group, a 28% reduction in thermal conductivity in YSZ TBCs was reported [102]. Full-scale optimization on process parameters is proposed to be systematically performed in this project, so as to produce more prominent IPBs in SPPS YSZ TBCs and further reduce thermal conductivity by ~50%. The repeatability issue is addressed and is shown not only by microstructural characterization but also from extensive thermal conductivity measurements. In addition, other critical coating properties, e.g. cyclic durability and erosion performance, are to be characterized as well.

To enhance the YSZ-based TBCs' resistance to CMAS attack, the two CMAS resistant materials, gadolinium zirconate and Al_2O_3/TiO_2-doped YSZ, are subsequently deposited by the SPPS process, benefited from the advantage of the quick precursor composition alteration with the SPPS process. In order to economize the use of expensive rare-earth and to overcome the thermodynamic incompatibility between GZO and Al_2O_3 TGO [116, 117], a double-layer structure consisting of GZO top-layer and YSZ inner layer has been known as a viable approach [30, 47, 49] and is produced with the SPPS process in this research. The reported high melting point (1550-1600^oC [37]) and good phase stability of GZO, additionally, would increase the maximum operating surface temperature, making the overall coating system more suitable for high temperatures applications. As for the Al_2O_3/TiO_2-doped SPPS YSZ TBCs, extensive spray trials are performed to incorporate IPBs into the ceramic coatings, in the hope of combining improved CMAS resistance and low thermal conductivity. One additional CMAS-resistant approach is attempted, namely filling the coatings' cracks and voids with infiltration-inhibiting substances, e.g. calcium sulfate [118] and/or yttria.

To evaluate the CMAS-TBC interaction in different TBC systems, glass buttons or pastes were seen in the literature to be placed on top of porous ceramic pellets that shared the same nominal TBC compositions, and tested in isothermal furnaces for extended durations [48, 119]. CMAS resistance was then determined from the glass infiltration depth, pellet morphology change and materials' reactivity. This method makes a quick tool for selecting CMAS-resistant materials, but it can't capture the realistic TBC performance subject to CMAS attacks in turbine engines, as it ignores the effect of TBC microstructures and fails to represent the drastic heating/cooling cyclic conditions. More advanced assessment designs, such as the jet engine thermal shock (JETS) tests [31, 120] and burner rig tests [121], are better at characterizing the CMAS-TBC interaction

under more realistic thermal gradient and cyclic conditions. However, these high-temperature high-gradient instruments aren't commercially available, and construction of one similar device is beyond the scope of this project. Therefore, the evaluation of CMAS resistance for several modified YSZ-based SPPS TBCs is proposed to be accomplished with a set of new CMAS-TBC interaction tests, called Spritz and Paste tests. In spritz tests, CMAS liquid precursors are periodically applied to TBC samples after each isothermal furnace cycle, as a good simulation of the slow CMAS accumulation between engine heating/cooling cycles. While the paste tests, which involve applying CMAS pastes to TBC surfaces before the aggressive thermal cycling test, are adopted in addition to the spritz tests to assess the CMAS-TBC interaction. As for the performance under typical IGCC high temperature humidity, modified SPPS TBCs are proposed to be evaluated in a customized high-temperature moisture rig, followed by a series of phase/microstructure stability study. In the end, based on all evaluation results, the TBC system that best suits IGCC environments with low thermal conductivity and enhanced corrosion resistance is selected and documented.

Chapter 2. Experimental Procedures

2.1 Preparation and characterization of precursor solutions

2.1.1 Precursor solutions for SPPS process

Precursor solutions for the SPPS process were prepared by mixing a range of organic or inorganic solutes in typical solvents of DI water or ethyl alcohol [58, 109, 111]. To deposit the low-thermal-conductivity YSZ interlayer, 75g yttrium nitrate hexahydrate were typically dissolved in 1L solution of zirconium acetate [122], yet occasionally alcohol-based solutions made from zirconium propionate were also used. The deposition of GZO PSLs was accomplished by dissolving 2.4 moles gadolinium nitrate hydrate in 1L zirconium acetate solution, with minimal efforts spent on other alternative combinations. For the deposition of Al_2O_3/TiO_2-doped YSZ TBCs, different combinations of organic and inorganic salts were used, depending on the solvent type (either water or ethyl alcohol). All precursor information is tabulated in **Table 2-1**

Table 2-1 Summary of all precursor solutions prepared for the SPPS deposition

Precursor type	Solvent	Solutes
YSZ	DI water	Zr[A] + Y[N]
	Ethyl alcohol	Zr[P] + Y[N]
GZO	DI water	Zr[A] + Gd[N]
Al_2O_3/TiO_2-doped YSZ	DI water	Zr[A] + Y[A] + Al[A] + Ti[S]
		Zr[A] + Y[A] + Al[S] + Ti[S]
	Ethyl alcohol	Zr[P] + Y[N] + Al[N] +Ti[I]
Note: A-acetate; N-nitrate; P-propionate; S-sulfate, I-isopropoxide.		

The thermal characteristics, viscosity, and surface tension of precursor solutions affect the microstructure in final coatings [67] and are thereby important to the SPPS process. These properties were measured, respectively, with DSC-TGA (10^oC/min with a 100mL/min N_2 flow,

SDT Q-600, TA Instruments), Ubbelohde viscometers (Cannon Instrument) in a digitally-controlled water bath, and a pendant drop tensiometer (OCA 20, Future Digital Scientific).

2.1.2 Precursor solutions for vacuum impregnation

To infiltrate CMAS-blocking materials into coatings' cracks and pores, precursor solutions of $CaSO_4$ and Y_2O_3 were prepared separately. For $CaSO_4$, calcium nitrate tetrahydrate and ammonium sulfate were mixed in water subsequently and was stabilized with ethylene-diamine-tetra-acetic acid (EDTA). The pH was monitored throughout the process and was adjusted to a final value of 6.3 using the ammonium hydroxide solution. The final nominal $CaSO_4$ content was calculated to be 8wt%. For Y_2O_3 precursor solutions, a saturated solution with yttrium nitrate hexahydrate was prepared in DI water.

2.1.3 Precursor solutions for CMAS-TBC interaction tests

The 1wt% aqueous CMAS precursors for the CMAS-TBC interaction tests were prepared by mixing various ingredients, such as calcium nitrate, aluminum nitrate, magnesium sulfate, sodium sulfate, potassium sulfate, ferric nitrate, titanium (III) sulfate, ammonium sulfate, aluminum sulfate and colloidal silica, in deionized water, based on the CMAS compositions listed in **Table 2-3**. In order to obtain stable precursors, chelating agents, e.g. EDTA, were also added, and pH was monitored and adjusted accordingly throughout the process. The melting points for different CMAS precursors were later measured using TA SDT-600.

2.2 Substrates

The dimensions of all substrates used in this project were mostly 25.4mm in diameter and 3mm in thickness, with only a few exceptions. 304/304L stainless steel and graphite (Ted Pella Inc.,

Redding CA) discs were typically utilized for SPPS process optimization and thermal conductivity measurements, while bond-coated, single-crystal alloy substrates and APS YSZ baseline specimens, which were provided by industrial partners, were reserved for critical furnace tests, due to the limited availability. Additionally, in-house deposited APS NiCoCrAlY bondcoats were also used in the case of high-temperature steam tests, given the sole interest of these tests concerned only the ceramic topcoats. All substrate information is summarized in **Table 2-2**. All characterizations on the substrates are similar to those applied to ceramic coatings; however, the surface roughness tests were performed with either Zygo 3-D Optical Scanning Interferometer Profilometer or Phase II SRG-4500 Surface Roughness Profilometer specifically, showing the surface roughness of both OEM and in-house deposited MCoCrAlY bondcoats to be 4.57±0.29 μm and 6.26±1.05 μm, respectively.

Table 2-2 Substrates used for different tests in this project

Substrate	Test	Topcoat
Grit-blasted 304/304L stainless steel discs	Process optimization, Thermal conductivity measurement	APS YSZ (Sulzer® 2O4NS)
		SPPS YSZ with IPBs
		SPPS GZO
		Double-layer SPPS GZO/YSZ
		Al_2O_3-doped SPPS YSZ
		Al_2O_3/TiO_2-doped SPPS YSZ
Graphite planchets	Thermal conductivity measurements	APS YSZ (Sulzer® 2O4NS)
		SPPS YSZ with IPBs
		SPPS GZO
304/304L stainless steel discs with APS NiCoCrAlY bond-coats (Sulzer® AMDRY® 365-2)	Bond strength tests (ASTM C633)	SPPS YSZ with IPBs
Single crystal superalloy buttons with LPPS or HVOF MCrAlY bond-coats (OEM)	Cyclic durability tests, CMAS-TBC interaction tests, Erosion resistance tests (ASTM Standard G76-07)	APS YSZ (OEM) as baseline
		SPPS YSZ with IPBs
		Double-layer SPPS GZO/YSZ
		Al_2O_3/TiO_2-doped SPPS YSZ
		Infiltrated SPPS IPB YSZ
Single crystal PWA 1484 buttons with APS NiCoCrAlY bond-coats (Sulzer® AMDRY® 365-2)	High temperature moisture tests	Double-layer SPPS GZO/YSZ
		Al_2O_3/TiO_2-doped SPPS YSZ

2.3 TBC deposition using the SPPS process

A Metco 9MB spray system with a 3MB gas-handling panel was employed for the process. The primary gas was argon and the secondary gas was hydrogen, and the compressed air was used for atomization in cases where the air atomization was needed. The gas flow rates, the current and voltage of the plasma arc were adjusted to change the plasma torch power. A customized fluid delivery system was employed, which consists of two precursor storage tanks under a regulated air overpressure that drove fluid to the plasma jet through a delivery hose (**Fig. 1-7**). Solution precursors were injected into the plasma plume through either an atomizing nozzle or a stream nozzle. To specify the nozzle positions, radial/axial distances of the nozzle were recorded before each trial. In addition to gun power, other important processing parameters (e.g. solution precursor feed rates, standoff distances, raster scan step sizes, plasma torch movement speed and cooling procedures) were systematical altered during the search for the optimal spray conditions. Additional in-process quality control devices, namely the Control Vision camera system (SprayCam, Control Vision Inc., Sahuarita AZ) and the infrared pyrometers (Industrial Non-Contact Infrared Thermometer/Transmitter, Omega Engineering Inc., Stamford CT), were used occasionally during the process development for new precursor solutions.

2.4 Laser-flash measurement and thickness verification

As-sprayed SPPS TBCs were routinely measured with laser-flash (Netzsch LFA447) to determine the thermal conductivity. Single- or double-layer models were alternatively utilized depending on what sample geometries were. Based on a quantitative sensitivity analysis of the calculated topcoat thermal conductivity to input parameters reported by Taylor, coating thickness, density and specific heat contribute the most errors to thermal conductivity measurement [123].

This phenomenon was confirmed by a similar study done as part of the research. Since the uncertainty of coating thickness causes the most error [123], the topcoat thickness was then determined by scanning electron microscopy (SEM) characterization on cross-sectional images. This method was found to give more accurate thickness measurement than the traditional use of a micrometer, as the effect of surface roughness or any surface imperfection was minimized. Specific heat data of both SPPS top layers and the substrates were gathered from the Modulated-DSC TA-Q100, and calibration was conducted prior to each measurement using standard sapphire references. Weights and dimensions of specimens were documented before/after each spray trial, from which densities were calculated. For laser-flash measurements, specimens were typically spray-coated with a thin layer of graphite so that heat was transferred predominately by conduction through the sample by not allowing the laser to penetrate the semi-translucent sample.

2.5 Microstructural characterization

Sectioned TBC samples were embedded in a low-viscosity epoxy resin (Allied High Tech) and were manually/automatically polished for metallography. Field emission scanning electron microscopes (JSM-6350/5F) and the energy dispersive X-ray spectrometer (EDS, Noran system six) were employed for cross-sectional microstructure characterizations. Sputtered Au/Pd coatings were routinely applied by a Polaron E5100 SEM Coating Unit to compensate for the poor electrical conductivity of the epoxy resin.

2.6 X-ray diffraction

The phase evolution in SPPS TBCs was captured by scanning the deposited coatings in a powder diffractometer (D2 Phaser, Bruker AXS).

2.7 Erosion test

The erosion behavior of SPPS YSZ top layers with IPBs was evaluated with an in-house built erosion rig at Penn State University, following the ASTM G76-07 standard. In the customized rig, erosion media were injected into a stainless steel chamber through a vibratory feeder at a constant rate before being mixed with the pressurized air. Then the mix had to go through a 37.5cm acceleration tube and hit the masked erosion specimen in a vacuum chamber. Mass loss was determined by weighing specimens before and after every test period, with a scale sensitive to the fifth significant digit. Test accuracy was assured with the adoption of multiple measurements [124, 125]. Besides, SPPS TBCs deposited on the superalloy substrates were also tested along with baseline samples, e.g. OEM APS YSZ, so that unbiased conclusions can be drawn upon direct comparison.

2.8 Bond strength test

Standard tensile bond strength test [126] was performed on SPPS TBCs at Metcut Research Inc. The SPPS samples were fabricated with bond-coated 304 stainless steel substrates, and were later glued to pull bar fixtures using a high peel strength FM1000 epoxy for the tensile pulling tests.

2.9 Cyclic thermal durability test

SPPS TBCs on super-alloy substrates were characterized in an isothermal cyclic furnace (CM Furnaces Inc.) to evaluate the cyclic durability performance, as described in [127, 128]. In the test, the furnace controlling thermocouple was welded to the back of a dummy sample to assure the thermal history of the specimen and not the furnace itself was controlled. This was because comparison of the sample-mounted thermocouple with the furnace resident thermocouple

previously showed that significant errors in assessing the specimen temperatures could result from using the furnace thermocouple to determine sample temperature, especially during the heating transient. The temperature profile of each thermal cycle was set up to be 5-min heating up to 1121^{o}C, 45(50)-min isothermal soaking and 10(5)-min forced air cooling to room temperature by a blowing fan. Sample failure was defined as more than 50% area spallation, and SEM was then employed to determine spallation sites and TGO thickness. In order to obtain statistically confident results, multiple samples (at least two) of the same TBC system are routinely tested simultaneously.

2.10 CMAS-TBC interaction: spritz and paste tests

As mentioned in the introduction, the jet engine thermal shock test and burner rig tests are better designs for characterizing CMAS-TBC interactions. However, due to the limited resources and time, a series of simple but still effective tests were developed in the isothermal cyclic furnace to assess the CMAS-TBC interactions and the relative improvement of CMAS resistance for each modified YSZ-based TBC system. Different simulated CMAS compositions (4-, 7- and 9-CMAS as listed in **Table 2-3**) were used in this case, each named after the number of nominal constituents in the corresponding final thermally-decomposed mixes. The melting points of the compositions 7-CMAS and 9-CMAS were measured by DSC-TGA.

Table 2-3 CMAS compositions and melting points

Constituents	Si	Ca	Al	Mg	Na	K	Fe	Ti	S	Melting points
4-CMAS (at%)	49.47	37.65	7.88	5.00						~1200^{o}C [48]
7-CMAS (at%)	46.34	35.22	7.42	5.47	1.85	1.85	1.85			1132^{o}C (**Fig. 7-1**)
9-CMAS*	1.00	0.64	0.61	0.13	0.08	0.06	0.04	0.03	0.59	1180^{o}C (**Fig. 7-1**)

*This proprietary composition is normalized at OEM's request.

To simulate the periodic uptake of traceable amounts of CMAS during engine operation, samples were isothermally cycled to 1180^{o}C using one hour cycles. During the cooling stage, when the samples were at approximately 400^{o}C, CMAS precursor solutions were sprayed over the TBC surfaces with medical bottle atomizers (0.1 mL/spray, LMA MADomizer^{TM}, San Diego CA), one spritz per cycle. One SPPS YSZ sample was also sprayed with deionized water to determine if thermal shock was a significant source of damage in this experiment. The temperature for applying liquid CMAS precursor involves compromise between applying it at a realistically high temperature and not creating excessive thermal shock from applying water-based liquids. The temperature of 400^{o}C was chosen as an arbitrary compromise, yet the study of this temperature effect was beyond the scope of this project.

For more severe testing conditions, samples were also spread with a CMAS paste (25wt% 7-CMAS paste, other ingredients including deionized water and a low-viscosity Allied High-Tech epoxy resin) prior to the cyclic durability test. The final dose of the 7-CMAS paste was determined to be 10mg/cm^2 (equivalent to 25 spritzes of CMAS precursor solutions), based on the reported minimum CMAS level to initiate TBC damage by Wellman et al [129]. Cycles to failure and spallation mechanisms were examined for each TBC system.

2.11 High temperature moisture test

The high-temperature moisture corrosion resistance of modified SPPS TBCs was evaluated by controlling the humidity within a tube furnace (**Fig. 2-1**); testing conditions were chosen from relevant works [130]. The test temperature was set to 1121^{o}C, and the moist air (air + 30%H_2O) was disconnected from the quartz tube until the set temperature was reached, so that exact

reaction time was maintained. The hot-zone temperature was confirmed with a *K*-type thermocouple inserted next to the test piece, in addition to the *B*-type one resident in the furnace. Granted the testing environment in this setup was reaching the upper application limit for *K*-type thermocouple, the temperature agreement between the *K*-type and *B*-type thermocouples was mostly acceptable ($<\pm 5^{o}C$), suggesting the deterioration of the thermocouple was not a major concern. Test samples were typically heat-treated for 300/400 hours, and X-ray diffraction patterns were collected every 50 hours. The same experiment setup was also utilized for a dry tube furnace test (with no feeding of moist air), serving as comparisons to the high temperature moisture tests.

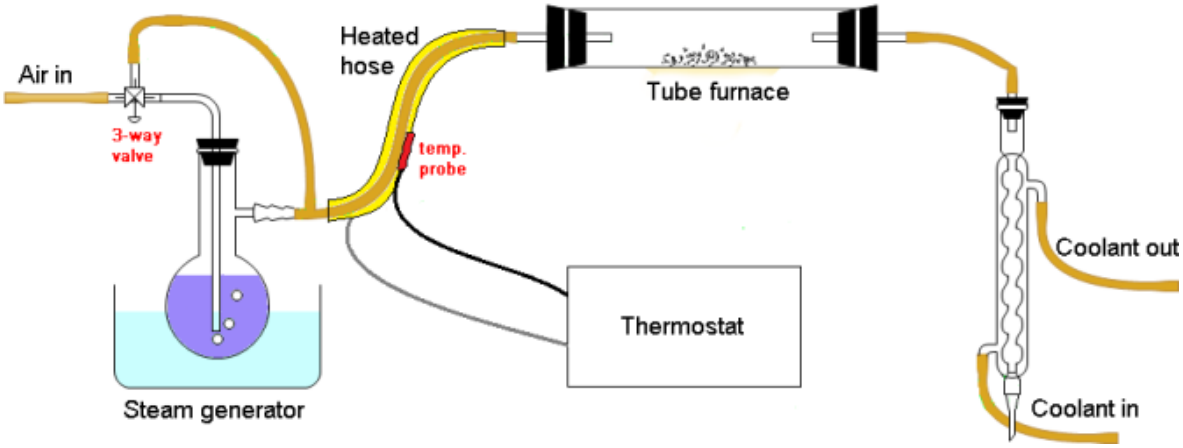

Fig. 2-1 High temperature moisture rig

Chapter 3. Low Thermal Conductivity YSZ TBCs Fabricated Using the SPPS Process

3.1 Precursor solution characterization and selection

The chemistry and fluid properties of precursor solution are known to affect the microstructure of SPPS TBCs [67]. In order to attain high deposition rates, precursors with high molarity are preferred; however, increased solute loading will generally raise the precursor viscosity and therefore impede fluid delivery, so only a limited range of viscosity is acceptable for practical purposes. In the case of our current delivery system, the upper bound of precursor viscosity is estimated to be 20cP.

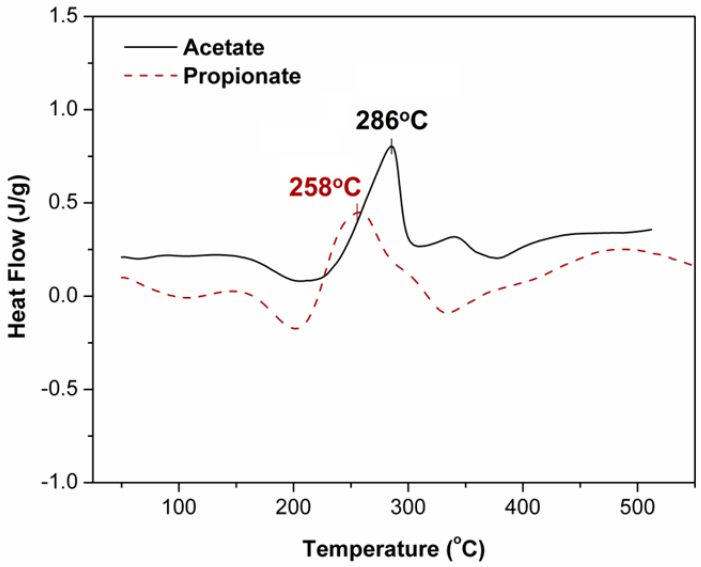

Fig. 3-1 DSC-TGA heat flow profiles of both acetate- and propionate-based 7YSZ precursor solutions, obtained at a heating rate of 10°C/min under a 100mL/min Ar flow

Thermal characteristics of solution precursors can impact coating microstructural morphologies remarkably [67]. A predominant exothermic performance during in-plume pyrolysis is one of the critical qualities of a successful precursor. Generally speaking, it's rather challenging to

sufficiently heat the droplets to fully evaporate the solvent, pyrolyze the salts and melt the oxides in such a short in-flight time, and hence endothermic events, which extract energy from the pyrolysis process, are not desirable. DSC-TGA characterizations on 7YSZ solution precursors made from both zirconium acetate and propionate (**Fig. 3-1**) indicate that precursors undergo a sequence of endothermic and exothermic reactions during in-flight pyrolysis, but exothermic reactions are predominant in the early stages of decomposition ($\leq 300^{o}C$) for both kinds of solutions. Early-stage endothermic events are detrimental to the SPPS process as they delay the particle heating and push the melting event to the cooler plume downstream. Given that the typical specific heat values of most ceramics are in the neighborhood of 0.5 J/g, the net heat gain for each precursor (**Table 3-1**) could theoretically lead to very substantial temperature increases, and aid full particle melting. The acetate and propionate precursors were therefore preferred in this work. Precursor solution viscosity [95] and surface tension can also impact the SPPS process in terms of precursor entrainment and droplet sizes [131]. As a rule of thumb, low viscosity and low surface tension are preferable for liquid delivery and droplet break-up, but their significance varies depending on the solvent itself. Ultimately there is a balance between a high cation loading and a low viscosity; this consideration, in part, leads to the specific formulations used in this study.

Table 3-1 Thermal characteristics, viscosity and surface tension of both acetate- and propionate-based 7YSZ precursor solutions

Precursor	Dynamic viscosity (cP)	Surface tension (mN/m)	Endothermic heat* (J/g)	Exothermic heat* (J/g)	Net heat* (J/g)
Propionate YSZ (alcoholic)	11.14	22.6	-36.1	485.1	449
Acetate YSZ (aqueous)	6.16	52.65	-33.4	419.1	385.7
*Heat = heat from decomposition reactions					

3.2 Target microstructure development

Porosity in TBCs can interrupt the direct flow of heat, forcing longer conduction paths and heat flow through decreased projected area region, and thereby reduce the overall thermal conductivity. By arranging the pores in layers, it becomes more difficult for the heat flow to find a path that avoids porosity, without taking a longer path through narrow regions with high thermal resistance. This effect is illustrated by the finite element experiments displayed in **Table 3-2**, where the thermal conductivity of a series of simulated coating microstructures with the same total porosity (~10vol%) are arranged increasingly into planar arrays or layers. The simulation was done using the OOF program, a Linux-based finite element analysis software developed by NIST [132], to compute coating thermal conductivity based on the input porosity geometry. The analysis was run assuming a steady state thermal conduction and thermal conductivities of 2.3 $W \cdot m^{-1}K^{-1}$ for dense YSZ and 0.024 $W \cdot m^{-1}K^{-1}$ for air trapped in pores. It can be seen that as the path of least resistance for conduction becomes limited, thermal conductivity declines accordingly.

Table 3-2 Simulated YBC thermal conductivity evolves as a function of porosity geometry. (10vol% porosity in black)

Artificial microstructure	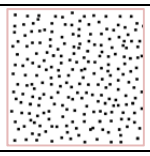	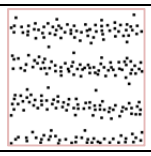	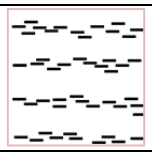		
Thermal conductivity ($W \cdot m^{-1}K^{-1}$)	1.942	1.876	1.256	0.800	0.176

3.3 SPPS process optimization for minimum thermal conductivity

Based on previous studies on SPPS YSZ TBCs [58, 95, 102, 100], key processing variables affecting as-sprayed microstructures were selected and summarized in **Table 3-3**.

Table 3-3 Key SPPS processing parameters explored for IPB optimization

Parameter	Range
Precursor solutions	Aqueous yttrium nitrate/zirconium acetate or alcoholic yttrium nitrate/zirconium propionate
Injection type	Atomizing nozzle or stream nozzle
Liquid precursor feed rate	20-60 mL/min
Plasma gun power	40-45.5 kW
Transverse speed	400-800 mm/s
Raster scan step size	1-6 mm
Cooling	No cooling or 30-60s pauses per 5 cycles
Standoff distance	31.75-57.15 mm (1.25-2.25 in.)

A two-stage study that extensively studied the influences of each process variables and utilized more than 100 spray trials was conducted to optimize the IPB microstructural feature and further reduce the thermal conductivity of SPPS YSZ TBCs. In the first exploratory stage, SPPS processing variables were systematically changed, forming a processing-structure matrix. A series of SPPS YSZ TBC microstructures were produced with promising layered porosity, and visual examination of polished cross-sections were subsequently used to guide the optimization study based on the observed strength of layering. In the second stage, when a number of promising microstructures were obtained, thermal conductivity of the TBCs was then measured directly using the laser flash method, constituting the structure-property relationships.

3.3.1 Precursor type

Table 3-1 shows that the YSZ precursor made from zirconium propionate has more net heat gain than zirconium acetate. Because of the chemical reaction between zirconium propionate and water, the propionate precursor solution was prepared in ethanol, which has less enthalpy of

evaporation than water (841kJ/kg vs. 2260kJ/kg). As a consequence, coatings sprayed with zirconium propionate precursor were generally denser than the ones sprayed with the acetate.

3.3.2 Injection method

The effect of the injection method was studied by comparing the coatings' microstructural differences after using an air blast atomizing nozzle (BETE Fog Nozzle) and a stream injection nozzle. With an atomizing nozzle, precursor solution is delivered as uniform fogs consisting of droplets, while in the case of stream injection precursor is delivered to the plasma as a continuous liquid stream and is subsequently atomized by impact from the transvers high velocity plasma jet. Depending on the atomizing air pressure, the atomizing nozzle is shown to dispense droplets with a range of 1-100μm with an average size of 40μm as [73]. During the optimization process, an atomizing pressure was chosen specifically to have a certain fraction of droplets acquire sufficient sizes and momenta for plasma plume entrainment, while other droplets in the plasma periphery would experience partial pyrolysis, and thereby form vertical cracks [64, 98] and IPBs. This was adjusted by the nature of the deposited coating from multiple spray passes. When the liquid precursor was injected as a continuous stream through the use of a needle-like nozzle, droplet entrainment into the hot inner core of the jet was generally uniform and had a small projected area on the jet surface. As a result, the as-sprayed coating was typically denser with weaker IPB traits, due to the lack of semi-pyrolzed deposits coming from the precursor that travelled in the jet periphery as compared to the use of atomizing nozzles.

3.3.3 Precursor feed rate

SPPS process economics favor a high molarity solution and a high solution feed rate, as they would theoretically increase the deposition and production rates. However, the precursor feed

rates, similar to the solute loading in the precursor solution, cannot increase without a limit, because beyond a certain point the volume of solution will start to quench the plasma jet significantly and cause excessive amounts of unpyrolyzed materials to deposit on the substrate, forming a porous coating. In short, an increased flow rate of liquid feedstock increases the amount of porosity in the as-sprayed coatings, and thereby helps the definition of IPBs (**Fig. 3-2**) until the microstructure begins to deteriorate and the amount of porosity exceeds the tolerance for TBC applications.

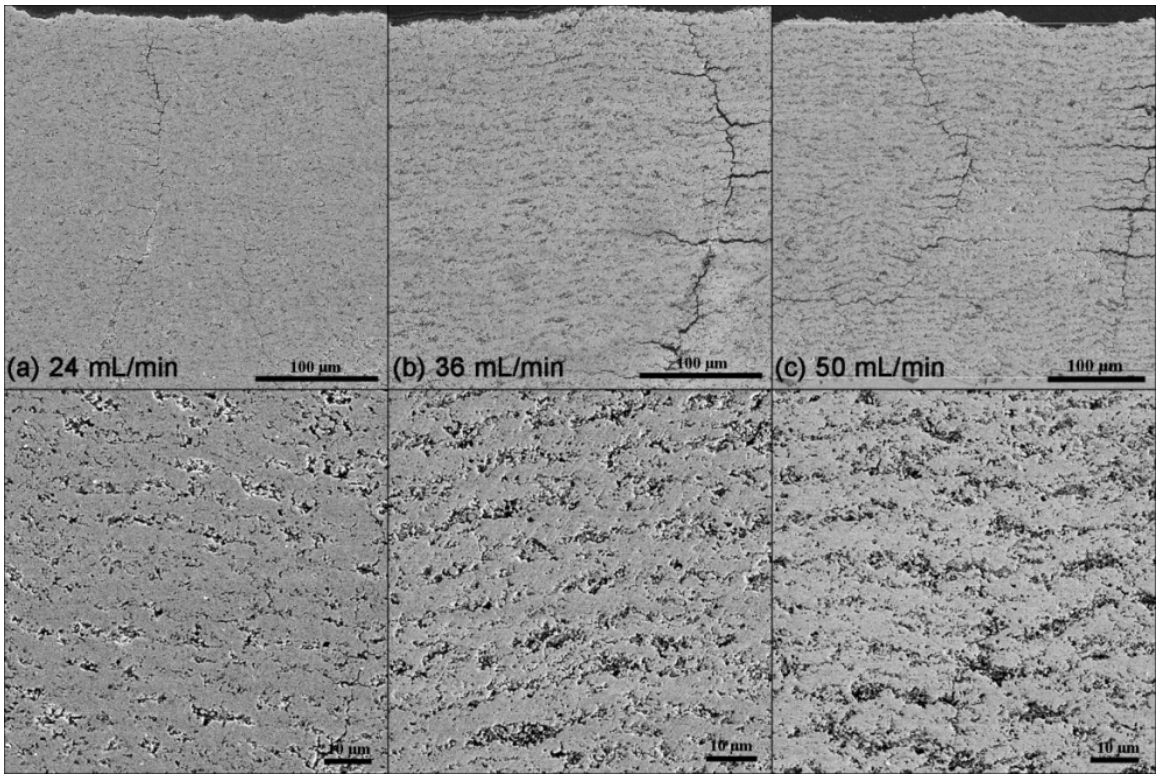

Fig. 3-2 Cross-sectional micrographs of topcoats sprayed with the same 2mm raster scan step size, 41.3mm standoff distance and 45kW plasma power except for different liquid precursor feed rates: (a) 24mL/min, (b) 36mL/min, and (c) 50mL/min

3.3.4 Standoff distance

The substrate standoff distance has its impacts on coating morphology. When the substrate is too close to the plasma torch exit nozzle, excessive heat from the plasma torch will damage the

substrate surface as well as the newly-deposited surfaces, causing the coating to spall off. While if the substrate is too far from the torch exit nozzle, melted precursor particles will then re-solidify in the flight as the plume temperature drops considerably, resulting in reduced deposition efficiency and a porous coating. For the Metco 9MB gun, IPB microstructures are observed in stand-off distances of 38.1mm to 50.8mm (1.5 in. to 2 in.); however, the strength of the IPB features tends to increase as the standoff distance is shorter (**Fig. 3-3**).

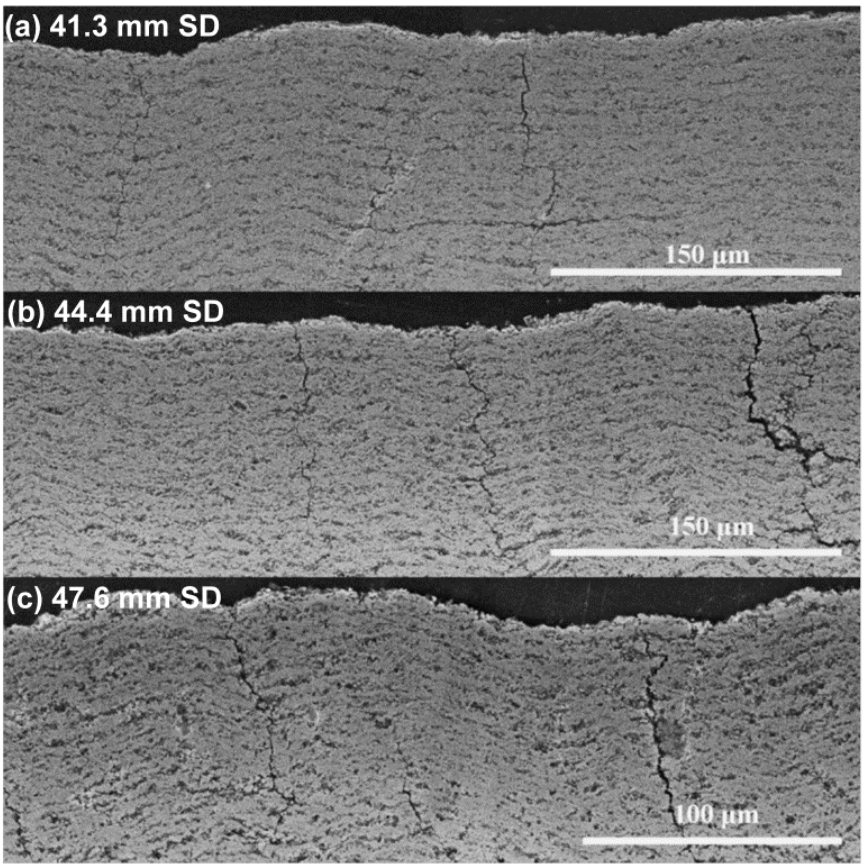

Fig. 3-3 Cross-sectional micrograph of topcoats sprayed with the same feed rate of 36mL/min, 2mm raster scan step size and 4 kW plasma power except for different standoff distances: (a) 41.3mm, (b) 44.4mm, and (c) 47.6mm

3.3.5 Plasma gun power

Without enough plasma gun energy to fully melt injected materials, porous coatings are reasonably expected. In fact, in one spray trial only a small energy difference had a significant

effect on the microstructural integrity, as a reduction of 5kW in gun power causes distinct hollow regions in **Fig. 3-4b**.

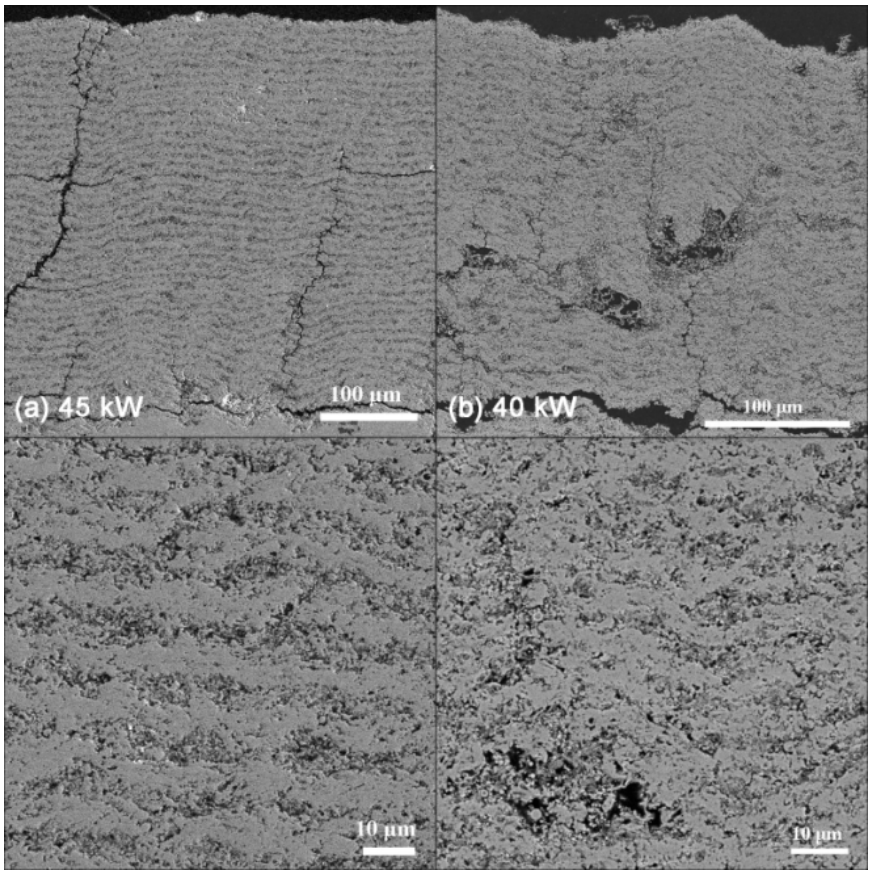

Fig. 3-4 Cross-sectional micrographs of topcoats sprayed with the same 2mm raster scan step size, 44.4mm standoff distance and feed rate of 50mL/min except for different plasma gun powers: (a) 45kW and (b) 40kW

3.3.6 Raster scan step size

Another key parameter in the SPPS process is the raster scan step size. As mentioned earlier, when the high molarity liquid precursor is injected into an atomizing nozzle, the precursor quickly fragments into smaller droplets due to *initial* and *secondary* break-ups, and forms a fog. Depending on the initial momentum of each droplet, the entrainment performance differs and, consequently, the droplet will end up at different sections of the plasma plume: (i) the cool temperature periphery region, (ii) the moderate temperature outer core, or (iii) the hot inner core

(**Fig. 3-5a**) [64]. In the hot inner core, the solvent evaporates and the precursor chemicals decompose, pyrolyze and melt subsequently forming dense deposits. While in the cooler periphery region, the insufficient energy causes the particle to form a partially-pyrolyzed splat on the substrate, which continues to decompose in-situ from the subsequent heating and produces a porous microstructure. These trends are particularly evident when the coating is sprayed repeatedly on a single line with no raster scan step [133]. As the plasma torch scans over the substrate in a raster scan pattern (**Fig. 3-5b**), a microstructure of alternate dense/porous layers is produced and the raster scan step size determines the strength of the IPBs.

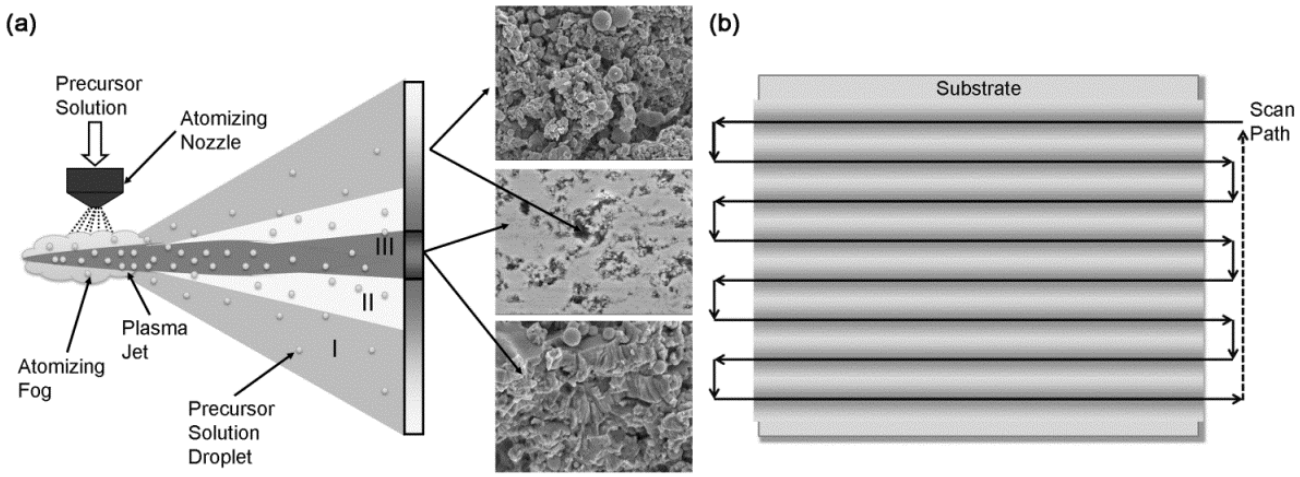

Fig. 3-5 Schematic of SPPS process with (a) an atomizing nozzle, and (b) raster scan pattern

This IPB feature, consisting of alternate dense and porous layers, is inherent to the SPPS process. However, since the normal scan step height is so large in regular SPPS practices, this feature is obscured. As the raster-scan step size decreases, more scans are performed over a given area of the substrate surface, so the heat accumulation and dense/porous contrast is enhanced, leading to a more prominent IPB feature (**Fig. 3-6**).Ultra-small step sizes however, could result in an excessive in-situ heat built-up, and raise the chances of substrate overheating and coating

spallation. Fast gun scan speeds as well as additional cooling are helpful for mitigating such problems.

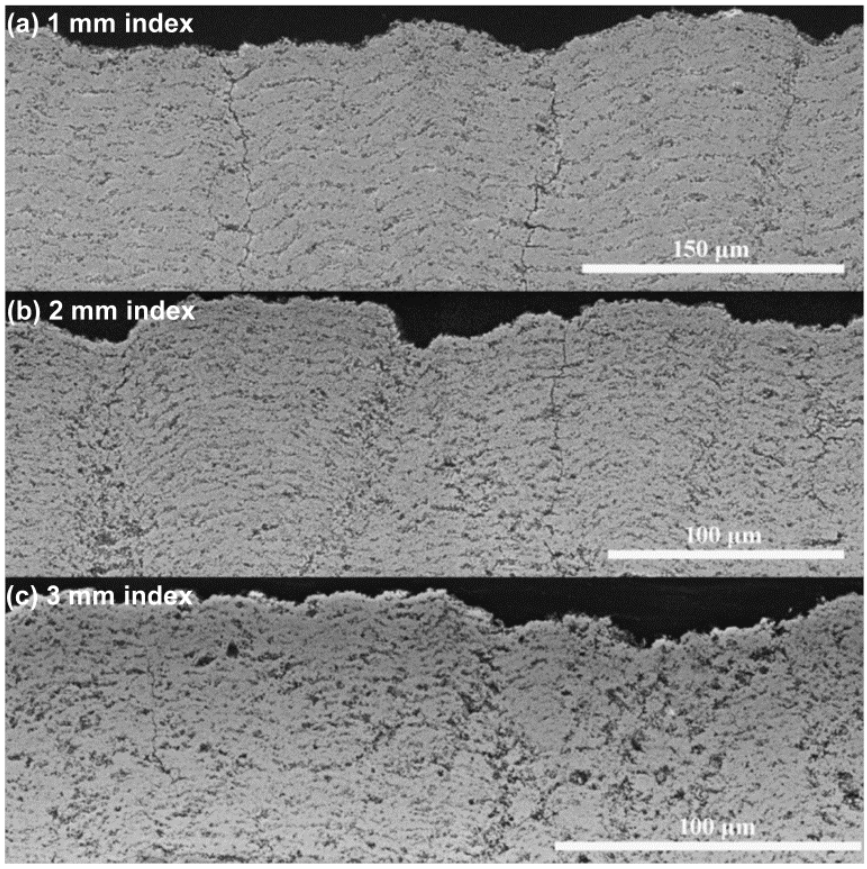

Fig. 3-6 Cross-sectional micrographs of topcoats sprayed with the same 44.4mm standoff distance, feed rate of 36mL/min, 45kW plasma power except for different raster scan step sizes: (a) 1mm, (b) 2mm, and (c) 3mm

3.3.7 Substrate surface roughness

The effect of substrate surface roughness is not reflected in the scope of regular spray practices; however, it became an issue when OEM alloy substrates with exceptionally rough surfaces were used for process development, and drastically different microstructures were observed (**Fig. 3-7**). Since the particle size of the SPPS process is small due to drastic droplet break-up and pyrolysis in the plasma jet, the deposited splats are also remarkably smaller than those in the APS process. When the substrate surface is too rough, it is nearly impossible for such small splats to

completely cover the complex surface geometry forming strong mechanical bonding. Besides, as suggested by VanEvery et al [88], the fine SPPS particles with small Stokes numbers will suffer a more severe shadowing effect on such rough substrate surfaces, resulting in microstructural anomalies and further deteriorated mechanical properties. A good rule of thumb for satisfactory coating adhesion is that the surface roughness should be comparable to the size of the deposited splats. Smoothing the substrate surface to a roughness range of ~5 μm is generally recommended so that good process reproducibility is guaranteed, especially when new combinations of substrate and bond-coat are used but the surface roughness is not specified.

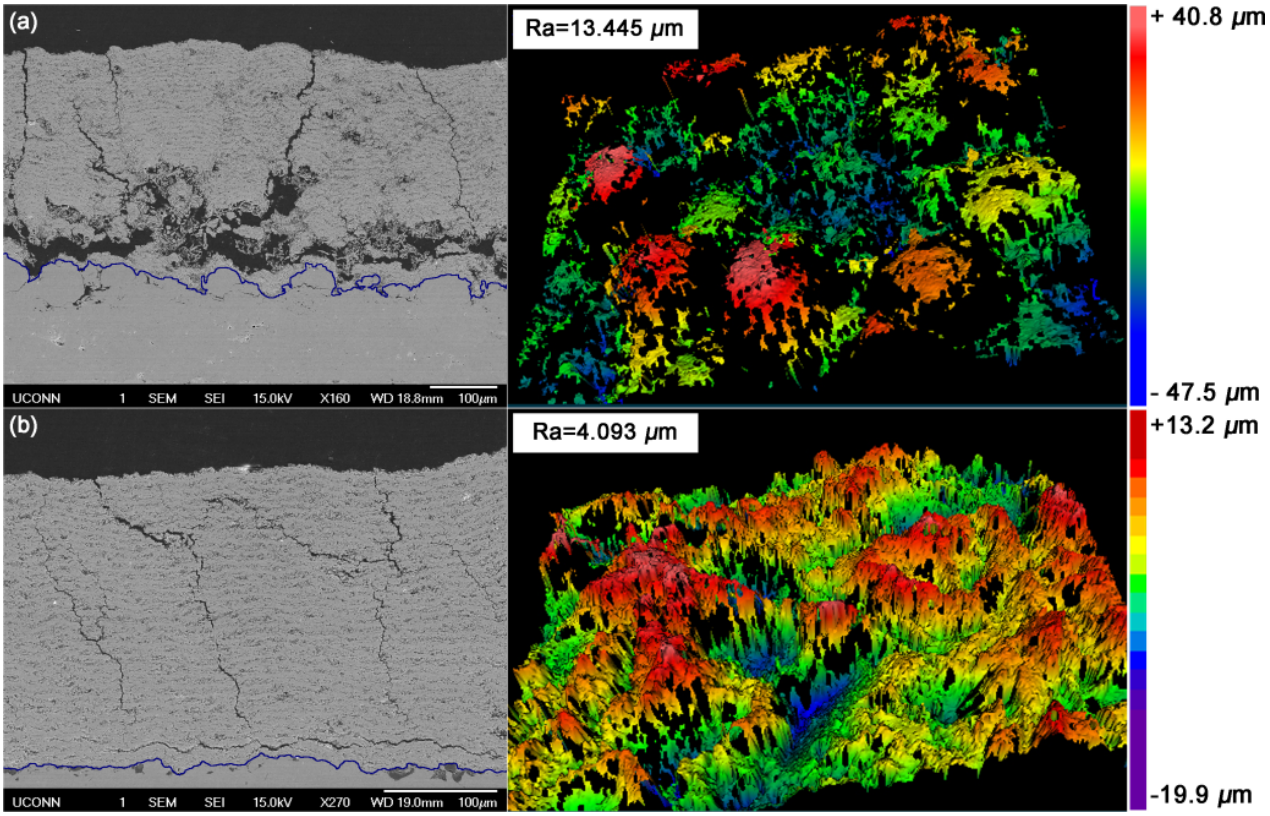

Fig. 3-7 Effect of substrate surface roughness on topcoat microstructure: (a) Ra=13.445μm, and (b) Ra=4.093μm

3.4 Thermal conductivity determination using the laser-flash method

In terms of associating IPB prominence with the overall thermal conductivity of the ceramic topcoat, initial efforts were made to continue using OOF to compute thermal conductivity from cross-section micrographs, as was did in [100]. Bacos et al. [134] later showed that the insufficient ability to reflect complicated 3D microstructural features in 2D images has caused OOF to be incapable of providing reliable measurements. Besides, submicron pores and cracks that are easily obscured in the low-resolution 2D images can in fact still aid the disruption of the heat conduction in coatings, and thereby generate discrepancies between OOF-estimated and experimentally measured thermal conductivity values, as shown in **Table 3-4**. Laser flash measurements, on the other hand, measure thermal conductivity directly from actual microstructures thus providing more reliable characterization.

Table 3-4 Thermal conductivity of YSZ TBCs with IPBs determined by LFA and finite element analysis (FEA) using OOF software

Sample#	OOF	LFA		
	Thermal conductivity @150°C ($W \cdot m^{-1}K^{-1}$)	Thermal conductivity @150°C ($W \cdot m^{-1}K^{-1}$)	Model	Substrate dimensions *a*×b×*h* or D×*h* (mm)
304/304L SS		16.5	Single-layer	6×6×3, square piece
#042412C	0.919	0.72	Two-layer	6×6×3, square piece
#042412D	1.13	0.99	Two-layer	6×6×3, square piece
#060412G	1.216	0.55	Two-layer	25.4D×2, disc
#060412I	1.235	0.32	Two-layer	25.4D×3, disc

The flash method is a well-established technique for measuring thermal diffusivity of solid materials [135]. The front surface of a planar specimen is typically heated by a uniform pulse of light, and the transient heat is transferred to the rear surface through conduction. Simultaneously, the change in rear surface temperature is detected, usually by an infrared radiometer. In theory,

the temperature distribution, $T(x)$, in a thermally insulated planar solid with a uniform thickness of l at any given time, t, is governed by the following equation [136],

$$T(x,t) = \frac{1}{l}\int_0^l T(x,0)dx + \frac{2}{l}\sum_{n=1}^{\infty}\left(\frac{-n^2\pi^2\alpha t}{l^2}\right) \times \cos\left(\frac{n\pi x}{l}\right)\int_0^l T(x,0)\cos\left(\frac{n\pi x}{l}\right)dx \qquad (16)$$

Incorporate the boundary conditions:

$$\begin{cases} T(x,0) = \dfrac{Q}{\rho C_p g}, 0 < x < g \\ T(x,0) = 0, g < x < l \end{cases}$$

where Q = radiant energy, ρ = solid density, C_p = specific heat, α = thermal diffusivity, and g = small depth into the front surface of the planar solid, the temperature distribution in the planar solid can then be rewritten as

$$V = 1 + 2\sum_{n=1}^{\infty}(-1)^n \exp(-n^2\omega) \qquad (17)$$

assuming

$$V(l,t) \stackrel{\text{def}}{=} \frac{T(l,t)}{T_M} = \frac{\rho C_p T(l,t) l}{Q} \quad (18) \quad \text{and} \quad \omega \stackrel{\text{def}}{=} \frac{\pi^2 \alpha t}{l^2} \quad (19)$$

where T_M = the maximum temperature at the rear surface.

Knowing V = 0.5 when ω = 1.38 according to the $V - \omega$ plot, the thermal diffusivity of the planar specimen is then calculated as

$$\alpha = 1.38 \times \left(\frac{l^2}{\pi^2 t_{0.5}}\right) \qquad (20)$$

and thermal conductivity, K, as

$$K = \alpha \rho C_p \qquad (21)$$

Table 3-5 Typical physical properties of the SPPS YSZ coating and the steel substrate

Material	Thickness (mm)	Density (g/cm^3)	Thermal diffusivity (mm^2/s)
Ceramic layer (SPPS YSZ)	0.20-0.60	3.8-4.9	0.21-0.35
Substrate (304 stainless steel)	1.0-3.2	8.02	3.827

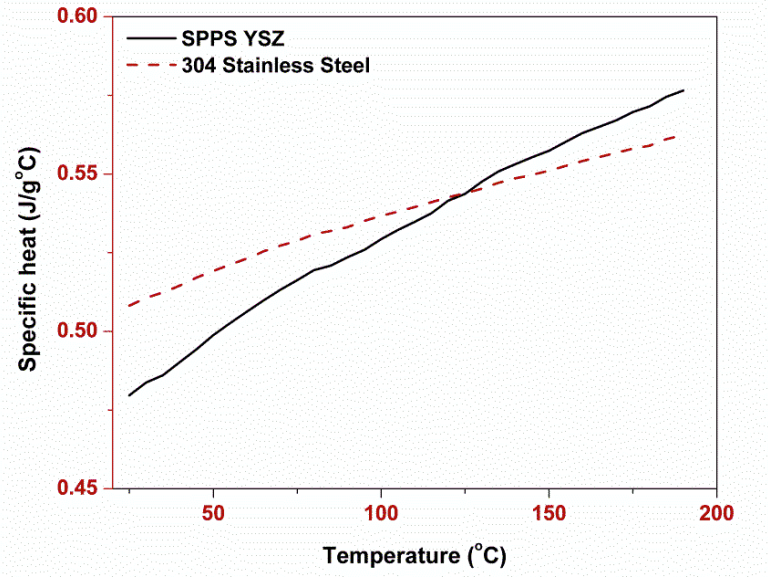

Fig. 3-8 Specific heat data of the SPPS YSZ topcoat and the 304 stainless steel substrate

Fundamental physical properties of both ceramic layers and metallic substrates were essential to laser-flash measurement, especially when double-layer models were used, and should be gathered beforehand. Thickness, density and thermal diffusivity values are tabulated in **Table 3-5** and the specific heat displayed in **Fig. 3-8**. Please note if not specifically indicated, SPPS YSZ topcoats with IPBs used for characterization were all sprayed with deposition conditions specified in **Table 3-6**, which were determined to produce SPPS YSZ TBCs with the most prominent IPB feature.

Table 3-6 Recommended spray parameters for producing optimized IPBs

Plasma gun		Metco 9MB
Plasma gun nozzle		GP
Plasma conditions	Current and voltage	650 A and 70 V
Precursor solution	Precursor solution	Aqueous yttrium nitrate/zirconium acetate

feeding	Feed rate	50 mL/min
	Precursor injection	Atomizing nozzle (FC4 Inj., 1501 Cap)
	Atomizing pressure	20 Psi
Robot movement	Scan speed	800 mm/s
	Scan distance	400 mm
	Raster scan step size	2 mm
Specimen specifications	Standoff distance	41.3 mm (1.625 in.)
	Preheat passes	10
	Spray passes	Depending on coating thickness
	Cooling	1 min pause for every 5 passes

After the optimal spray conditions were determined, it was then possible to produce repeatedly, in 20 consecutive spray trials, SPPS YSZ TBCs with IPBs, and a thermal conductivity of 0.623±0.052 $W \cdot m^{-1}K^{-1}$ was obtained (**Fig. 3-9**). This value is approximately half of that of a typical APS TBC [9] and is equal to or less than most second generation TBC compositions in commercial use.

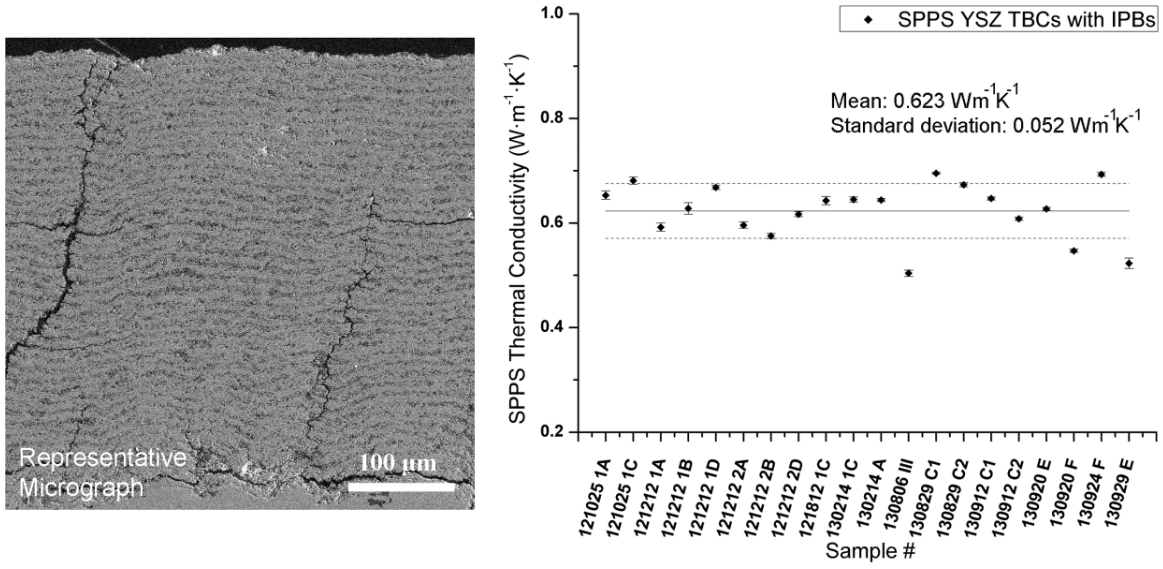

Fig. 3-9 Repeatability of producing IPBs using SPPS process

3.5 Thermal ageing effects on the layered porosity and thermal conductivity

The sintering-induced loss of strain tolerance and deterioration of durability as well as thermal conductivity have been one of the major factors that limit the application of traditional TBC

systems in the next-generation gas turbine engines. After the deposition of SPPS YSZ TBCs with thermal-conductivity-reducing IPBs, it becomes necessary also to characterize how the layered porosity would respond to the thermal ageing after it is exposed to above-service temperatures for an extended period of time, and how the thermal conductivity would change accordingly.

A series of thermal ageing experiments were conducted by annealing both monolithic SPPS IPB YSZ coatings and APS YSZ coatings in 1150°C/1250°C/1350°C tube furnaces for 50 hours, with thermal conductivity and microstructure characterizations before and after each thermal ageing experiment. According to the high-magnification cross-sectional images, even after an exposure to 1350°C for 50 hours, the IPB features were retained (**Fig. 3-10b)**. Other microscopic changes were observed though, in comparison to the as-sprayed SPPS TBCs, that the amount of submicron porosity and cracking disappeared due to sintering, leading to a much *cleaner* cross-sectional microstructure. Therefore, the thermal conductivity was expected to increase in response to the loss of submicron features and grain coarsening [64].

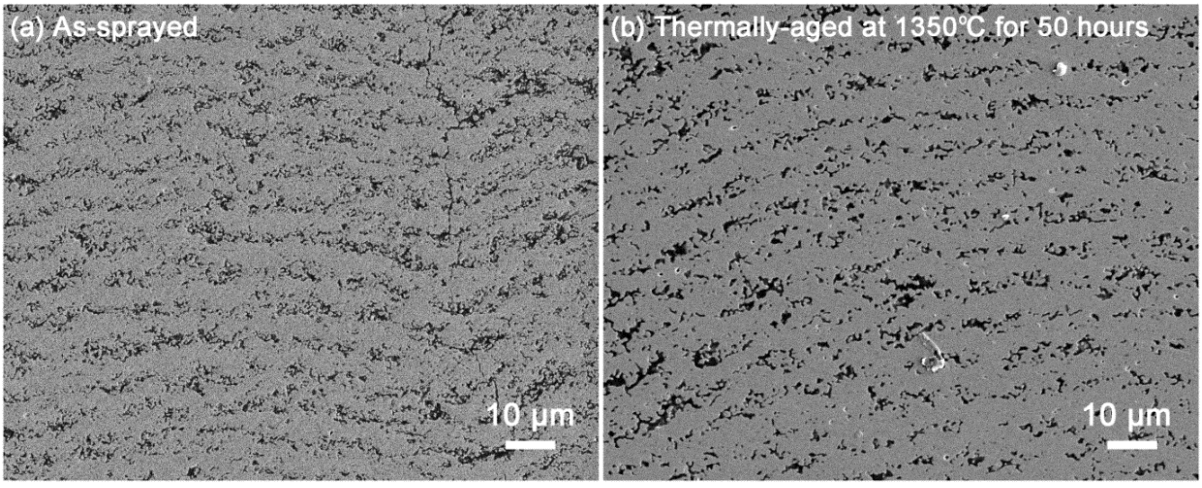

Fig. 3-10 Cross-sectional images of SPPS IPB YSZ (a) before and (b) after 50-hour thermal ageing at 1350°C

The subsequent laser-flash measurements confirmed the increase of thermal conductivity in both SPPS and APS TBCs after thermal ageing, as demonstrated in **Fig. 3-11a**. If compared within the each temperature group, all SPPS YSZ TBCs with IPB features still maintained a much lower absolute thermal conductivity values than APS baseline samples, even after extensive exposures to the above-service temperatures. This implies that despite the loss of submicron porosity (**Fig. 3-10**), the remaining IPB features composed of larger pores were still capable of significantly disrupting the out-of-plane heat conduction, reinstating the validity of thermal conductivity reduction through porosity layering. It is also worth mentioning that among all temperature groups, absolute thermal conductivity increases in SPPS YSZ TBCs was remarkably less than those in the APS counterparts in the 1150^{o}C test. Only at much higher sintering temperatures (1250^{o}C and 1350^{o}C) was the increase of thermal conductivity in SPPS TBCs comparable to or greater than the APS baseline. The suppressed thermal conductivity increases at lower temperatures may be attributed to the presence of ultra-fine splats (diameter <2μm and thickness <1μm) in SPPS TBCs [99], and enhanced sintering resistance below 1250^{o}C [106], compared to the conventional APS TBCs.

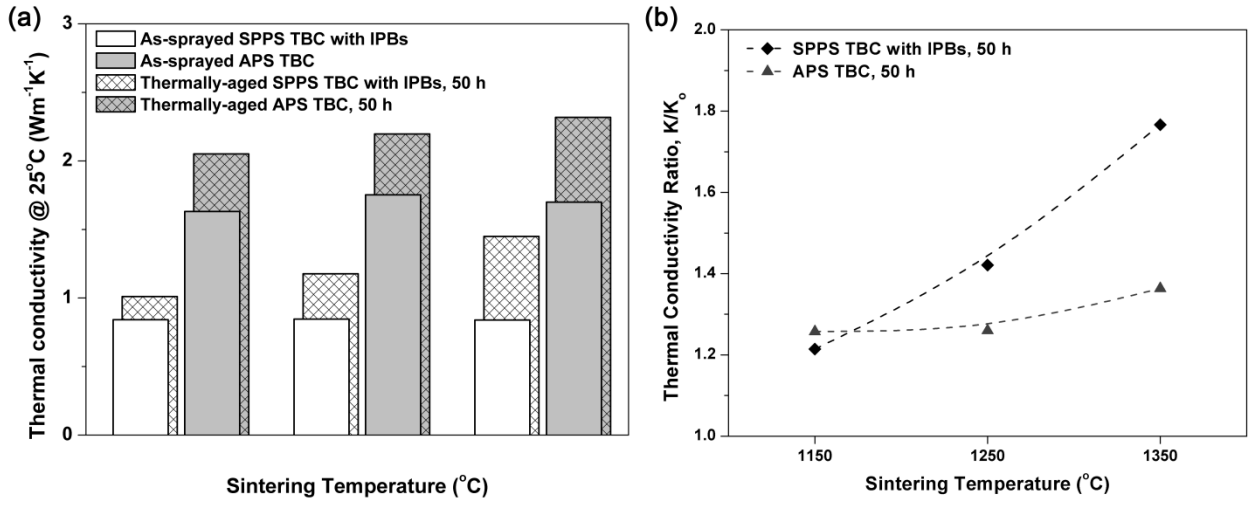

Fig. 3-11 Change of thermal conductivity in both SPPS IPB and APS YSZ TBCs displayed as (a) absolute and (b) relative values, after extensive thermal ageing at 1150°C, 1250°C and 1350°C

To look at the thermal ageing effect on IPB features from a different perspective, the relative thermal conductivity change of each TBC systems, expressed as the ratios of thermal conductivity after thermal ageing as opposed to before (K/K_o), were also plotted against various sintering temperatures in **Fig. 3-11b**. It was then apparent that the increase of thermal conductivity in SPPS YSZ with IPBs experiences an accelerated trend as the sintering temperature is increased, unlike the APS baseline samples which only suffer a moderate rise in relative values. The large relative changes of thermal conductivity in SPPS YSZ TBCs with IPBs were probably due to the much lower thermal conductivity values to begin with. It would be ideal also that if time permits more sintering experiments are performed with various extended ageing periods, such as 100 h or 150 h, to show whether the sintering effect will reach saturation.

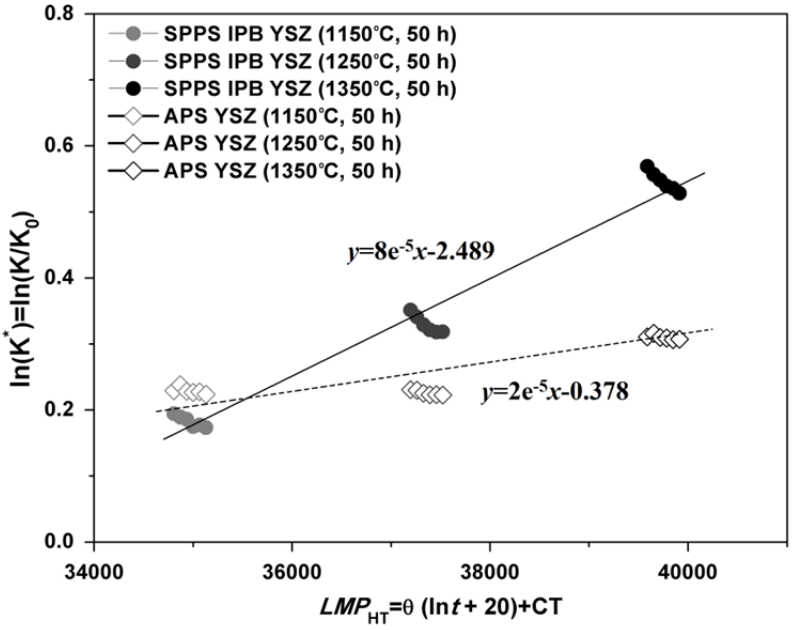

Fig. 3-12 Relationship between normalized thermal conductivity and temperature-dependent Larson-Miller parameters measured for SPPS and APS YSZ TBCs at different sintering temperatures

Larson-Miller plots are usually employed to demonstrate the materials property change subject to thermal ageing, and help to predict the performance at other service conditions. According to a study by Tan et al [137], a similar plot between a temperature-dependent Larson-Miller parameter (LMT_{HT}) and a normalized thermal conductivity value (K^*) was constructed in **Fig. 3-12** for both SPPS YSZ with IPBs and APS YSZ baselines, in which

$$K^* = K^*(T, t, \theta) = \frac{K}{K_o} \qquad (22)$$

$$LMP_{HT} = \theta(\ln t + 20) + CT \qquad (23)$$

Where K = thermal conductivity, K_o = thermal conductivity before thermal ageing, T = service/measurement temperature of coatings, θ = sintering temperature, t = exposure time and C = 2.6 [137]. The relative trends for SPPS and APS TBCs were similar to those observed in **Fig. 3-11b**, as a much steeper trend line was measured in SPPS YSZ with IPBs ($y = 8 \times 10^{-5}x - 2.489$). An interesting feature, though, was that in each cluster of data points the normalized thermal conductivity tends to decrease with the temperature at which the thermal conductivity was measured (shown in **Fig. 3-12** as declining Larson-Miller parameters within each data set), which implies that at much higher service temperatures (limited only up to 150^{o}C in this study due to equipment capability), the reduction in thermal conductivity will somewhat compensate for the effect of deteriorating microstructures, and for SPPS YSZ with IPBs, in which the reduction phenomenon is more prominent, the normalized thermal conductivity can be lower.

3.6 Erosion performance

To gain commercial acceptance of novel TBC systems including the low thermal conductivity SPPS YSZ TBCs with IPBs, it is important to demonstrate that other engine critical properties

are not compromised and should perform at least similar to the widely used APS YSZ, if not much better. To this end, preliminary erosion, bond strength, and thermal cyclic durability tests were conducted.

Care was taken to only include samples with 20% or lower porosity in the erosion test, as it was expected that higher porosity would lead to poor erosion resistance and the resulted low thermal conductivity that cannot be fairly compared to that of a standard APS TBC. An erosion test was performed on an OEM APS TBC baseline and an SPPS TBC with IPBs, the porosity and conductivity of which were 19.8% and 0.612 $W \cdot m^{-1}K^{-1}$. The SPPS specimens were sprayed on OEM single-crystal super-alloy buttons with LPPS MCrAlY bondcoats, same as the baseline sample. **Fig. 3-13** shows the results of the erosion test in which the erosion rate (in forms of coating mass loss) of SPPS YSZ TBCs with IPBs is no greater than that of the OEM APS TBC baseline at both 30^o and 90^o impingement angles, demonstrating an at least equivalent erosion resistance to APS YSZ if not better, and no additional deterioration occurred due to the introduction of IPBs.

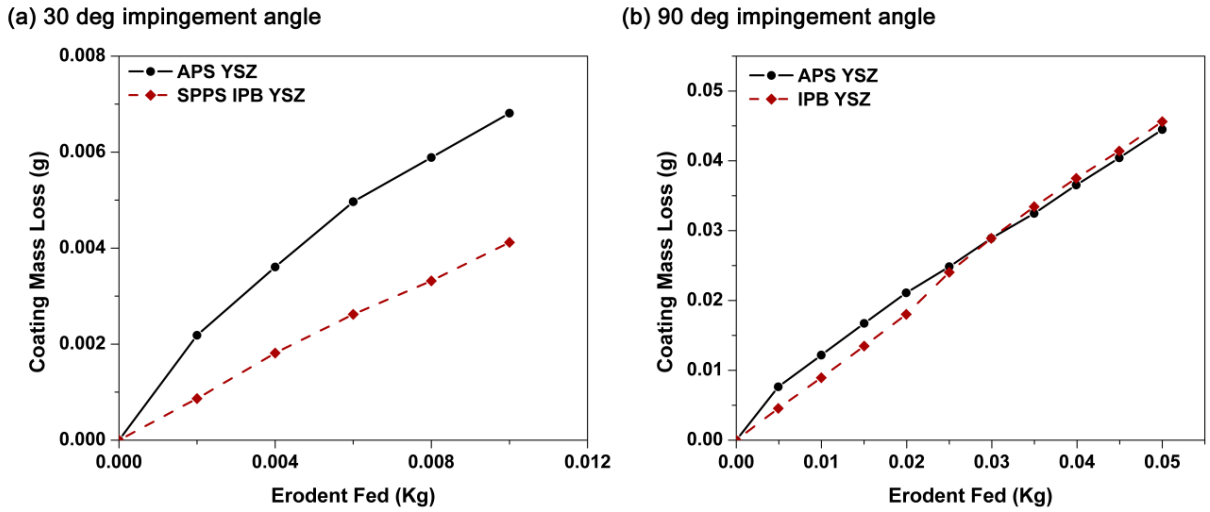

Fig. 3-13 Erosion performance of the APS YSZ baseline, and the SPPS YSZ TBC with IPBs at (a) a 30^o impingement angle, and (b) at a 90^o impingement angle

3.7 Bond strength characterization

The bond strength tests are typically employed to characterize the adhesion or cohesion strength of thermal barrier coatings [126]. The results of the tests are summarized in **Table 3-7**.

Table 3-7 Summary of the bond strength test results on SPPS IPB YSZ and APS YSZ

Sample#	Material	Max. stress (psi)	Failure location		
			Top coat	Bond coat	Topcoat/bond-coat interface
#1	SPPS YSZ with IPBs	859	20%	30%	50%
#2	SPPS YSZ with IPBs	54	35%	15%	50%
#3	SPPS YSZ with IPBs	742	20%	30%	50%
#4	APS YSZ	3949	0%	0%	100%
#5	Epoxy (FM1000)	12614			

The exceptionally low stress value of sample #2 seems like an anomaly. After the cross-sectional characterization, #2 is found to be no different than other SPPS samples in terms of microstructure, but given the fact that a greater topcoat failure area is exposed after failure (**Table 3-7**), it's likely that some horizontal cracks that pre-exist in the ceramic topcoat could cause the early delamination. This result suggests that in an industrial application there would need to be a microstructural specification to prevent the acceptance of samples like #2 and that it is necessary to discover how to avoid spray conditions leading to such a microstructure. The failure site for other SPPS IPB YSZ samples (#1 and #3) is found to be along IPBs, approximately 50-100μm above the topcoat/bond-coat interface. This suggests that the layered porosity is the weak spot of the whole TBC system and may compromise some mechanical properties. Though it is not ideal, the bond strength of SPPS IPB YSZ TBCs is still within the acceptable range specified by the OEMs.

3.8 Cyclic thermal durability

To characterize TBCs' performance under typical engine drastic heating/cooling conditions and confirm the acceptable durability, a cyclic furnace test was conducted using a one-hour cycle, consisting of 5 minutes heating, 50 minutes dwelling at 1121^{o}C and a 5 minutes forced air cooling down to below 100^{o}C. In this test, cyclic thermal durability was characterized on 10 specimens (all deposited on single-crystal super-alloy buttons with HVOF MCrAlY bond-coats, **Table 2-2**), which include six SPPS YSZ TBC pieces with or without APS YSZ inner layers, two APS TBC pieces as a baseline and two SPPS YSZ TBC pieces with IPBs on a 25μm APS YSZ inner layer (**Fig. 3-14**). The YSZ TBC specimens with IPBs have significantly better durability than OEM APS baselines, and comparable durability to SPPS TBCs with no IPBs. This result indicates that the stress-relieving vertical cracks are capable of enhancing the coatings' durability, and at the same time the layered porosity, IPBs, doesn't introduce additional failure modes.

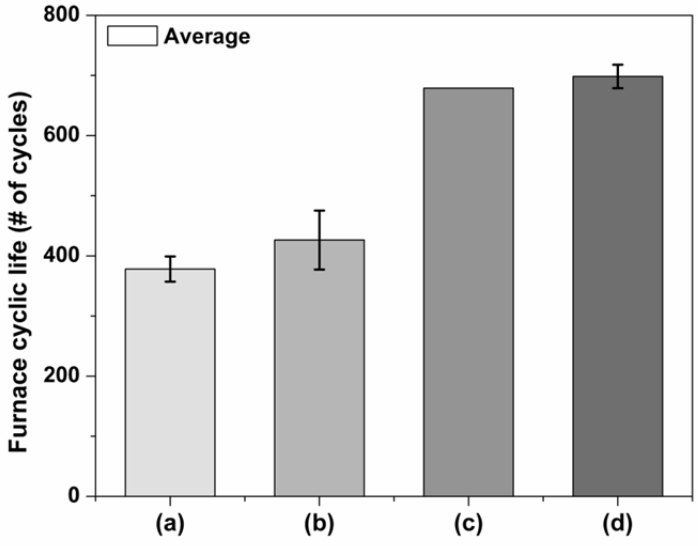

Fig. 3-14 Cyclic furnace testing of (a) 250μm APS YSZ, (b) 200μm SPPS YSZ with a 25μm APS YSZ inner layer, (c) 250μm SPPS YSZ with IPBs on a 25μm APS YSZ inner layer, and (d) 250μm SPPS YSZ

Chapter 4. Double-layer SPPS GZO/YSZ TBCs

4.1 Precursor solution characterization

As mentioned earlier, precursor solutions with high molarity, manageable viscosity (depending on the delivery system), predominantly exothermic decomposition reactions, and minimal abrupt release of gases are best suited to the SPPS process. In order to help anticipate and understand the deposition of the GZO PSL, a set of thermal and rheological characterizations have been previously proven to be effective for aiding in depositing YSZ TBCs and magnesia/yttria composites [67, 138] and were employed for the development of the double-layer SPPS GZO/YSZ TBCs as well.

Since the primary component of both GZO and YSZ precursor solutions is zirconium acetate solution, their thermal properties were shown to be similar in DSC-TGA tests (**Fig. 4-1**), in the sense that both exhibited predominantly exothermic decomposition reactions above 250^{o}C. The major difference between the two precursor solutions though was the amount of nitrates mixed in each solution. The relative concentration of the oxidizer (nitrate) and the reducer (acetate) in the precursor solution determines the degree of the redox reaction, and maximum exothermic heat is typically expected when an ideal stoichiometry is reached. Both YSZ and GZO precursors were calculated to be predominantly fuel-rich [139] in this case, with GZO slightly close to the perfect stoichiometry. However, because of the heavy molecular weight of gadolinium, the GZO precursor with 50% gadolinium nitrate content had a lower *energy density* (heat per gram dried precursor gel), and therefore the total amount of exothermic energy was still lower than YSZ precursor (**Table 4-1**). In addition, a vigorous combustion reaction associated with high nitrate content is known to produce particles that are too fine to be deposited onto the substrates due to a

small Stokes number [87] leading to many particles following the gas stream off the substrate instead of impacting it.

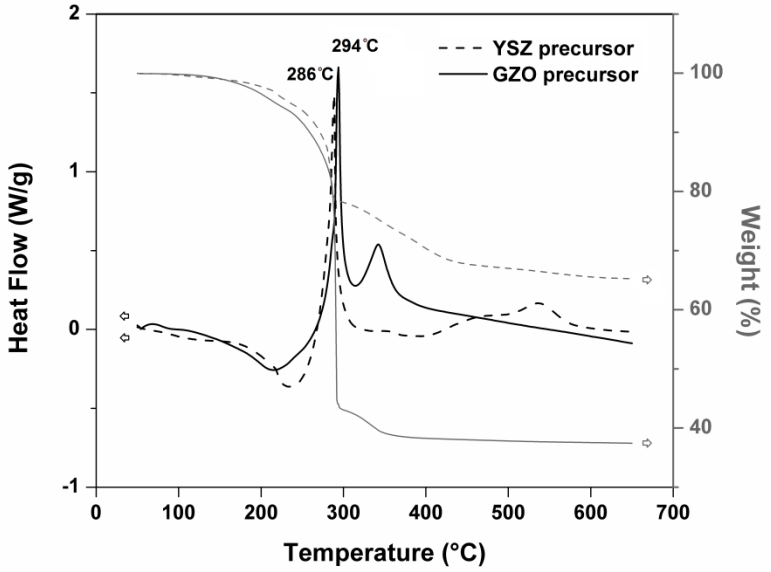

Fig. 4-1 Thermal characteristics of GZO and YSZ precursor solutions

Surface tension (**Table 4-1**) will influence the droplet breakup mechanism during atomization, thus affecting the particle dimension and size distribution, heat transfer, entrainment and overall microstructure of deposited coatings [87, 131]. Because of the high nitrate content in GZO precursor, the gas-releasing reactions and the subsequent particle break-up events were anticipated to be more violent, and a higher surface tension was therefore expected to be more favorable, unlike the case of the acetate-based YSZ precursor. The GZO precursor solution with a higher surface tension was expected to produce larger particles after the air atomization and violent outgassing pyrolysis, which would lead to the enhanced particle entrainment to the hot inner core of plasma plume, full pyrolysis and melting of decomposed particles, and in return compensate for the disadvantages of using higher nitrate content. It was unclear though which of competing dynamics or chemical factors would be dominant before any actual spray trials.

Table 4-1 Fluid and thermal properties of GZO and YSZ precursor solutions

Precursor	Dynamic viscosity (cP)	Surface tension (mN/m)	Endothermic heat* (J/g)	Exothermic heat* (J/g)	Net heat* (J/g)
GZO	6.04	69.37	-121.8	368.7	246.9
YSZ	6.16	52.65	-33.4	419.1	385.7

*Heat = heat from decomposition reactions

4.2 Double-layer TBC deposition and microstructural characterization

In the double-layer TBCs, the low thermal conductivity SPPS YSZ inner layer was deposited using the same spray conditions listed in **Table 3-6**. The repeatability was proven viable in this study as microstructures containing the typical IPB feature, layered porosity, were obtained (**Fig. 4-2c**).

Based on the extensive optimization work on the IPB microstructure, some general conclusions about the SPPS process development on future TBC materials are listed as follows:

(i) The atomizing nozzle typically gives more porous coatings than the stream injection;

(ii) Smaller raster scan spray index provides better delineated IPBs, but can lead to overheating that requires extra cooling;

(iii) Smaller standoff distance gives more prominent IPBs, but may also cause overheating;

(iv) Increased feed rates will increase porosity and give thicker IPBs;

(v) Development of alternating low and high feed rates every 5 coating passes with 1 minute rest in between can significantly prevent the occurrence of overheating; and

(vi) Lowering the atomizing gas pressure increases coating density but only up to a point.

In light of these helpful guidelines, the deposition of the GZO protective surface layer (PSL) was performed with no additional treatment on the SPPS YSZ inner layer, except for moderate preheating (5-10 passes). Given the general similarity between GZO and YSZ in the precursor

screening, especially in terms of dynamic viscosity and net heat (**Table 4-1**), the processing parameters for GZO PSLs were derived from the parameters that were applied successfully for SPPS YSZ TBCs with IPBs (**Table 3-6**); however, the feed rate, the stand-off distance and cooling setup had to be adjusted accordingly to achieve the desired microstructure. By utilizing graphite planchets that can be burnt off above 600^{o}C, the calculation involving the weight and density of monolithic GZO coating revealed an approximate porosity of 15vol% porosity, and in using this method, all types of porosity are included. Through-thickness vertical cracks (inear density: 180μm^{-1}) was produced for SPPS GZO PSLs (**Fig. 4-2b**). All corresponding deposition conditions for the SPPS GZO layer are summarized in **Table 4-2**.

Table 4-2 Recommended process conditions for depositing GZO PSLs

Parameter	Recommended value
Plasma gun	Metco 9MB
Plasma gun nozzle	GP
Plasma current and voltage	650 A and 70 V
Primary gas/secondary gas	Ar/H2
Precursor solution	Aqueous gadolinium nitrate/zirconium acetate
Liquid injection mode	Atomizing nozzle (FC4 Inj., 1501 Cap)
Atomizing air pressure	20 psi
Liquid flow rates	20 mL/min
Standoff distances	38-45 mm
Traverse speed	450 mm/s
Raster scan step size	2 mm
Preheating	10 passes
Cooling	None

From the SEM cross-sectional image (**Fig. 4-2a**), the adhesion between the SPPS GZO PSL and the YSZ inner layer appears to be good, with no apparent pores or gaps at the interface. Also important is the fact that desirable through-thickness vertical cracks extend from the YSZ interlayer to the GZO PSL, preserving the ability of the cracks to accommodate thermal expansion mismatch at elevated temperatures. The shared vertical cracks are able to

accommodate the thermal expansion difference between YSZ and GZO [27], minimize the thermal stress accumulated under the thermal cyclic conditions, and therefore improve the durability of the double-layer TBCs, as is seen in **Fig. 4-5**.

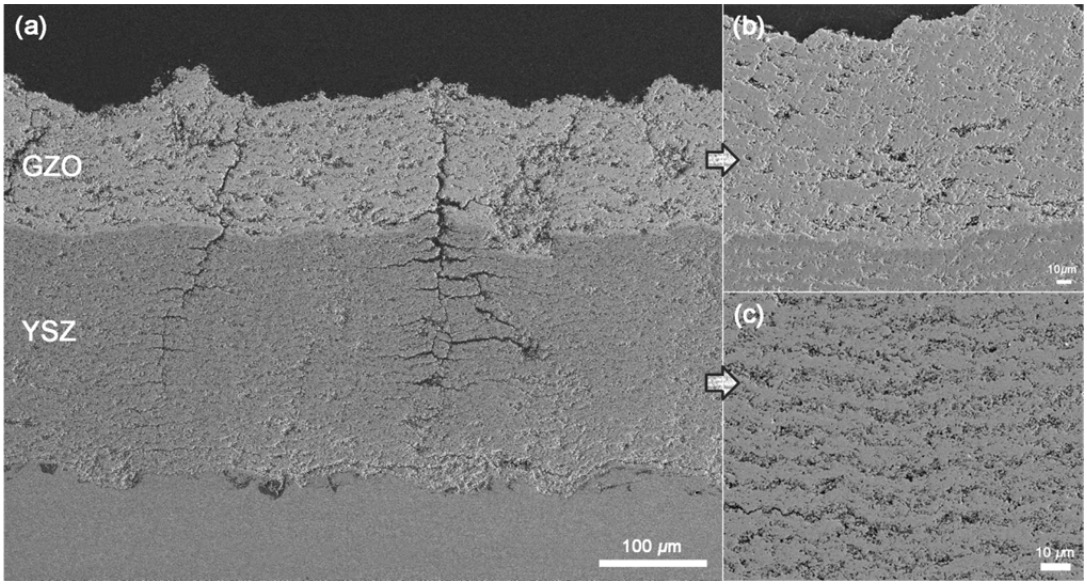

Fig. 4-2 Typical cross-sectional micrograph of double-layer SPPS TBC with a GZO protective surface layer (~100μm) and a YSZ interlayer with conductivity-reducing IPBs (~200μm)

Regarding the target thickness of each layer, Lee et.al not only mentioned that the double-layer GZO/YSZ structure could alleviate the overall compressive stress in TBCs, but also claimed the stress state was insensitive to the ratio of top-/bottom-layer thickness, unless the ratio was around 1:1 [140]. Considering the cost and the poor erosion resistance of GZO [42], the thickness ratio between the GZO PSL and the YSZ interlayer was kept at 1:2. However, this can be easily adjusted in future by altering the number of deposition passes for each layer.

4.3 Phase determination of as-sprayed GZO PSLs

Zirconates are known to form ordered pyrochlore or disordered fluorite structures at varying temperatures [37, 141]. GZO is no exception, as the high-temperature stable fluorite phase tends

to thermodynamically transform into pyrochlore with a gradual cooling [142]. However, a rapid-solidification process such as the plasma spray (10^6 $K \cdot s^{-1}$ or higher [143]), together with the complicated physical and chemical reactions associated with the precursor solutions, can lead to the preservation of metastable phases in the as-deposited coatings. **Fig. 4-3** shows the X-ray diffractogram of the as-sprayed SPPS GZO PSLs, in which the primary peaks suggest the predominant presence of the metastable fluorite phase, while the characteristic superlattice peaks of the pyrochlore phase, (311), (331) and (511), appear to be extremely weak. This suppressed formation of highly-ordered pyrochlore phase in as-sprayed SPPS GZO is in accordance with the observations from both APS [42] and EB-PVD [144] processes.

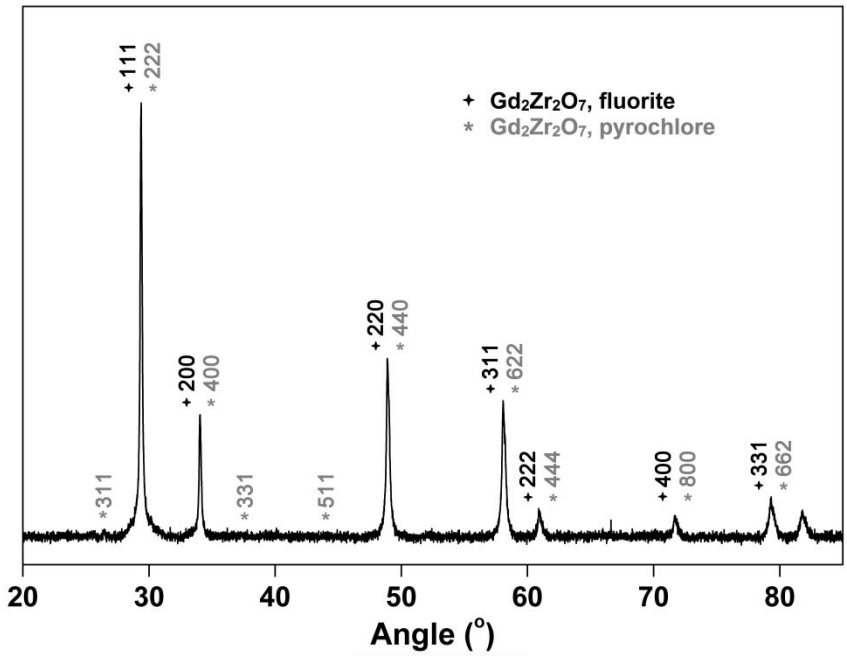

Fig. 4-3 XRD pattern of the as-sprayed GZO PSL

4.4 Thermal conductivity determination using the laser-flash method

The importance of low thermal conductivity TBC systems has been emphasized in previous chapters. Bulk YSZ has a thermal conductivity of 2.3 $W \cdot m^{-1}K^{-1}$ at elevated temperatures, but this

value can be reduced significantly through process and microstructure engineering [100], and even be optimized to as low as 0.63 $W \cdot m^{-1}K^{-1}$ by the introduction of IPBs using the SPPS process [122]. GZO (both pyrochlore and fluorite), on the other hand, is found to exhibit a low bulk thermal conductivity of 1.6 $W \cdot m^{-1}K^{-1}$ [37], and two consecutive measurements on two different as-sprayed SPPS GZO PSLs in this study yielded an average thermal conductivity to be 0.53 $W \cdot m^{-1}K^{-1}$ (**Fig. 4-4**). The lower thermal conductivity of both SPPS layers compared to APS YSZ ensured an overall low thermal conductivity in the double-layer TBC system.

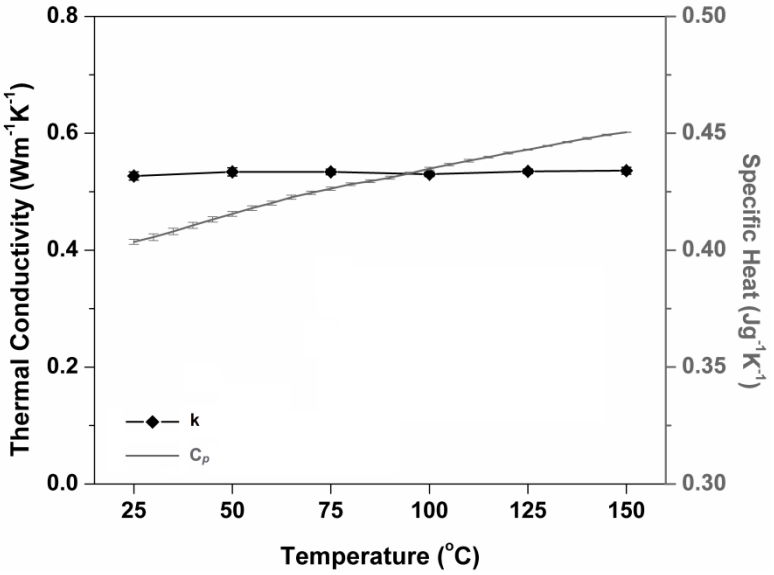

Fig. 4-4 Thermal conductivity and specific heat for the as-sprayed SPPS GZO PSL

4.5 Cyclic thermal durability

The earlier tests dedicated to low-thermal-conductivity SPPS YSZ TBCs with IPBs has demonstrated a promising durable performance [122]. To characterize the cyclic thermal durability of the double-layer SPPS GZO/YSZ TBCs, three different TBC systems (APS YSZ supplied by OEM, SPPS YSZ with IPBs, and SPPS GZO/YSZ double-layer) were tested side by

side in one-hour cyclic furnace tests set at 1121 ^{o}C, and the performance was evaluated based on the cyclic lifetime and spallation mechanism.

By comparing the cyclic lives against the APS YSZ baseline samples, it's clear in **Fig. 4-5a** that SPPS TBCs exhibit improved durability, even though the relatively thicker SPPS TBCs would theoretically store more strain energy and have shorter cyclic lifetime. The average lifetimes of the SPPS TBCs (both the SPPS YSZ with IPBs and the double-layer SPPS GZO/YSZ), on the other hand, are comparable, indicating no notable deterioration of thermal cyclic durability is caused by the lower toughness of GZO PSLs [55].

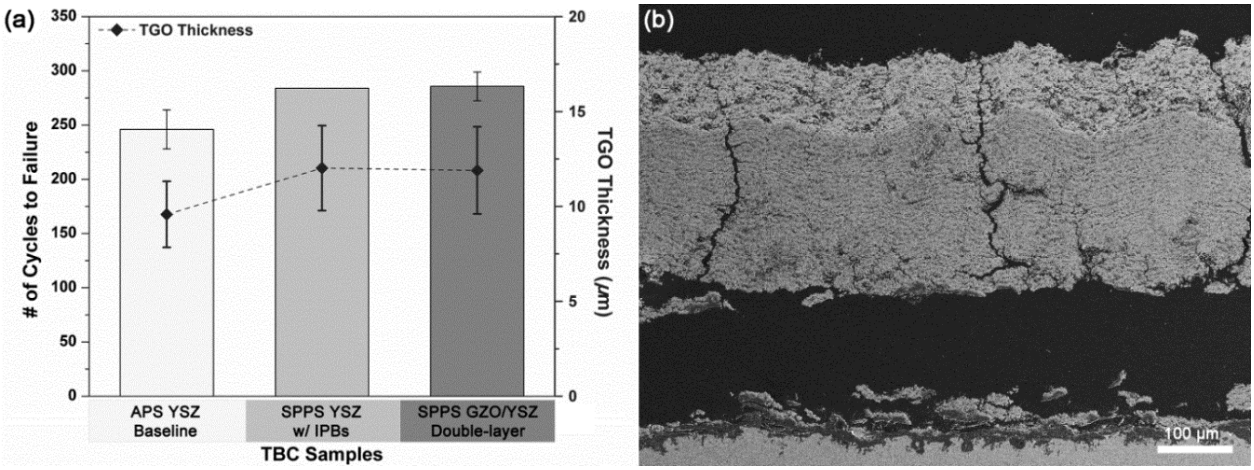

Fig. 4-5 (a) Summary of thermal cyclic durability and TGO thickness results based on a cyclic furnace test consisting of two OEM APS YSZ baseline, one SPPS YSZ with IPBs and four SPPS GZO/YSZ double-layer TBCs, and (b) failure mode of the SPPS double-layer TBC

Spallation is found to be at the YSZ/TGO interface in all cases (**Fig. 4-5b**), and durability is likely to be governed by the stresses in the ceramic, associated with the TGO thickening and the interface roughening. According to the measured TGO thickness at failures (**Fig. 4-5a**), SPPS coatings that have the stain-tolerant vertical cracks withstand somewhat thicker TGOs compared to APS OEM coatings. The stress relieving vertical cracks also help to stabilize the GZO/YSZ interface for the double-layer TBCs, which could be crack initiation sites due to the thermal

expansion mismatch and the different sintering rates as seen in APS coatings of this same type [142], but as shown in the cross-sectional micrograph stay almost intact without visible signs of crack initiation or propagation.

Chapter 5. Al_2O_3/TiO_2-doped SPPS YSZ TBCs

The idea behind doping YSZ TBCs with Al_2O_3/TiO_2 using the SPPS process, which was first proposed by A. Aygun et al. [45], is to incorporate Al_2O_3 and TiO_2 in a solid solution of YSZ. An abundant supply of Al_2O_3 in the solid solution helps to alter the CMAS composition and increases its propensity for crystallization (**Fig. 5-1**) when the attack of environmental deposits occurs. The CMAS test in the isothermal furnace confirms the validity of this hypothesis, but suggests that only through the co-doping of Al_2O_3 and TiO_2 would this method be effective. TiO_2, which functions as a nucleating agent, arrests the CMAS penetration front by allowing the new anorthite phase to rapidly crystallize.

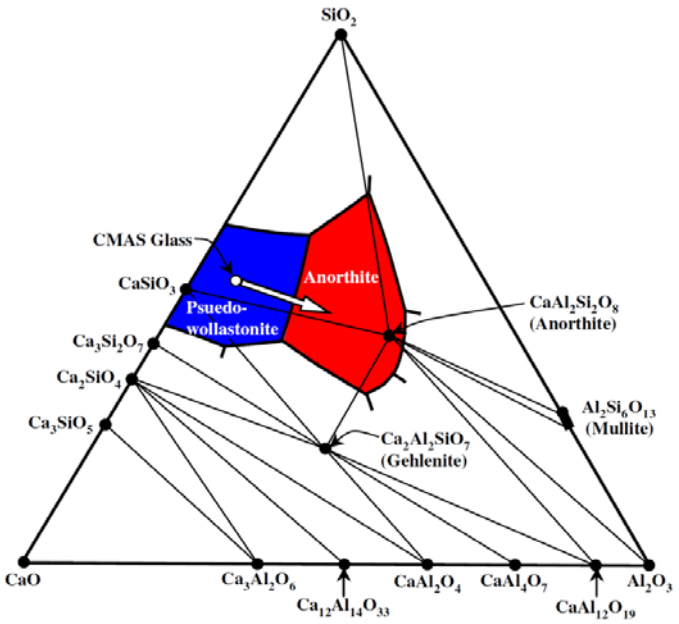

Fig. 5-1 CaO-Al_2O_3-SiO_2 ternary phase diagram showing the composition of simulated CMAS and the anorthite field [45]

Regarding the maximum Al_2O_3 solubility in the ZrO_2-based solid solutions, an earlier study on the ternary Al_2O_3-ZrO_2-Y_2O_3 system indicated that a miscibility of 20 mol%Al_2O_3 was feasible through the SPPS process, while the emergence of crystalline Al_2O_3 was observed in the sub-

micron *t*-ZrO_2 regions where the Al content was higher [145]. On another note, dense Al_2O_3-40wt% YSZ nanocomposite coatings were also produced by the SPPS process with the suppressed grain growth presenting a homogeneous cross-sectional morphology [146], due to the formation of ultra-fine splats and the rapid cooling of plasma spraying in general. A complication to producing the solid-solution Al_2O_3/TiO_2-doped SPPS YSZ TBCs is that the deposition conditions were not specified in the original journal paper, so to reproduce the doped coating using the SPPS process, we had to initiate a bottom-up thermal spray study with new precursor solutions, starting from the deposition of Al_2O_3-doped YSZ TBCs.

5.1 Precursor solution characterization

5.1.1 For Al_2O_3-doped SPPS YSZ TBCs

As mentioned in the previous sections, thermal characteristic and fluid properties of precursor solutions are important to the initial process development of new composition SPPS TBCs. Aluminum nitrate, as the most readily available and cheap aluminum salt on the market, was utilized as the Al_2O_3 source. **Fig. 5-2** summaries the DSC-TGA results of three different Al_2O_3-mixed YSZ precursors (20%, 25% and 50% additions), as well as a pure YSZ solution. An interesting discovery is the onset temperature of the major exothermic events during pyrolysis shift to the higher end, as the addition of aluminum nitrate increases. As the in-flight velocity of particles in the plasma plume is typically 100-250m/s for Metco 9MB gun [147], little time is available for heat transfer to the droplets and particles. Considering the amount of energy needed for solvent evaporation and the rapid temperature drop in the downstream plasma jet, a low exothermic onset temperature will generally be favorable in terms of full particle pyrolysis and melting in the SPPS process. Another apparent trend in the thermal characteristics is that as the

dopant level increases, the endothermic peaks at lower temperatures augment significantly, while the exothermic peak at higher temperatures disappears (highlighted by the arrows). In fact, as displayed in **Table 5-1**, the net decomposition heat changes from mostly exothermic in the pure YSZ precursor to predominantly endothermic in 50mol% Al_2O_3-doped YSZ. This is likely to be the result of the drastic endothermic decomposition reaction of nitrates in general, and similar results were observed previously in other nitrate-rich precursor solutions [67]. The endothermic behavior of precursors will produce un-melted particles, and thereby lead to a multitude of problems, such as porous microstructures and poor deposition efficiency.

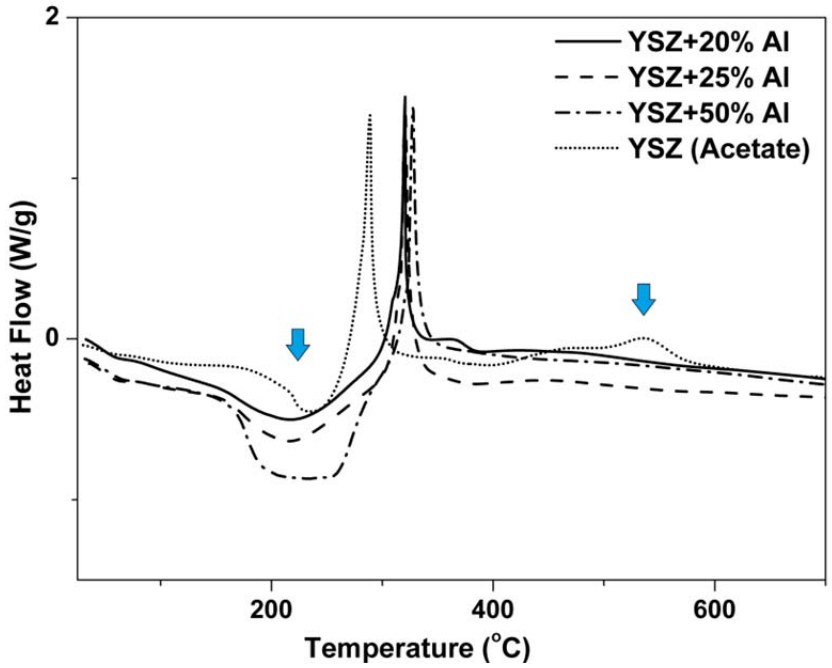

Fig. 5-2 DSC-TGA heat flow profiles of YSZ precursors with different Al_2O_3 doping levels: 0%, 20%, 25%, and 50%

In **Table 5-1**, the viscosity of Al_2O_3-doped YSZ precursor solutions increases remarkably as more nitrates are added. Increased viscosity will cause difficulties for fluid delivery. Generally speaking, aluminum nitrate based precursor solutions tend to be problematic for the SPPS

process, so do the spray trials demonstrate later on. A possible cure for this disadvantage is to find other alternative aluminum sources, but then instead solubility is likely to be a greater issue.

Table 5-1 Thermal characteristics and viscosity of YSZ precursors with different Al_2O_3 doping levels: 0%, 20%, 25%, and 50%

Precursor	Kinematic viscosity (cSt)	Endothermic heat* (J/g)	Exothermic heat* (J/g)	Neat heat* (J/g)
YSZ	4.96	-33.4	419.1	385.7
YSZ + 20% Al_2O_3	N/A	-185.8	147.2	-38.6
YSZ + 25% Al_2O_3	5.39	-203.5	134.2	-69.3
YSZ + 50% Al_2O_3	14.11	-387.8	117.7	-270.1
*Heat = heat from decomposition reactions				

5.1.2 For Al_2O_3/TiO_2-doped SPPS YSZ TBCs

To determine an appropriate amount of Al_2O_3 dopant in the precursor solution is not an easy task. On one hand, since the amount of dopant in the precursor directly affect the size of *Al_2O_3 reservoir* in the coating, a higher Al content is more favorable; on the other hand, the low solubility of Al_2O_3 in the ZrO_2, according to the binary phase diagram, will limit the maximum Al_2O_3 doping level for a solid solution, beyond which phase separation is inevitable, and deterioration in mechanical properties is expected. In fact the high magnification backscattered imaging on the YSZ+50% Al_2O_3 TBC showed the distinct segregation between Al_2O_3-rich and ZrO_2-rich splats in the microstructure. Therefore, the 20% Al_2O_3 content was selected for the Al_2O_3/TiO_2-doped SPPS YSZ TBCs, since it was previously reported to be both stable and effective for CMAS resistance [45, 145], and further study was performed to modify the addition of 5% TiO_2.

Precursor solutions for the Al_2O_3/TiO_2-doped SPPS YSZ TBCs were first made from titanium isopropoxide and aluminum nitrate, due to the limited variety of commercially available titanium

sources. Because titanium isopropoxide is known to be readily reactive with water, the solvent had then to be substituted with ethyl alcohol, and consequently zirconium acetate was replaced with zirconium propionate. The brand-new alcohol-based precursor exhibited completely different thermal characteristics, and was employed as our sole precursor for a while before another titanium source, the titanium (III) sulfate solution, was procured after an extensive search for alternative chemicals. Two additional water-compatible Al_2O_3/TiO_2-doped YSZ precursors were later prepared from titanium sulfate solution, while the aluminum source was changed from aluminum nitrate to either aluminum sulfate or aluminum acetate, since the oxidizers, e.g. nitrates, in this case would instantaneously oxidize Ti^{3+} and cause TiO_2 to precipitate by the hydrolysis of Ti^{4+}. The results of DSC-TGA characterization on all four precursors, including the successful standard YSZ precursor, are summarized in **Fig. 5-3**.

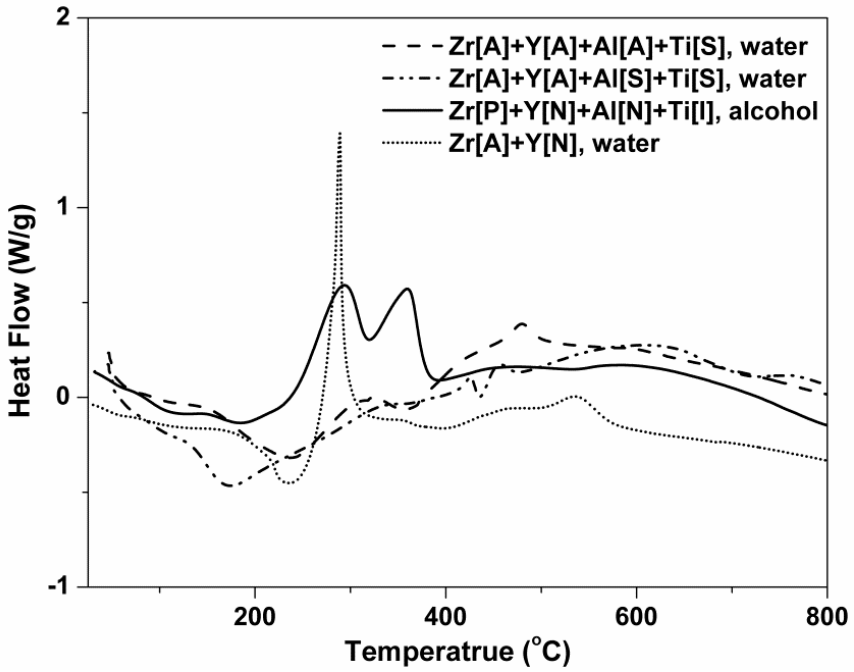

Fig. 5-3 DSC-TGA heat flow profiles of different Al_2O_3/TiO_2-doped YSZ precursors (A: acetate, P: propionate, N: nitrate, S: sulfate, and I: isopropoxide)

In **Fig. 5-3**, it's clear that the alcohol-based oxidizer/reducer mixture (Zr[P] + Y[N] + Al[N] + Ti[I]) demonstrates the most exothermic behavior, while the water-based predominantly reducer mixtures (Zr[A]+Y[A]+Al[A]+Ti[S] and Zr[A]+Y[A]+Al[A]+Ti[S]) are more endothermic. This implies that the carbon (organic) content alone doesn't suffice an exothermic precursor; certain amounts of oxidizer are essential for the optimal thermal characteristic, as a maximum energy release is expected when a perfect stoichiometry of the redox reaction is reached.

5.2 Deposition of Al_2O_3-doped SPPS YSZ TBCs

Under SEM characterization on initial spray trials of Al_2O_3-doped SPPS YSZ TBCs, the as-sprayed coatings were generally porous regardless of dopant concentration, as expected from the predominantly endothermic characteristics in precursor solutions. Therefore, tremendous efforts were devoted to increasing the density of as-sprayed TBCs.

Based on the precedent knowledge, several possible improvement approaches were explored, including modifying on the precursor chemistry, lowering precursor feed rate, reducing standoff distance and decreasing the droplet atomizing pressure.

5.2.1 Precursor chemistry: addition of PVA

The addition of chelating agents in precursor solutions strongly affects the degree of splashing and equivalent diameter of splats [148], hence influences the coating microstructure. Polyvinyl alcohol (PVA), as a common chelating agent, was employed in this case to study the effect on as-sprayed coatings. It's worth mentioning though there are different grades of PVA available commercially: depending on the molecular weight of the polymer chains, they are commonly subcategorized as low, medium and high M.W. In this study, both the low and medium molecular weight PVAs are utilized, which correspond to 10,000-26,000 and 57,000-66,000

M.W., respectively. From **Fig. 5-4** and **Table 5-2**, several changes are observed after the addition of different PVAs: (i) the precursor viscosity increases as the PVA is added, and a greater increase is observed with the higher M.W., (ii) the dwindling of endothermic peaks and emergence of additional exothermic peaks is observed in the DSC-TGA (as indicated by the arrows) as the addition of PVAs , (iii) medium MW PVA has a much stronger effect on exothermic behaviors than the low MW PVA does, and in fact the effect is so dramatic that the net decomposition is altered completely from endothermic to exothermic, and (iv) the onset temperature for major exothermic peak are shifted slightly to the lower end after PVA additions.

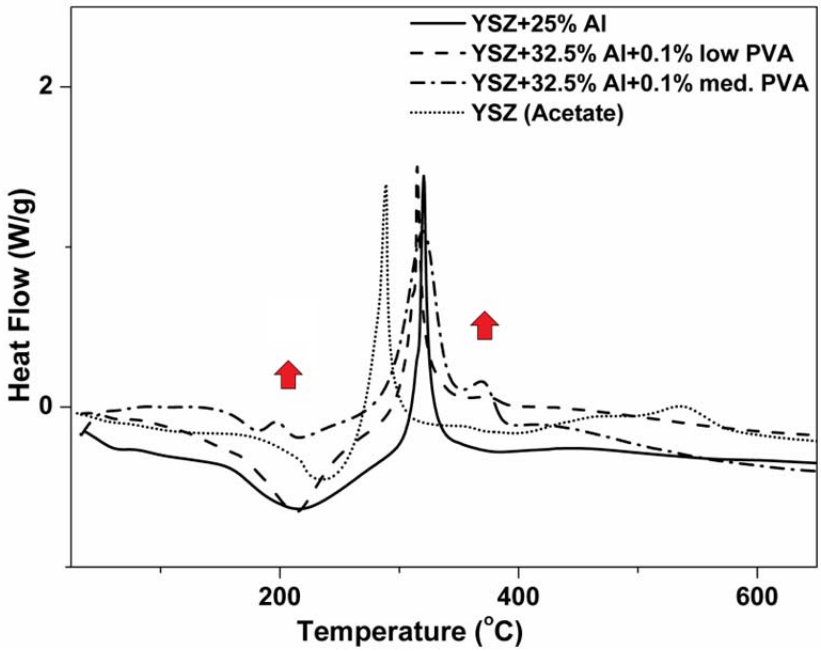

Fig. 5-4 Effect of PVA additions on the thermal characteristics of Al_2O_3-doped YSZ precursors

Phenomena (ii), (iii) and (iv) all have positive influences on precursor characteristics, in terms of improving precursors' exothermic behavior, and this influence seems to correlate with the total amount of carbon addition; which is reasonable since hydrocarbon will provide additional heat when reacts with oxidizers, in this case the aluminum nitrate. While increased precursor

viscosity (**Table 5-2**) will not only limit the maximum liquid feed rate in the delivery system, but also influence the droplet-plasma jet interaction in a way that the increased viscosity can hinder the droplet break-up and the resulted larger droplet have better entrainment to the hotter plasma jet core, leading to better melting and denser coatings.

Table 5-2 Thermal characteristics and viscosity of Al_2O_3-doped YSZ precursors with different PVA additions

Precursor	Kinematic viscosity (cSt)	Endothermic heat* (J/g)	Exothermic heat* (J/g)	Neat heat* (J/g)
YSZ	4.96	-33.4	419.1	385.7
YSZ+20% Al_2O_3	N/A	-185.8	147.2	-38.6
YSZ+32.5% Al_2O_3+0.1% PVA (Low M.W.)	6.88	-265.9	153.6	-112.3
YSZ+32.5% Al_2O_3+0.1% PVA (Medium M.W.)	11.56	-66.2	282.1	215.9

*Heat = heat from decomposition reactions

The effect of PVA additions on as-sprayed TBCs is demonstrated in **Fig. 5-5**, in which a much denser microstructure was observed. This modification to the deposition of Al_2O_3-doped SPPS YSZ TBCs accomplished the original goal; however, due to the high precursor viscosity, the liquid feed rate and the deposition rate had to be compromised.

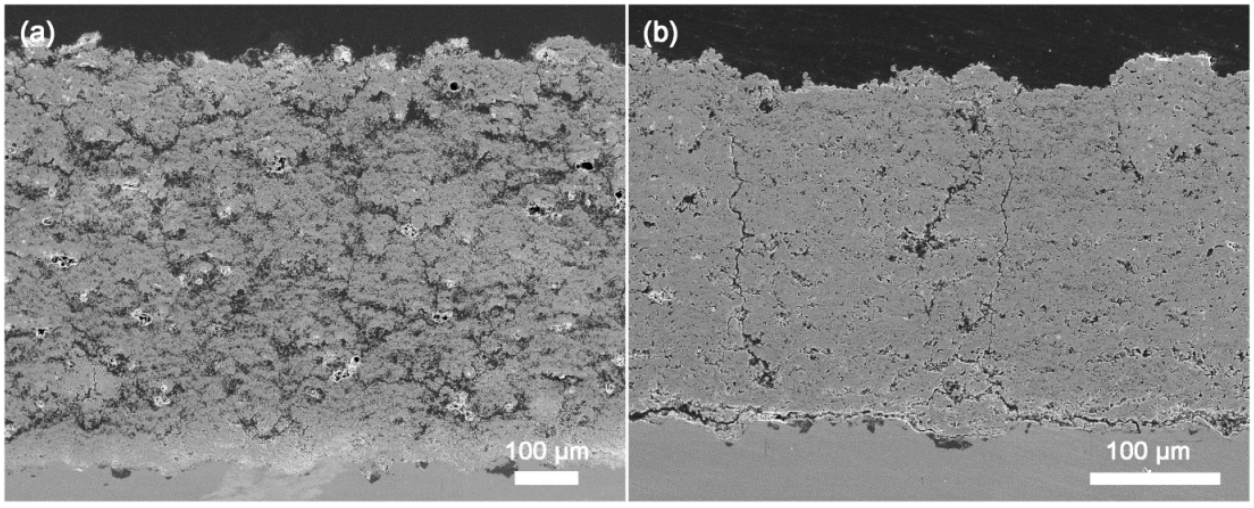

Fig. 5-5 Effect of PVA additions on the microstructure of SPPS YSZ + 32.5% Al_2O_3 TBCs: (a) no PVA addition, and (b) 0.1% PVA (Medium M.W.)

5.2.2 Precursor feed rate

Another way to produce denser SPPS YSZ is to adjust the precursor feed rate into the plasma jet. Given a fixed gun power, reduced amounts of precursor solution injected into the plasma jet will usually cost less energy for solvent evaporation, and thereby more energy for particle pyrolysis as well as melting. Full molten droplets tend to form better splat bonding, which leads to denser microstructure. As shown in **Fig. 5-6**, a reduction in feed rates from 32 mL/min to 20 mL/min did have an effect on the densification of as-sprayed TBCs, though it was not as significant as in the case of IPB since the precursor itself was predominantly endothermic. Accompanying the densification, the layered-like feature in the case of 32 mL/min also lost its prominence, following the same trend as in the development work of IPBs.

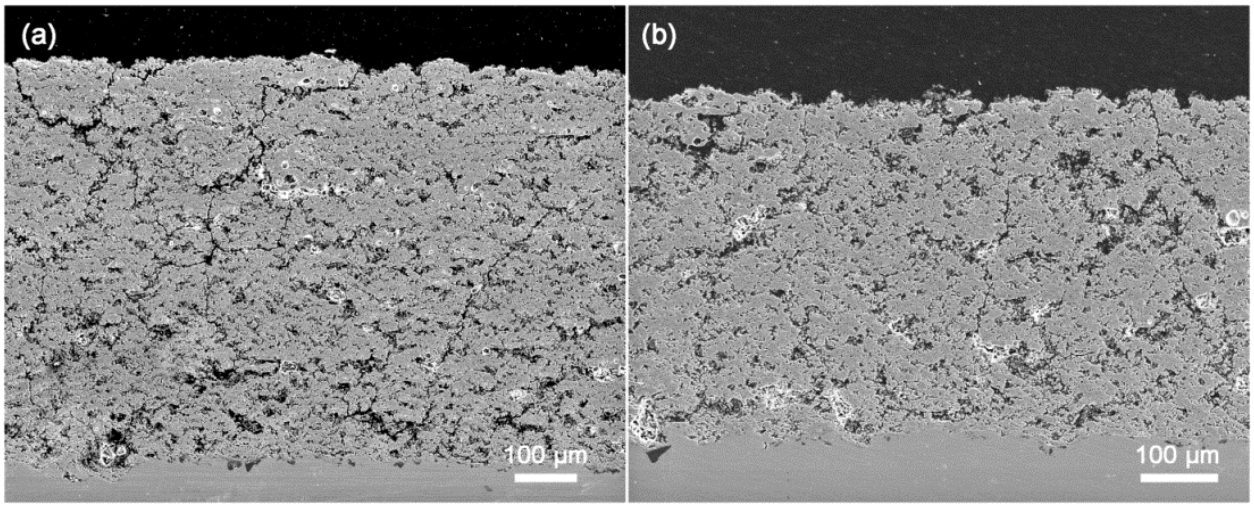

Fig. 5-6 Effect of precursor feed rates on the microstructure of SPPS YSZ + 32.5% Al_2O_3 TBCs: (a) 32 mL/min, and (b) 20 mL/min

5.2.3 Substrate stand-off distance

A closer standoff distance from the plasma gun not only allows the substrate to experience a hotter processing temperature, but also minimizes the chances for molten particles to re-solidify as the downstream temperature of plasma jet cools down rapidly. That's why the microstructure got denser as the standoff distance decreased, as shown in **Fig. 5-7**, until the excessive heat from plasma torch overheated the deposited surface causing spallation.

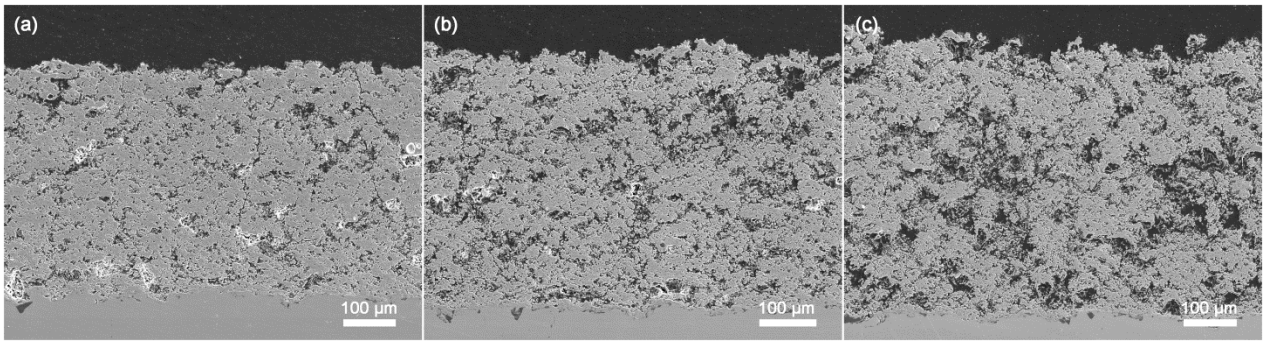

Fig. 5-7 Effect of substrate standoff distances on the microstructure of SPPS YSZ + 32.5% Al_2O_3 TBCs: (a) 1.625 in., (b) 1.75 in., and (c) 1.875 in.

5.2.4 Atomizing pressure

Besides causing the thermal characteristics to become predominantly endothermic (**Table 5-1**), in the case of SPPS YSZ + 50% Al_2O_3 TBCs the high aluminum nitrate content in the precursors could also lead to violent outgassing during decomposition/pyrolysis stages. The release of nitrous gases disturbed the particle breakup process, generated particles with broader size distributions, and produced a coarse microstructure in the deposited coatings (**Fig. 5-8a**). By reducing the atomizing air pressure, the extent of the particle break-up was then mitigated, and consequently the larger and more uniform particles succeeded in producing a more uniform microstructure (**Fig. 5-8b**). Little effect on the coating densification was observed, though.

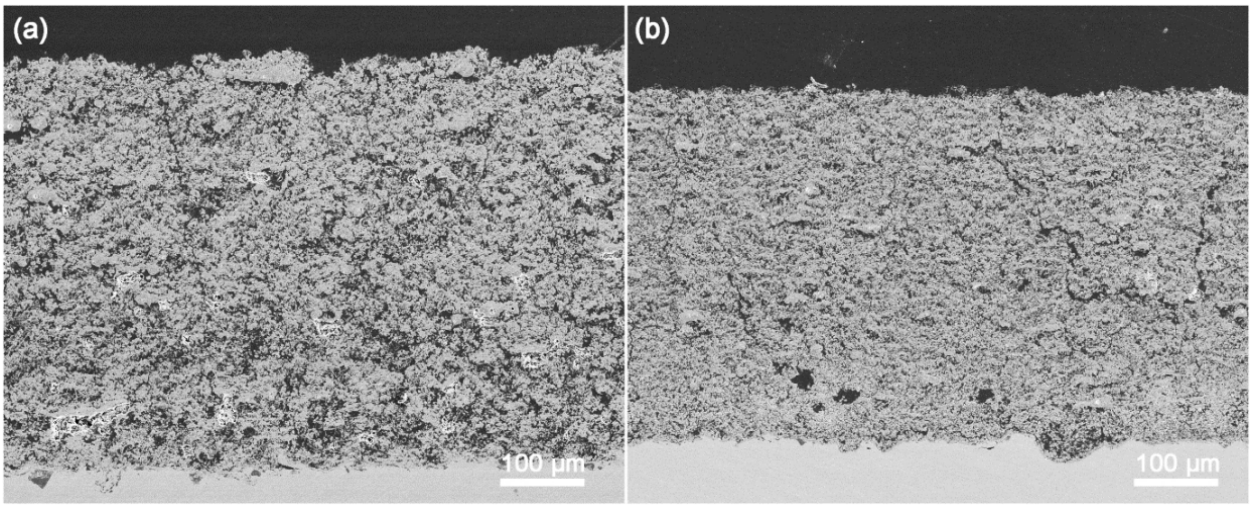

Fig. 5-8 Effect of atomizing air pressures on the microstructural of SPPS YSZ + 50% Al_2O_3 TBCs: (a) 20 psi and (b) 10 psi.

5.3 Deposition of Al_2O_3/TiO_2-doped SPPS YSZ TBC

The discussion of deposition is divided into two separate sections, based on which precursor solvent was used.

5.3.1 Using alcohol-based precursor solution

Other initial considerations for using ethyl alcohol, besides its compatibility with titanium isopropoxide, were the low heat of vaporization (841 kJ/kg in comparison to 2260 kJ/kg of water), and the fact that the organic solvent could burn. The low heat of vaporization in precursor solvent guaranteed a less energy extraction from the plasma jet, and the potential ability for combustion was supposed to introduce more energy, which overall enhanced the energetics in the plasma jet. However, as it turned out, there were more complicated effects associated with the usage of alcohol.

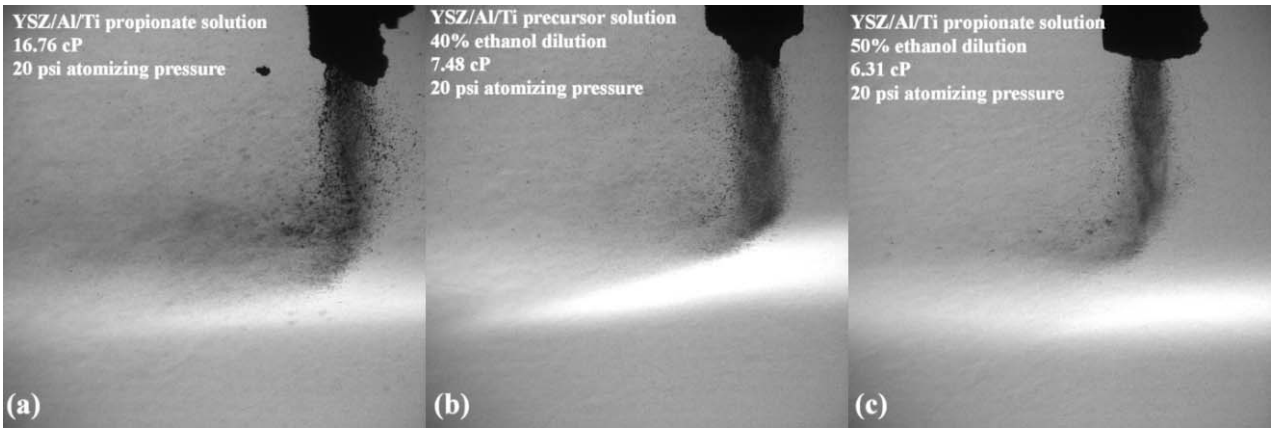

Fig. 5-9 Effect of dilution on precursor delivery at the atomizing nozzle tip

First of all was the clogging and detritus-accumulation at the atomizing nozzle tip that led to inconsistent flow. This could be attributed to the low heat of vaporization in ethyl alcohol, since the solvent dried out so quickly that some dried gels form long before they reached plasma jet. Due to the loss of their mass in solvent evaporation and thermophoresis forces, these gel particulates were transported back to the atomizing nozzle tip, and started to accumulate. As demonstrated in **Fig. 5-9a**, pieces from the loosely compacted built-up could break off from time to time, and disturb the particle deposition process. More severe problems associated with the particle accumulation were the inconsistent flow and wider distribution in droplet sizes. To eliminate this undesirable issue, dilution of the precursor solution was performed, and as shown in **Table 5-3**, this brought remarkable changes in precursor fluid properties, reduction in viscosity in particular.

Table 5-3 Effect of dilution on fluid properties of alcohol-based precursors

Dilution (v/v% ethyl alcohol)	Density ($g \cdot cm^{-3}$)	Dynamic viscosity (cP)
0%	1.091	16.76
5%	1.071	14.96
10%	1.062	13.49
20%	1.028	10.36
40%	1.005	7.48

50%	0.981	6.31

A reduction of precursor viscosity to a favorable range is generally beneficial to the SPPS process. In **Fig. 5-9**, the accumulation at the nozzle tip was obviously mitigated, and also the droplet sizes became finer and more uniform as the degree of dilution increased. The entrainment of atomized fogs into the plasma jet then became an issue, as too fine particles had insufficient momenta to overcome the transverse high-velocity jet to penetrate to the plasma core. Besides, the smaller Stokes number could also lead to certain degree of shadowing effect as the fine particles tend to follow the plasma gas flow instead of directly impacting the substrate, resulting in a columnar structure.

Moreover, diluting the precursor solution also meant lowering the solute-loading in the precursor solution, which in return can adversely affect the deposition rate of the process as well as the microstructures in as-sprayed coatings (**Fig. 5-10**), a similar trend seen in an earlier work performed by Chen et al [95].

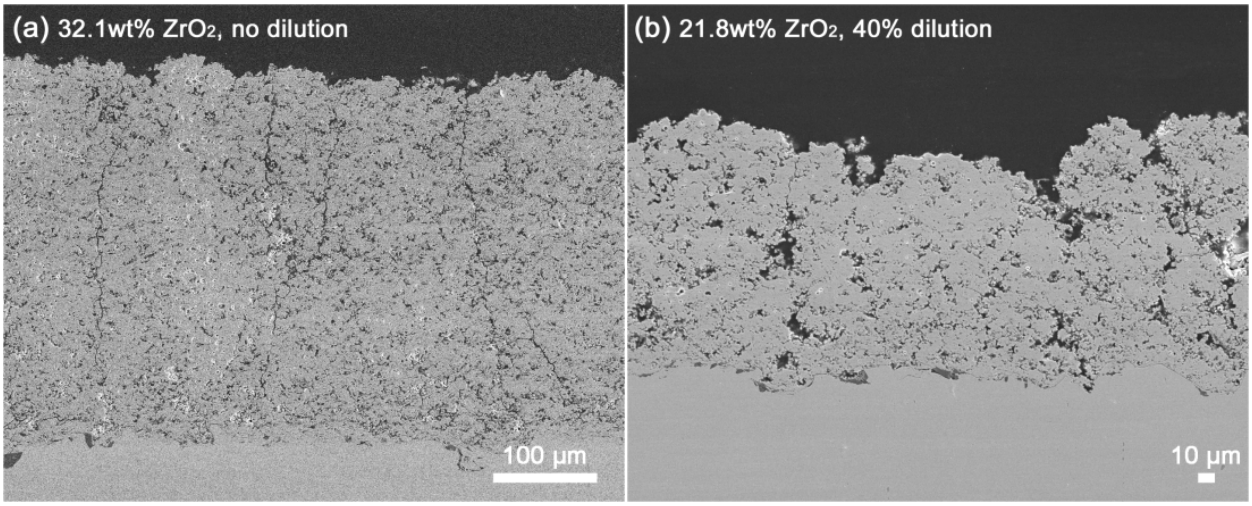

Fig. 5-10 Effect of dilution on as-sprayed microstructure using the alcohol-based precursor: (a) no dilution and (b) 40% dilution.

After diluting of alcohol-based precursor solution, efforts were spent on reproducing the IPB feature in the doped SPPS YSZ TBCs. Similar process parameters were included in the study as the optimization of IPBs, such as raster scan steps, feed rates, standoff distance and the gun power. Reducing the raster scan step size from 3mm to 1mm did reproduce the layered IPB microstructure as long as overheating didn't lead to TBC spallation, but the density of as-sprayed coatings were high. Increasing the standoff distances was found to effectively increase the TBC porosity, but the layering feature became less distinct. Even though a further standoff distance produced a sample with the thermal conductivity of ~0.85 $W \cdot m^{-1}K^{-1}$, the reduction in thermal conductivity was most likely to be the result of the high porosity rather than the porosity layering.

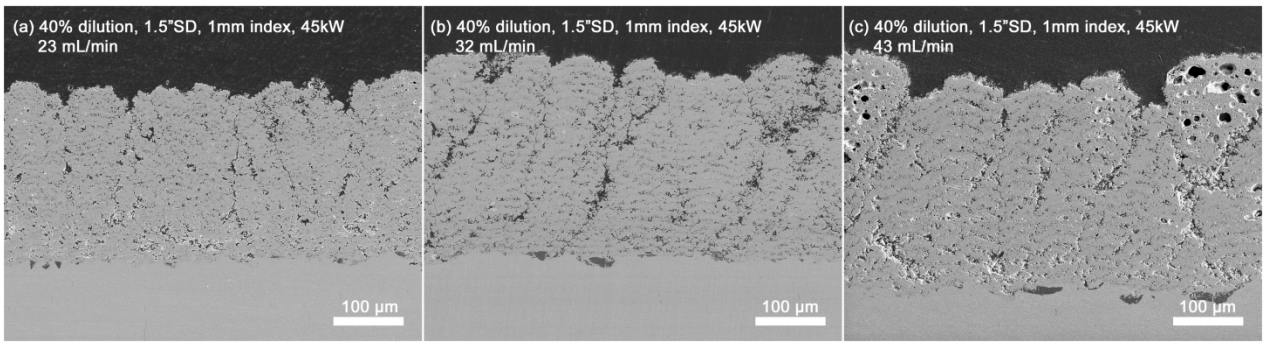

Fig. 5-11 Effect of the feed rate on IPB features using the alcohol-based precursor: (a) 23 mL/min, (b) 32 mL/min, and (3) 43 mL/min.

The effect of feed rates on IPB features, however, was less significant in Al_2O_3/TiO_2-doped SPPS YSZ TBCs using the alcohol-based precursor for enhancing the prominence of layered porosity (**Fig. 5-11**). The relatively dense microstructure in as-sprayed coating using the alcohol-base precursor solution can be explained by the combustion of ethyl alcohol not during the particle pyrolysis though, but in the plasma jet downstream and close to the deposited coatings, which led to additional in-process sintering. Recall that this is reducing plasma composed primarily of hydrogen and argon until sufficient air entrapment occurs downstream. As an

alternative approach to reduced density, the possibility of lowering the plasma gun power was explored and found viable, but again at the cost of losing layered-ordering.

5.3.2 Using water-based precursor solution

Aqueous Al_2O_3/TiO_2-doped YSZ precursor solutions prepared from titanium sulfate and aluminum sulfate/nitrate were employed, after the insensitivity of alcohol-based precursors to processing conditions was realized for reproducing the IPB feature. Since zirconium acetate solution was still the primary component of aqueous precursors, similar to the YSZ precursor, optimal spray conditions of producing SPPS YSZ TBCs with IPBs were utilized as a guideline. Further modifications mostly involved adjusting the precursor feed rates, as the microstructures respond much more effectively with water-based precursor than the alcohol-based ones. As demonstrated in **Fig. 5-12**, as more liquid feedstock was injected into the plasma just, more porous TBCs were produced accordingly; at the same time, the IPB feature became more prominent due to the nature of the raster scan pattern.

The challenge though was that feed rate was still dominated by solution viscosity, and 40 mL/min seemed to be the maximum feed rate for our current delivery system. In order to achieve a higher feed rate, as in the case of **Fig. 5-12b3**, the solution was again diluted, and together with other related factors (e.g. solute loading and solvent evaporation) rendered a microstructure with less uniform porosity.

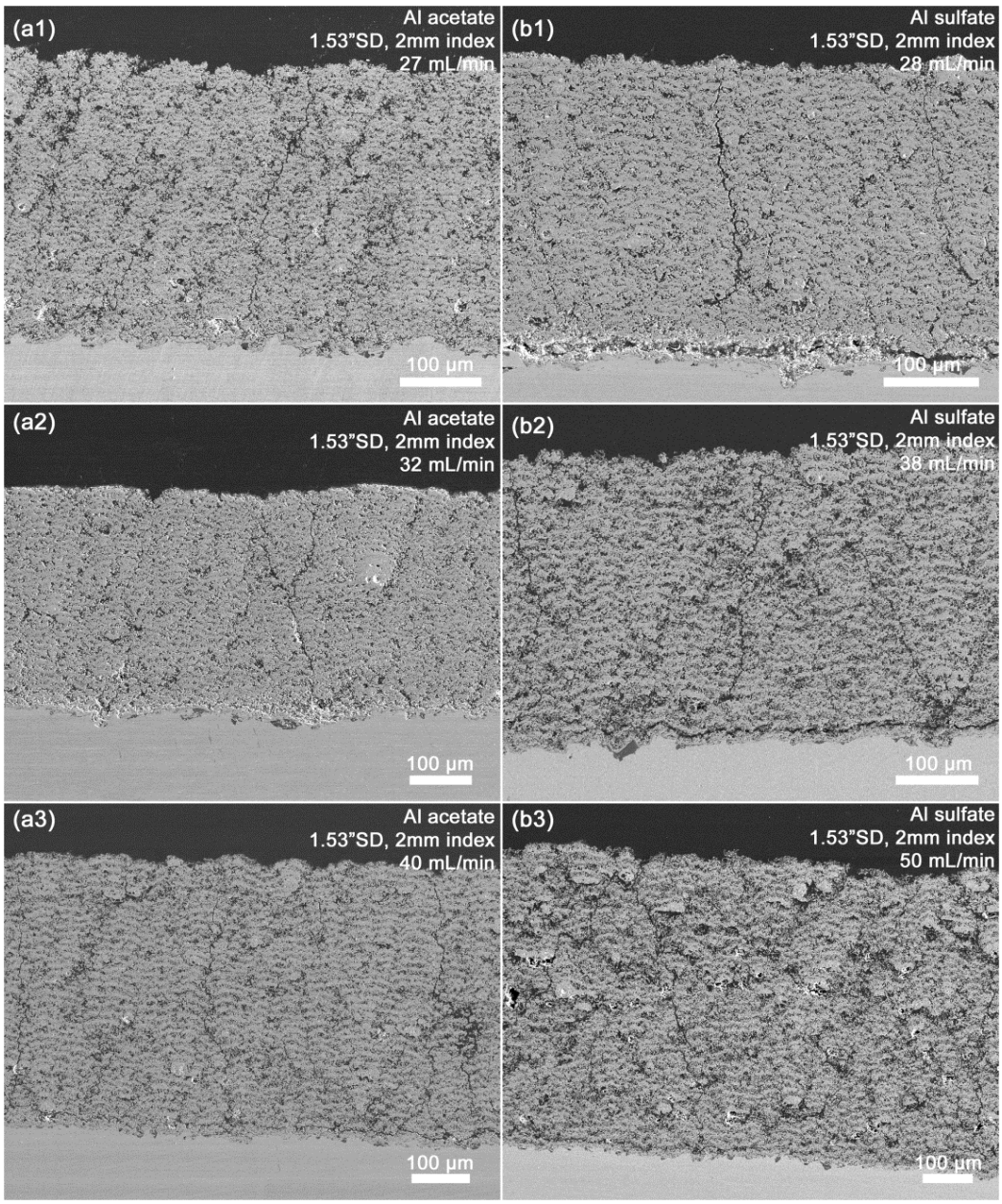

Fig. 5-12 Effect of the feed rate on IPB features using the aqueous precursors

Another trend in **Fig. 5-12** is that precursors made with aluminum acetate generally yield denser microstructures than those made with aluminum sulfate. This is in accordance with the more exothermic behavior observed in the Zr[A]+Y[A]+Al[A]+Ti[S] precursor (**Fig. 5-3)**.

5.3.3 Discussion

Since the plasma primary/secondary gas combination used in this research was the reducing Ar/H_2, the combustion of ethyl alcohol was not likely to occur in the earlier stages of decomposition or provide any beneficial addition of energy; instead, the solvent steam would mix with air in the plasma downstream and generate undesirable heat to the substrates, as evidenced by the measured substrate temperatures in the spray process (**Fig. 5-13**). The approximately 250^{o}C increase in substrate temperature not only produced dense coatings, but could also lead to some other unfavorable microstructural defects.

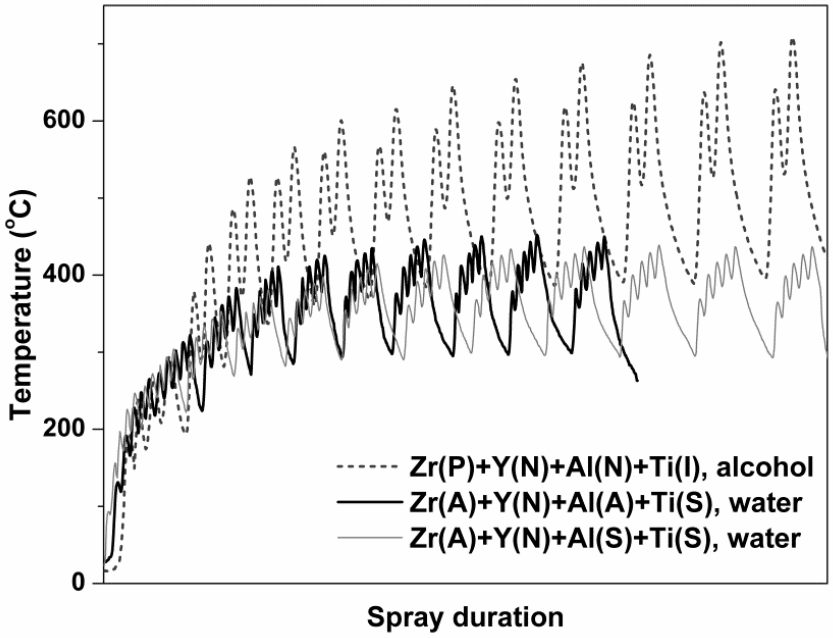

Fig. 5-13 In-process substrate temperatures measured by infrared pyrometer (A: acetate, P: propionate, N: nitrate, S: sulfate, and I: isopropoxide)

One of the microstructural defects was the hollow structures (**Fig. 5-14a**) occasionally observed in the upper regions of the coating. Under the high-magnification SEM characterization, these hollow features were observed to be composed of numerous spherical grains, rather than the typical homogenous molten splats in regular SPPS TBCs. Among all the alloy microstructures in

the Al_2O_3-ZrO_2-Y_2O_3 system reported by Lakiza et al. [149], a specific one with a composition of 80mol% ZrO_2 - 20mol% YA most resembled the microstructure discovered in this study (**Fig. 5-14c**). To be noted was that the 80mol% ZrO_2 - 20mol% YA composition was close to the nominal composition of the doped YSZ TBCs. Besides, the fact that all defects were present close to the top surface implied that their formation was related to the increasing processing temperature. In **Fig. 5-11**, it was also evident that a number of defects formed as the feed rate of the alcohol-based precursors was increased. Providing the excessive heat from the combustion of alcohol kept surrounding the substrate, temperatures of deposited materials increased rapidly as the deposition progressed, and it was possible that after certain point the hot substrate would no longer provide a sufficiently *cool* surface to quench the incoming molten particles forming homogenous splats, but instead promoted phase transformation and crystallization to occur.

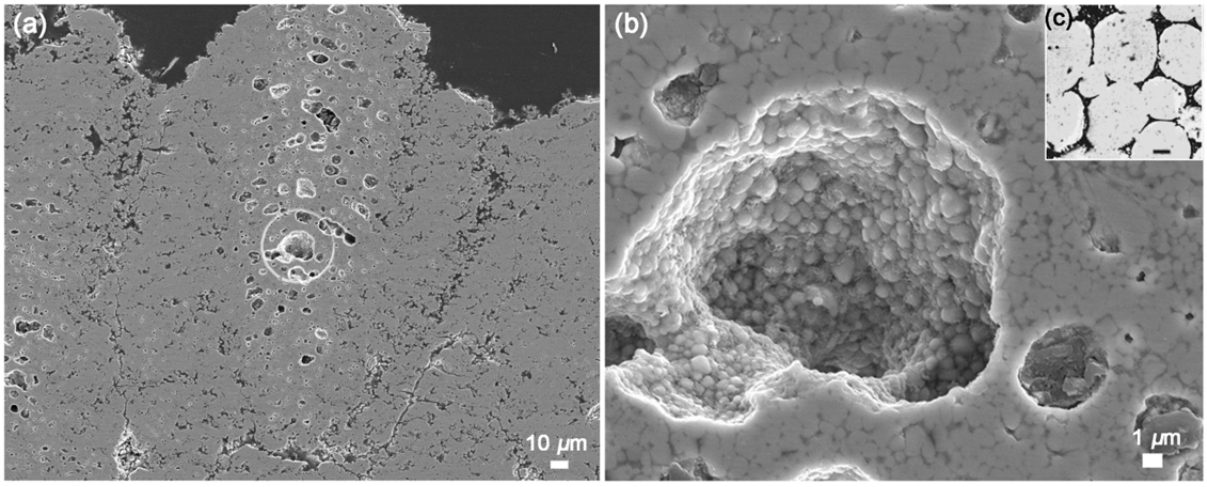

Fig. 5-14 (a) Microstructural defects (circled) observed in the Al_2O_3/TiO_2-doped YSZ coatings; (b) the close-up of the hollow defects embedded in a spheroidal microstructure; and (c) the microstructure of the alloy of the polythermal 80mol% ZrO_2-YA section [149].

Considering the problematic nature of alcohol-based precursors, aqueous precursor solutions are considered to be more suitable for the deposition of homogenous Al_2O_3/TiO_2-doped SPPS YSZ TBCs. As for finding a balance between erosion resistance and prominence of layered porosity,

the microstructure of **a3** in **Fig. 5-12** exhibits a great promise. Therefore, corresponding spray parameters are recorded as the optimal conditions and will be executed for the preparation of the doped SPPS YSZ TBCs.

5.4 Phase determination of as-sprayed TBCs

5.4.1 On Al_2O_3-doped SPPS YSZ TBCs

All as-sprayed Al_2O_3-doped SPPS YSZ TBCs were characterized with XRD for phase determination. Similar to the results shown in [145], 20mol% Al_2O_3 seemed to the upper limit of dopant contents for the deposition of a solid solution using the SPPS process (**Fig. 5-15**), with the increasing Al_2O_3 contents giving more distinct α-Al_2O_3 peaks in the diffraction patterns. An anomaly to this trend occurred in the case of 32.5mol% Al_2O_3, in which significantly weaker Al_2O_3 peaks were observed despite of the higher Al content, as if the formation of crystalline Al_2O_3 was suppressed in the deposition. An explanation for this phenomenon could be the addition of PVA in the original precursor solution, which as suggested in [148] other similar chelating agents can affect the decomposition characteristics of the precursors resulting in a more homogenous mixture. Besides, the exothermic reaction from the decomposition of the mixture of PVA and oxidizers could benefit the atomic mixing during the pyrolysis process, contrary to the excess heat applied to the plasma downstream, which promoted the undesirable accelerated crystallization and grain growth (**Fig. 5-14**).

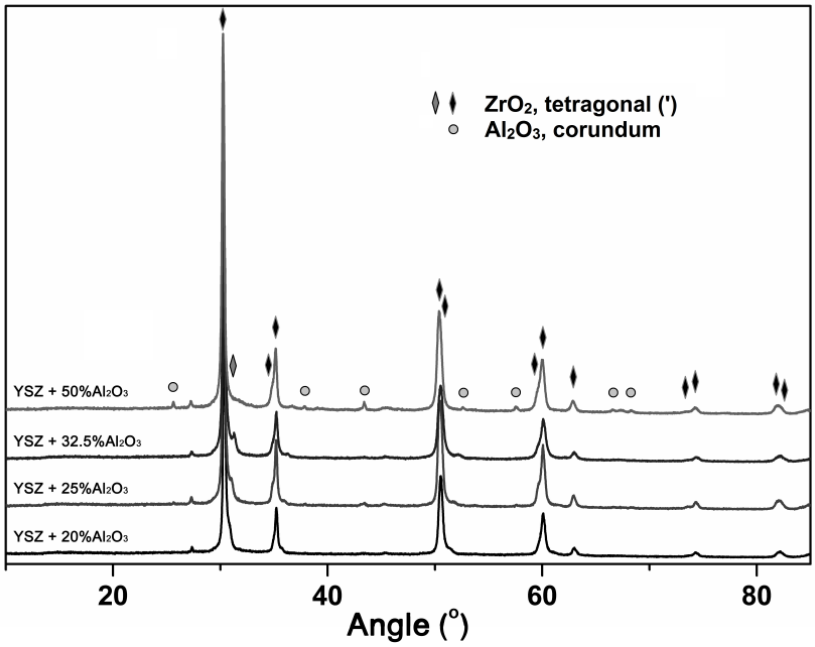

Fig. 5-15 XRD patterns of Al_2O_3-doped SPPS YSZ TBCs at varying dopant levels

5.4.2 On Al_2O_3/TiO_2-doped SPPS YSZ TBCs

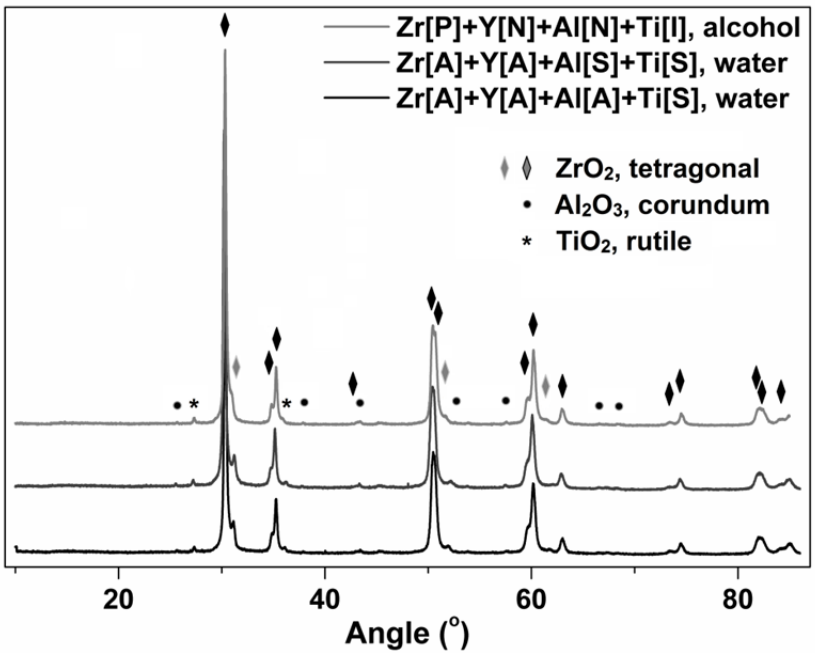

Fig. 5-16 XRD patter of as-sprayed Al_2O_3/TiO_2-doped SPPS YSZ TBCs

Unlike the YSZ+20mol% Al_2O_3+5mol% TiO_2 APS TBCs that exhibited only three *t*-ZrO_2 phases with different tetragonalities in XRD patterns [54, 150], the as-sprayed SPPS TBCs in this study, regardless of the precursor chemistry, also showed traceable amounts of α-Al_2O_3 and rutile TiO_2 (**Fig. 5-16**). Since the nominal coating compositions were the same in both cases, this difference in XRD results may be attributed to either the instrument insensitivity or the in-process volatilization of Al_2O_3/TiO_2 in the original publication.

Chapter 6. Further Modifications for Enhanced CMAS Resistance

6.1 Infiltration of calcium sulfate

$CaSO_4$ filling of the TBC porosity as a mitigation strategy for CMAS attacks was first suggested by Braue [118]. Though the natural occurrence of $CaSO_4$ in TBC systems was reported to be mostly through gas-phase transfer [151], several alternative approaches were explored and studied to achieve complete $CaSO_4$ infiltration in TBC porosity. A vacuum impregnation method was adopted in some cases to assist the delivery of liquid $CaSO_4$ precursors to cracks and pores, as proposed in [152].

6.1.1 Using $CaSO_4$ containing suspensions or slurries

The solubility limit of $CaSO_4$ in water is considerably low, about 0.24 g dihydrate in 100 mL water at 20^{o}C. So to acquire a liquid-form precursor with a practical concentration, preparing suspensions or slurries out of $CaSO_4$ micron-/nano-sized powders are one of the few practical options. In one attempt, $CaSO_4 \cdot 2H_2O$ was calcined at 150^{o}C to form the gypsum plaster, and then re-introduced to water under drastic agitation, rendering an un-set suspension. Another approach was to mix $CaSO_4$ powders in an epoxy resin with a moderate viscosity, followed by an extensive ball-milling. Vacuum impregnation was utilized in both cases to assist the infiltration of $CaSO_4$-containing suspensions/slurries, yet the subsequent SEM/EDS characterization indicated the material were resting on top of the coating instead of going in. The proposed explanation for this failure is that the suspended particles or agglomerates are too large for the openings of vertical cracks in SPPS TBCs, which are typically around 5 microns in diameters.

6.1.2 Using eutectic mixtures of sulfates

The high melting point of anhydrous $CaSO_4$ powders, 1460°C, prevents the direct infiltration of $CaSO_4$ through the melting route. However, by alloying $CaSO_4$ with other materials to form eutectic mixtures, the melting temperature can be significantly decreased. One example is the eutectic mixture of $CaSO_4$ and CaO has a melting point of 1365°C, lower than pure $CaSO_4$ [153].

In this study the possibilities of utilizing eutectic mixtures of $CaSO_4$ and other sulfates, such as Na_2SO_4 and $MgSO_4$, were explored. According to the phase diagrams of the binary $CaSO_4$-Na_2SO_4 and the ternary $CaSO_4$-Na_2SO_4-$MgSO_4$ systems (**Fig. 6-1)**, the compositions of 50mol% Na_2SO_4+50mol% $CaSO_4$ and 50mol% Na_2SO_4+30mol% $MgSO_4$+20mol% $CaSO_4$ were selected, each having a melting point of ~900°C and 750~800°C, respectively. To acquire homogenous mixtures of sulfates, the sulfate powders were typically mixed with zirconia balls in a dispersing medium of ethyl alcohol and left ball-milling for about 48 hours, after which the alcohol was evaporated and sulfate mixtures were dried overnight in a Binder oven at 150°C.

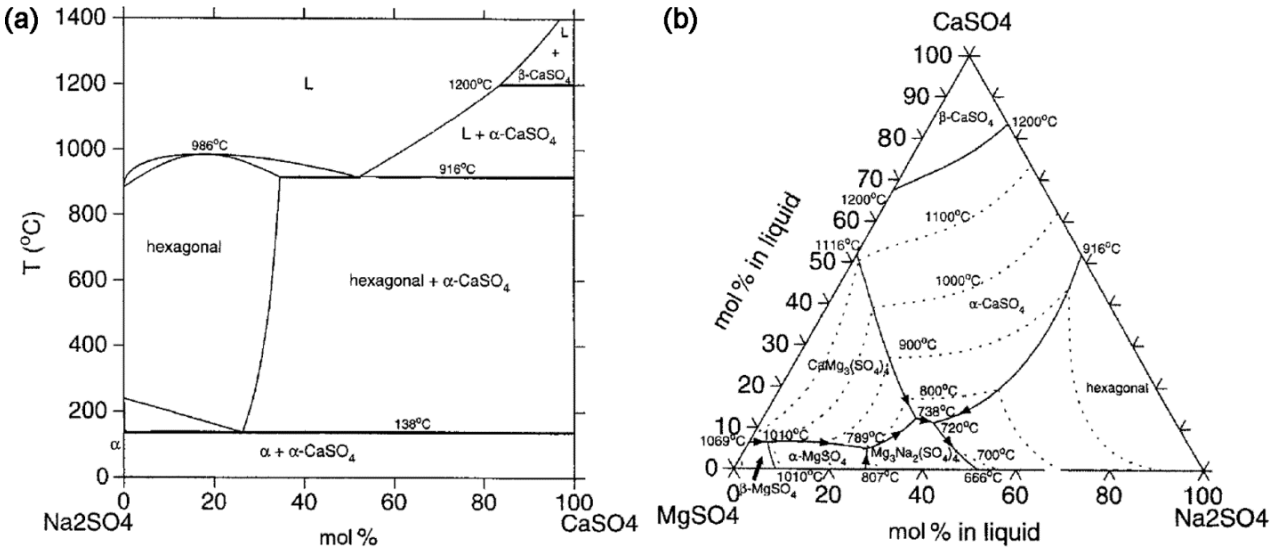

Fig. 6-1 Calculated phase diagrams of (1) the binary $CaSO_4$-Na_2SO_4 and (2) the ternary $CaSO_4$-Na_2SO_4-$MgSO_4$ systems [154]

The SPPS YSZ TBCs were then spread with the sulfate eutectic mixtures, before heat-treating in a muffle furnace at 1000^{o}C for 1 hour.

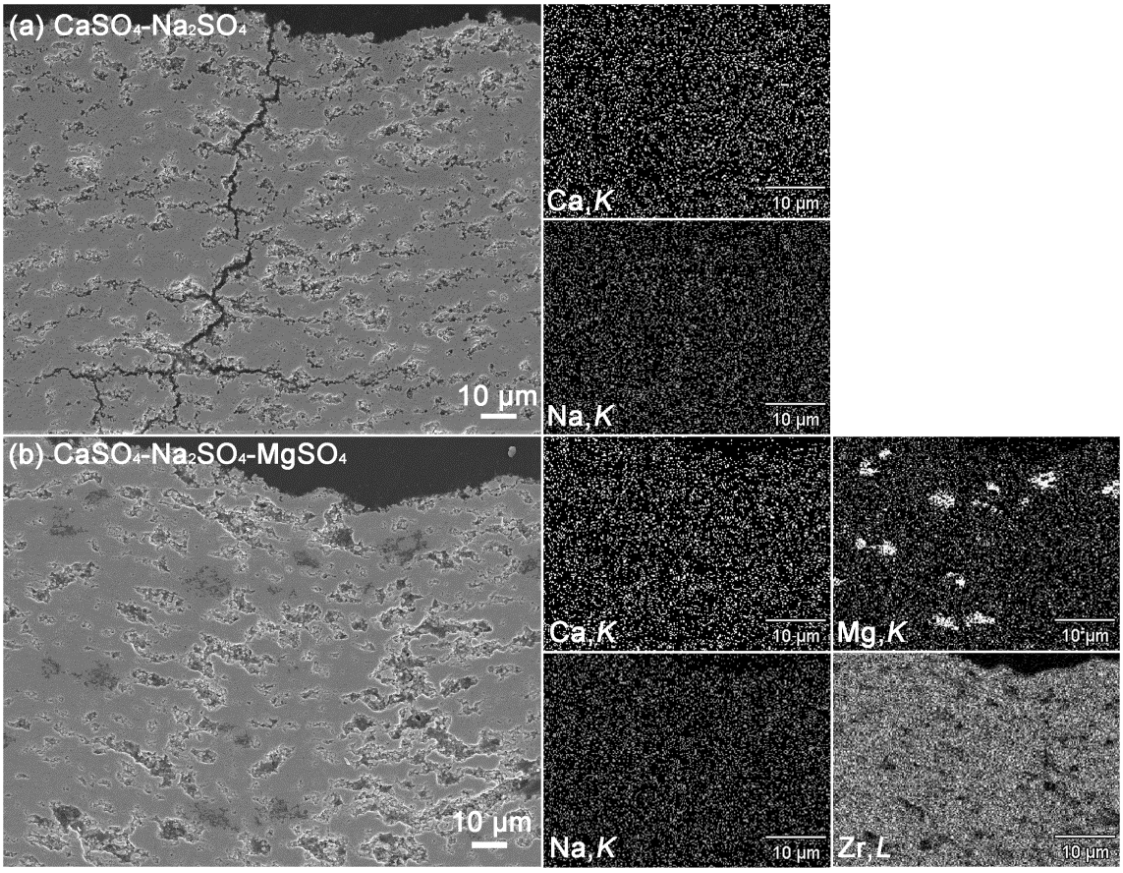

Fig. 6-2 Infiltration of $CaSO_4$ through eutectic molten mixtures of (1) 50mol% Na_2SO_4+50mol% $CaSO_4$ and (2) 50mol% Na_2SO_4+30mol% $MgSO_4$+20mol% $CaSO_4$

According to the SEM/EDS mapping, the molten eutectic sulfate mixtures did penetrate the TBC at relatively lower temperatures and some porosity were completely sealed, especially in the case of Na_2SO_4-$MgSO_4$-$CaSO_4$ (**Fig. 6-2**). But then the removal of alloying materials became an essential yet challenging issue, as failing to do so could lead to complications in terms of interactions with CMAS.

6.1.3 Using chemical reactions

Since the solubility of calcium sulfate is the biggest obstacle in obtaining liquid precursors, an alternative approach is to use soluble salts, calcium chloride and ammonium sulfate in this case, as starting materials to form $CaSO_4$ in its designated positions through the following the chemical reaction:

$$CaCl_2 + (NH_4)_2SO_4 \xrightarrow{\Delta} CaSO_4 + 2NH_3\uparrow + 2HCl\uparrow$$

Saturated calcium chloride solutions was infiltrated into TBC topcoats through vacuum impregnation, and dried in a low temperature oven. Then excess saturated ammonium sulfate solution was applied, before the TBCs were calcined in a muffle furnace to release any gases. Unfortunately, the chemical reaction was later observed to occur primarily on the TBC surface, as $CaCl_2$, instead of $CaSO_4$, was still observed in the cross-sectional SEM/EDS characterization. This was probably caused by the instantaneous blocking of the open pores by the $CaSO_4$ produced from the chemical reaction, preventing ammonium sulfate solution penetrating to form the calcium sulfate inside the coating.

6.1.4 Using the aqueous calcium sulfate solution with chelating agents

As stated earlier, calcium sulfate is known to be hardly any soluble, but with the help of chelating agents, e.g. EDTA, Ca^{2+} can be stabilized and co-exist with SO_4^{2-} in the solution form. An aqueous calcium sulfate precursor was then prepared with an approximately 8wt% $CaSO_4$ content, and the calcined precursor residues have shown clear anhydrite peaks by XRD (**Fig. 6-3**).

The following SEM/EDS confirmed the existence of calcium sulfate in the SPPS TBCs after the vacuum impregnation and calcination, yet the signal was weak, which was the result of the dilute concentration. This issue can be resolved by repeated infiltration/calcination cycles.

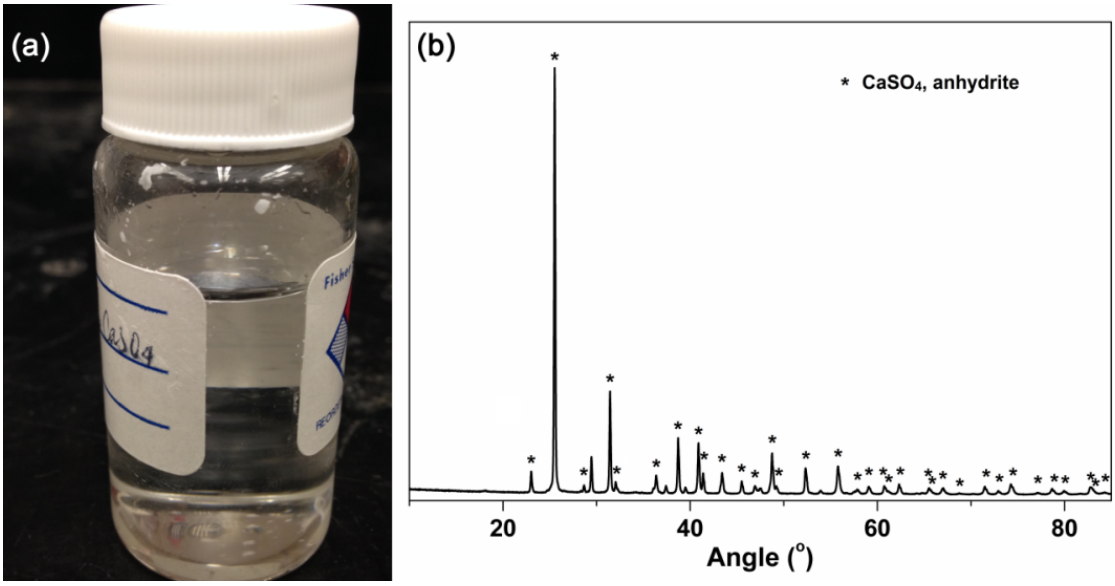

Fig. 6-3 (a) Aqueous calcium sulfate precursor solution and (b) the XRD identification of the furnace-pyrolysis residue

6.1.5 Discussion

According to the results shown above, few approaches succeeded in delivering $CaSO_4$ into the TBC cracks and pores that can provide additional protection against CMAS attacks. The aqueous calcium sulfate precursor may yield complete sealing of the cracks, but it involves tedious lab effort and lacks practical significance. By far, the gas-phase transfer has still been the only feasible method to deposit $CaSO_4$. However, limited by the equipment availability, performing such gas phase transfer was not pursued in the scope of this research, but instead the possibility of applying alternative blocking materials other than $CaSO_4$ were thereby explored.

6.2 Infiltration of yttrium oxide

Inspired by the CMAS-inhibition mechanism of GZO, dissolution of rare-earth zirconates upon contact with CMAS and the formation of a highly-stable apatite silicate of $Ca_2RE_8(SiO_4)_6O_2$, we then proposed to infiltrate the cracks of SPPS TBCs with penetration-blocking materials, so as to further enhance the CMAS resistance. Y_2O_3, known for its reactivity with CMAS and the ability to form high-temperature apatite silicate, was then selected as the candidate blocking materials to substitute for $CaSO_4$. One attempt for Y_2O_3 infiltration was performed by vacuum impregnation with Y_2O_3 nanopowder suspensions. Even though the nominal particle size is remarkably smaller than the crack opening (2-5μm), Y_2O_3 was still prevented from delivered into the coating cracks due to particle agglomeration, and instead formed a dense layer of nanopowders on top of TBCs (**Fig. 6-4**).

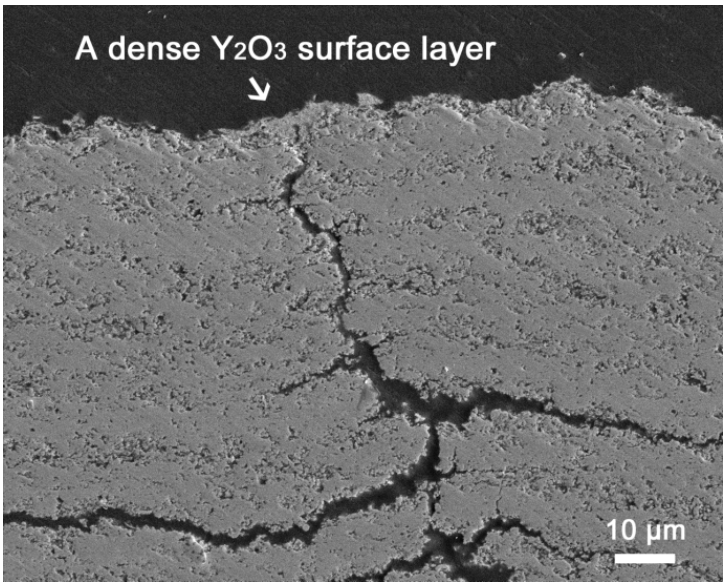

Fig. 6-4 Vacuum impregnation with a Y_2O_3 nanopowder suspension leads to a dense surface layer instead of infiltration

Another approach explored to deliver Y_2O_3 into the coating cracks was to infiltrate a salt-based precursor solution and to form the oxide through subsequent furnace pyrolysis. A saturated

yttrium nitrate aqueous solution was then prepared and applied to TBC sample under vacuum, after which it was calcined at 600^{o}C for 5 hours. This process was repeated intentionally for three times in order to get full infiltration. The SEM/EDS characterization later confirmed the existence of yttria deep in the coating (**Fig. 6-5b**). In fact, the infiltration is so complete that the IPBs are now hard to distinguish in **Fig. 6-5a**.

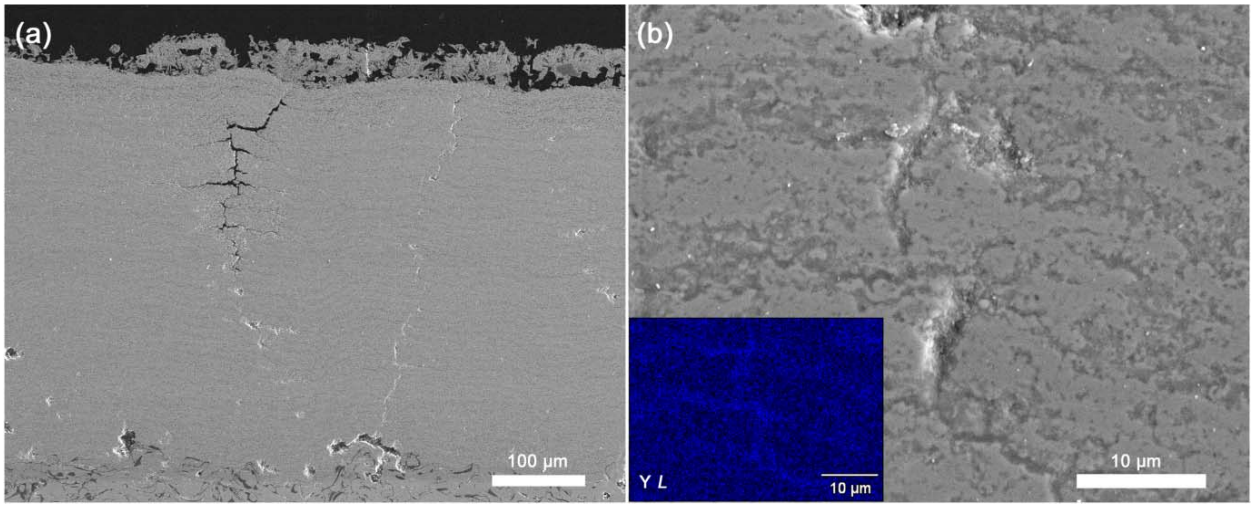

Fig. 6-5 Vacuum impregnation with a saturated yttrium nitrate solution leads to a complete Y_2O_3 infiltration

Chapter 7. Investigation of TBCs' Resistance to CMAS Attack

7.1 Precursor characterization

The CMAS compositions differ remarkably between locations, climates, service environments, and etc. The published data, though, can be roughly categorized into three classes, based on their sources [47]:

(i) Minerals including dust, sand and ash [155, 156, 157, 158, 159, 160],

(ii) Actual engine deposits [155, 156, 134, 151], and

(iii) Simulated CMAS synthesized using oxide mixtures [45, 32, 54, 33, 121, 161].

As demonstrated by Krause et al [43], the optical basicity of all published CMAS compositions fall in a narrow range of 0.49-0.75, and for simulated CMAS specifically, the optical basicity is around 0.64, regardless of the relative concentration of constituents. This has led to the confident selection of the three simulated CMAS compositions (**Table 2-3**), namely the 4-, 7- and 9-component CMAS to be used in the CMAS-TBC interaction tests, and the yielded results are expected to be general to other compositions due to the similar optical basicity values.

The initial melting point was the primary property of interest for all three simulated compositions: Drexler et al. showed the 4-component CMAS to be molten at 1200^{o}C [54]; but little published data is available for the 7- and 9-CMAS. After the DSC-TGA measurements (**Fig. 7-1**), the melting point of 7-CMAS was found to be at 1132^{o}C, while a value of 1180^{o}C was determined for 9-CMAS, even though some ingredients tended to complicate the measurement by displaying various stages of decomposition. 4- and 9-CMAS were both utilized for spritz tests, as they would differentiate the effect of CMAS compositions, if there was any, while the 7-CMAS,

which resembled mostly the 4-CMAS (**Table 2-3**), was selected specifically for the paste tests, as the much lowered melting point would ensure CMAS to attack the TBCs the same way it should in actual engine environments at determined testing temperature of 1180^{o}C. The heat-up duration in furnace cycles was also adjusted from the normal 5 minutes to 10 minutes, to accommodate the drastic testing conditions and avoid any potential furnace damage.

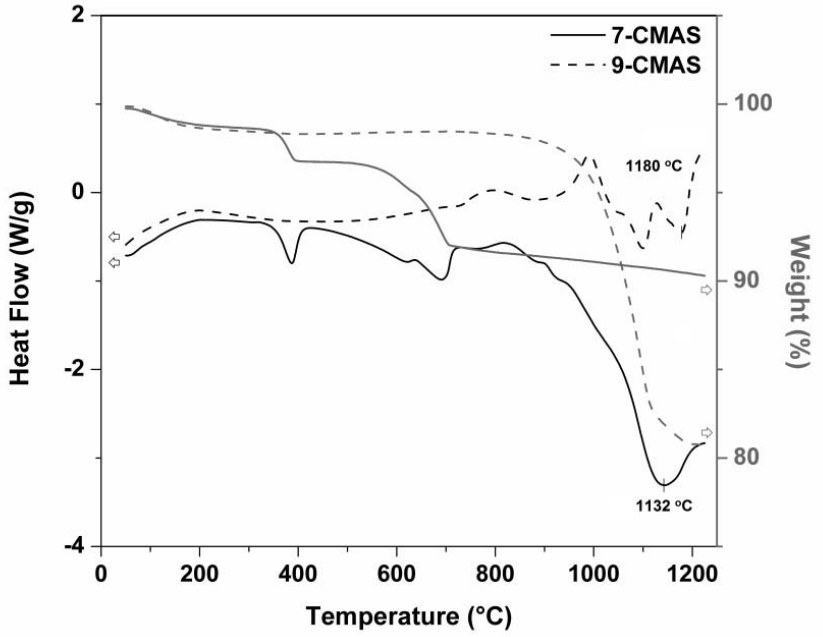

Fig. 7-1 Thermal characteristics of dried 7-/9-CMAS precursor gels

7.2 CMAS-TBC interaction: the spritz test

In the spritz test, cyclic life data was gathered for different TBC systems and used as one of the indicators of CMAS resistance. Due to limited quantities of OEM superalloy substrates, for most cases only one sample was tested for each condition, except for two double-layer TBCs spritzed with the 9-CMAS. Although not statistically rigorous, the one and only replicated test was consistent with there being relatively modest scatter in these tests. Besides, OEM APS YSZ baseline samples, which contains 10~15% porosity, were treated alongside with modified SPPS

TBCs for direct comparison. Based on this limited testing, it is clear in **Fig. 7-2** that periodically spraying the CMAS precursor solution over the coating surfaces did shorten the cyclic lifetime significantly, regardless of the CMAS composition due to the similar optical basicity. But if we look into the group of SPPS YSZ alone, spritzing deionized water (precursor solvent) didn't affect the cyclic life much, as opposed to the case of no CMAS application (51 cycles vs. 55 cycles). This implies that the thermal shock of room-temperature water in contact of hot TBC surfaces was of minimal effect to sample failures and thereby the reduction in TBCs lives under spritz conditions was mostly due to CMAS attack.

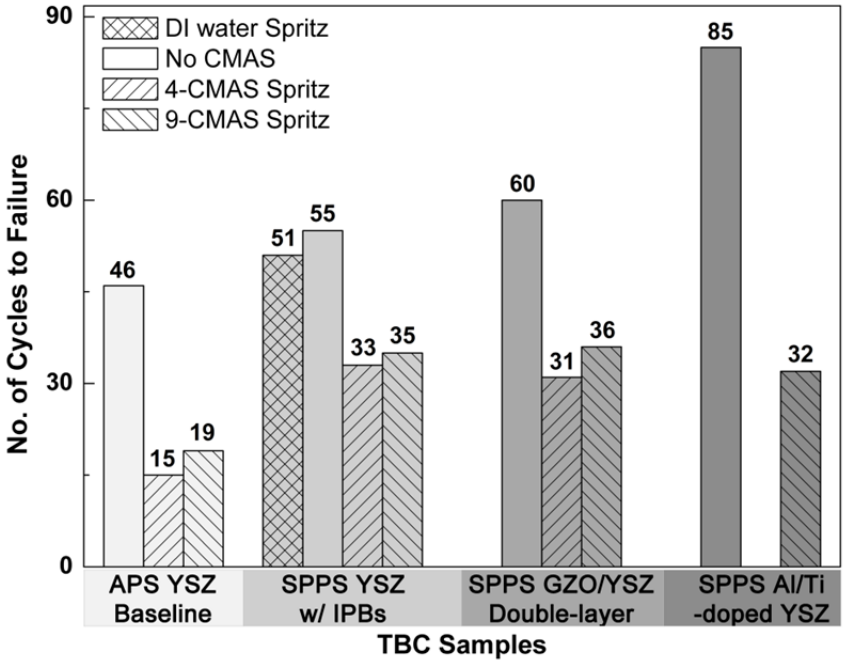

Fig. 7-2 Cyclic lifetime of different TBC systems in the spritz test

The reaction between the CMAS precursor and TBC test samples was also evident by the change in XRD patterns collected before and periodically during the thermal cycling (**Fig. 7-3**). In the case of double-layer SPPS GZO/YSZ TBCs, the sample prior to the thermal cycling exhibited strong fluorite GZO peaks, while the furnace-pyrolyzed 9-CMAS powders demonstrated a

typical anhydrite pattern, due to the high sulfate and calcium concentrations in its composition. The diffraction patterns gathered during the spritz tests resembled neither the two starting materials, nor a simple combination of the two, but showed a series of additional peaks. Some of the additional peaks were identified as different kinds of calcium silicates, which were expected to be the result of the crystallization of the two major constituents in this specific CMAS composition (**Table 2-3**). The very observation of the rare-earth apatite silicate, $Ca_2Gd_8(SiO_4)_6O_2$, indicated the interaction between CMAS and TBC, validating the efficacy of the spritz test. By comparing the relative peak strength among different diffraction patterns during spritz tests, it was also clear that the silicate and fluorite peaks weakened as the tests progressed, while the apatite silicate peaks became more prominent, which suggested that applying the CMAS in a liquid form was capable of replicating and even monitoring the progression of the CMAS-TBC interaction.

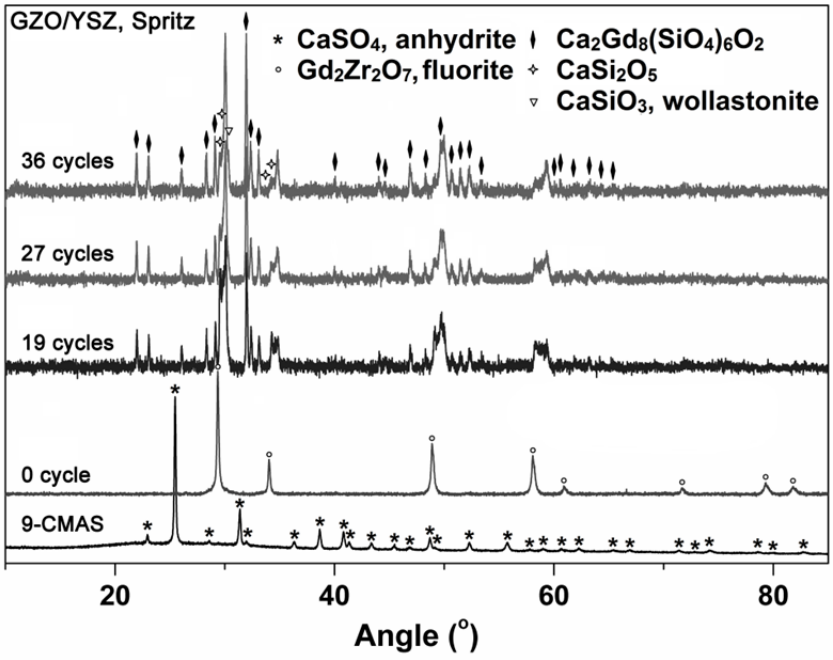

Fig. 7-3 XRD patterns of double-layer GZO/YSZ SPPS TBCs before and during CMAS spritz tests

The characterization of cross-sectional microstructures added another dimension to the CMAS resistance assessment. As summarized in **Fig. 7-10**, in the spritz tests, spallation in all three TBC systems occurred close to the topcoat/TGO interfaces, again similar to the cyclic durability test results. In the case of SPPS YSZ with IPBs, the layered porosity was gradually filled with molten glassy melt (**Fig. 7-10a2**) as it got closer to the coating surface, showing the CMAS attacks.

Secondly, when compared across all TBC groups, **Fig. 7-2** indicates that SPPS TBCs, regardless of microstructure or composition, generally withstood modestly more thermal cycles than APS YSZ baselines did. This result was in accordance with the previously-reported better thermal cyclic durability in SPPS TBCs, indicating the strain-tolerant microstructure improves cyclic lives both with and without CMAS attacks. The stress-relieving vertical cracks could alleviate the damage by the CMAS penetrating into cracks and small pores, as shown in **Fig. 7-10a2**.

Judging from the percentage of the cyclic life reduction by CMAS attacks, Al_2O_3/TiO_2-doped YSZ TBCs had the worst performance among all SPPS TBCs; yet between the other two SPPS TBC systems, the difference was little. In the case of the double-layer SPPS GZO/YSZ TBC, contrary to an earlier study [30], little CMAS resistance improvement was seen in the spritz tests, when the SPPS YSZ TBCs without GZO PSLs was compared. Given the fact that CMAS did attack the TBCs (shown in both XRD and EDS mapping) and shorten the cyclic lives, this contradictory phenomenon was unlikely to be the results of CMAS not doing the damage, but rather due to spritz conditions not being able to reproduce the CMAS infiltration-inhibiting reactions in GZO PSLs.

7.3 CMAS-TBC interaction: the paste test

The paste test, with a one-time application of a much greater amount of CMAS over coating surfaces followed by the same 1180^{o}C one-hour furnace cycles, was therefore employed to complement the assessment of CMAS resistance. The 7-CMAS composition was chosen specifically in this case, since its low melting point would facilitate the CMAS infiltration and prevent the cooling fan from blowing the paste away between cycles. Contrary to the results of spritz tests, the double-layer SPPS GZO/YSZ TBCs this time lasted nearly 6 times longer than the SPPS YSZ TBCs, over 13 times longer than the APS YSZ baseline and 20 times longer than Al_2O_3/TiO_2-doped YSZ TBCs (**Fig. 7-4**). One piece of the SPPS IPB YSZ TBC infiltrated with a potential infiltration-blocking material, Y_2O_3, was also tested alongside with other TBC modifications, and the cyclic life was found shortened after the Y_2O_3 infiltration than before.

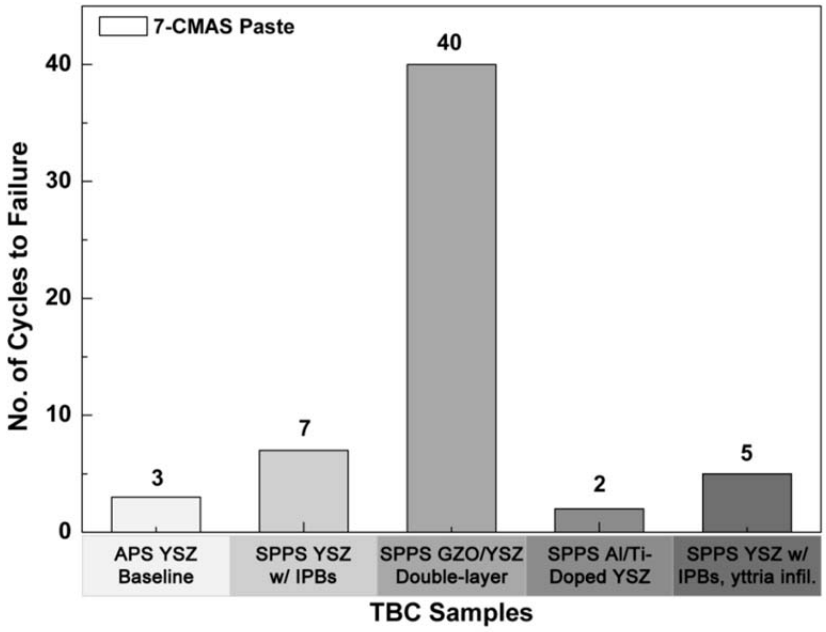

Fig. 7-4 Cyclic lifetime of different TBC systems in the paste test

7.3.1 APS YSZ baseline and SPPS YSZ TBCs with IPBs

In APS YSZ samples, cracks were found to propagate from the topcoat surface to the TGO interface (**Fig. 7-10b1**), rendering a flakey macroscopic appearance, while according to the microstructural characterization, segments above the spallation site were in fact fully infiltrated with CMAS.

In the SPPS YSZ TBCs with IPBs, coatings delamination occurred at the TGO to topcoat interface, right beneath where the coating was fully penetrated by CMAS. The CMAS penetration remarkably reduced the porosity in the coating, causing the ceramic topcoat to lose its strain tolerance and to become more susceptible to stress accumulation at the topcoat to TGO interface, under the cyclic conditions.

7.3.2 Double-layer GZO/YSZ SPPS TBCs

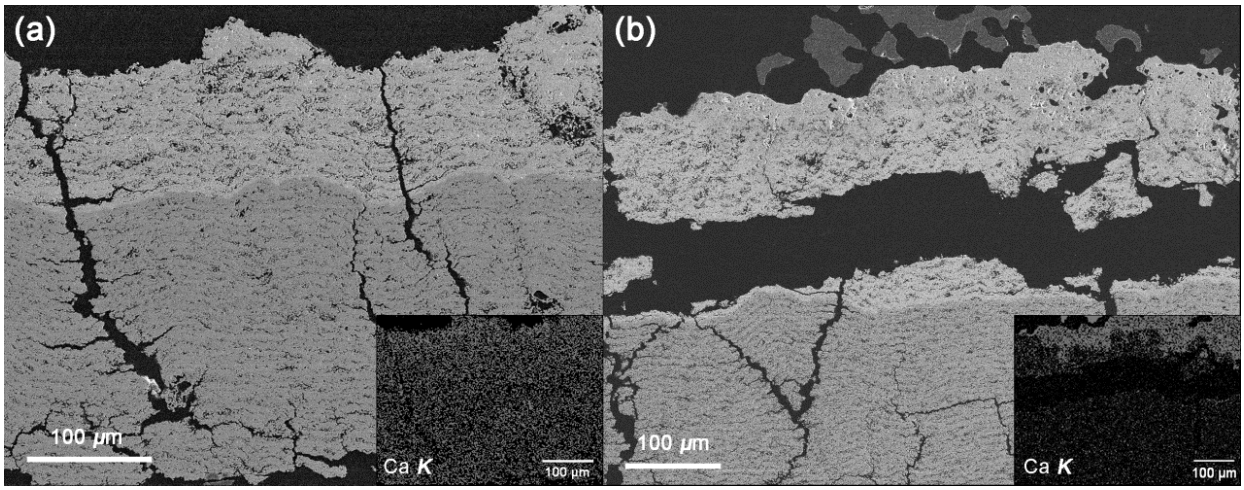

Fig. 7-5 SEM/EDS cross-sectional images of SPPS GZO/YSZ double-layer samples showing (a) CMAS infiltrated through both TBC layers in the spritz test while (b) CMAS trapped in the GZO PSL under paste conditions

Based on the cross-sectional characterization on the failed microstructure, the double-layer GZO/YSZ SPPS TBCs in the paste tests were able to withstand the CMAS attack by trapping a

significant amount of CMAS in its sacrificial surface layer (**Fig. 7-5b**), and allow the underlying YSZ interlayer to still properly function as a thermal barrier.

The XRD characterization during the paste tests again confirmed the formation of the apatite silicate, but at a lower concentration (**Fig. 7-6**). The pattern of the original 7-CMAS composition was characterized as predominantly lime with weak peaks of other constituents on an amorphous background. After the CMAS paste was applied, different kinds of calcium silicates readily crystallize as the paste test progressed, but a relatively less amount of apatite silicate was observed. Judging from the cross-sectional image (**Fig. 7-5b**), it seemed that the formation of apatite silicate occurred more likely inside the coating than on the surface, which by comparing to the result of the spritz tests, appeared to be more effective at inhibiting the penetration of CMAS.

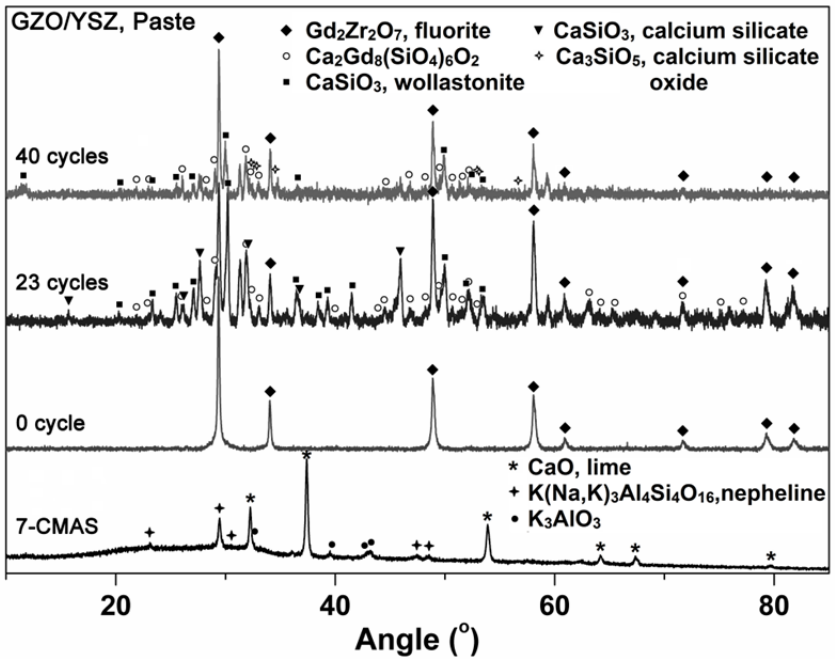

Fig. 7-6 XRD patterns of double-layer GZO/YSZ SPPS TBCs before and during CMAS paste tests

7.3.3 Al_2O_3/TiO_2-doped SPPS YSZ TBCs

According to the results of paste tests, Al_2O_3/TiO_2-doped SPPS YSZ TBCs were indeed reactive to the simulated CMAS paste, as evidenced by the dendrite-like patterns found after the CMAS attack. In fact, the high magnification EDS mapping on these crystalline regions (**Fig. 7-7**) confirmed the detailed patterns were rich in Ca, Al, and Si, presumably forming the anorthite ($CaAl_2Si_2O_8$) phase. This observation agreed with the Raman map results obtained by Senturk et al [150], indicating the Al^{3+} and Ti^{4+} solutes do interact effectively with CMAS. However, the crystalline anorthite wasn't shown in this study to be as effective as the gadolinium zirconate in arresting the CMAS penetration front, and the CMAS-resistance was limited by the *volume* of the *alumina reservoir* present in the TBC topcoat, beyond which the leftover CMAS can still penetrate the TBC microstructure all the way to the topcoat to TGO interface and cause the spallation (**Fig. 7-10b4**).

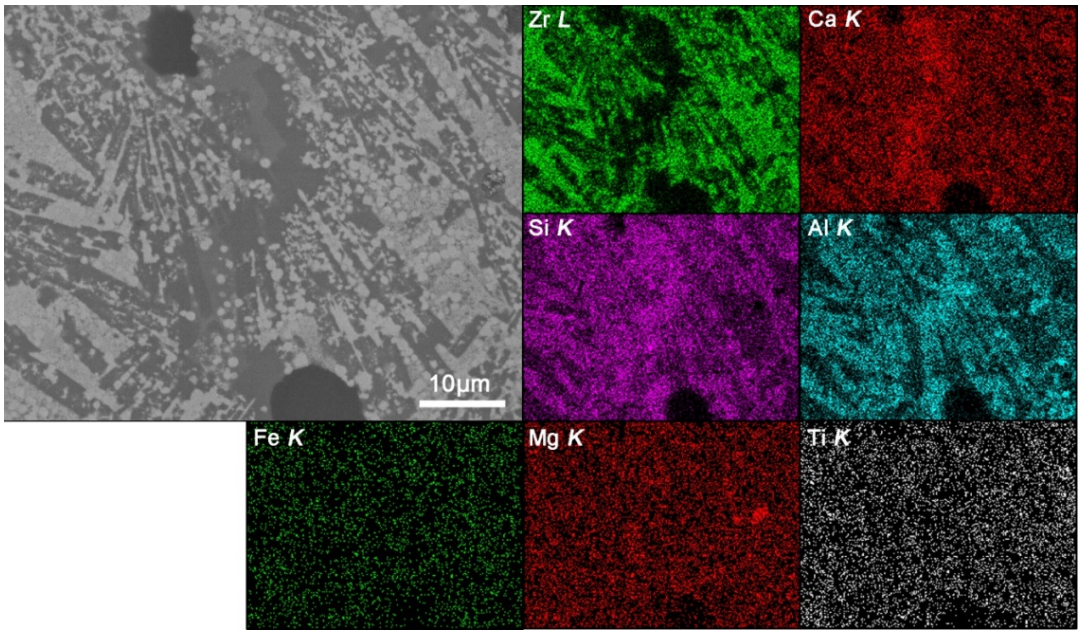

Fig. 7-7 EDS mapping of the secondary patterns found in the Al_2O_3/TiO_2 SPPS YSZ TBCs upon contact with CMAS pastes

7.3.4 Y_2O_3-infiltrated SPPS YSZ TBCs

The infiltration of Y_2O_3 into the cracks of YSZ TBCs was not only verified by the cross-sectional SEM characterization and EDS mapping shown in **Fig. 6-5**, but also indicated by the XRD pattern collected before the paste tests, as distinct cubic Y_2O_3 peaks were observed besides the typical patterns of *t'*-YSZ (**Fig. 7-8b**). In the CMAS paste, the Y_2O_3-infiltrated YSZ appeared to be more reactive than the regular SPPS YSZ TBCs upon contact with CMAS, in the sense that a detailed granular microstructure was formed (**Fig. 7-8a**), which was not present in the regular SPPS YSZ TBCs in contact with CMAS. The corresponding XRD pattern indicated the occurrence of apatite silicate, $Ca_4Y_6(SiO_4)_6O$, as it was originally designed to be. This modification, though formed the apatite silicate and exhibited longer cyclic life than the APS YSZ baselines, still wasn't effective enough to stop CMAS from further penetration. Besides, through careful examination on the change of all zirconia peaks [162], it suggested that there was a significant increase in the amount of the cubic phase after the paste test. This may either be the result of the excess infiltrated Y_2O_3 shifting the *t'* partially-stabilized zirconia to the cubic full-stabilized zirconia, or the CMAS dissolving/re-precipitating YSZ TBC rendering the un-stabilized zirconia. Either way, the presence of a considerable amount of cubic zirconia would be harmful to the mechanical properties, such as fracture toughness, as well as the phase stability.

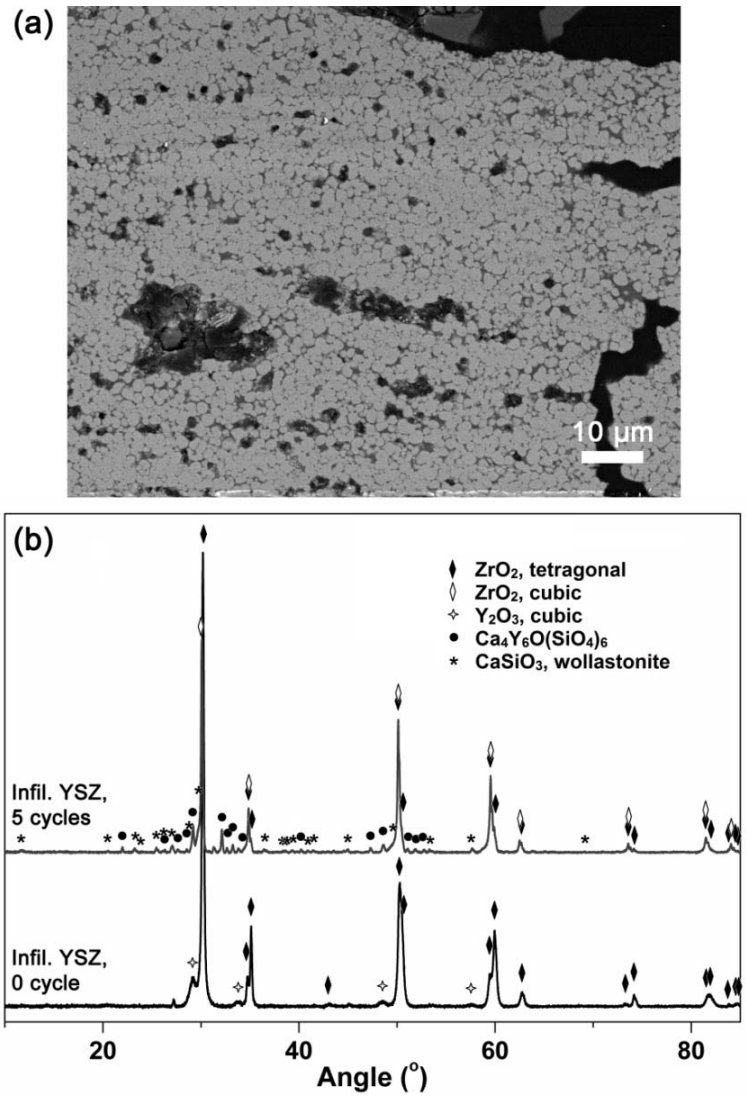

Fig. 7-8 (a) TBC-CMAS interactions in Y_2O_3-infiltrated SPPS YSZ TBCs with IPBs, and (b) XRD patterns of infiltrated SPPS YSZ TBCs before and after CMAS paste tests

Also worth noting in this modified system is the fact that the cyclic life of SPPS YSZ with IPBs was actually shortened by the Y_2O_3 infiltration in the paste tests (**Fig. 7-4**). As indicated by the spritz tests, the stress-relieving microstructure was crucial feature that benefits a prolonged service time under CMAS attack. Infiltrating blocking materials into the vertical cracks and horizontal pores would certainly compromise that stress-relieving capability. In **Fig. 7-9**, it was

clearly shown that delamination along the inter-pass boundaries became an issue when the vertical cracks disappeared due to the materials infiltration, either by Y_2O_3 or CMAS.

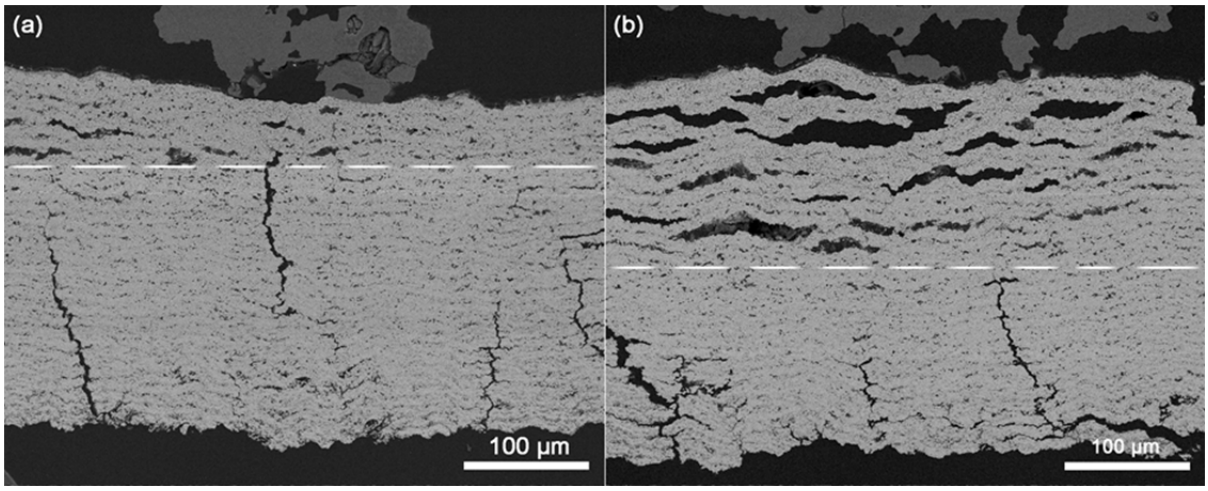

Fig. 7-9 Delamination along IPBs observed at different locations (a & b) in Y_2O_3-infiltrated SPPS YSZ TBCs with IPBs

7.4 Discussion

In summary, failures in all four TBC systems occurred as spallation close to the topcoat/TGO interfaces in the spritz tests, again similar to the cyclic durability test results. In the case of SPPS YSZ with IPBs, the layered porosity gradually was filled with molten glassy melt (**Fig. 7-10a2**) as it approached the topcoat surfaces. While in the paste tests, each TBC system displayed a different failure mode (**Fig. 7-10b**):

(i) for APS YSZ baseline samples, a flakey appearance was observed after the CMAS-penetrated segments caused cracks to form right beneath;

(ii) for SPPS YSZ with IPBs, coatings delamination occurred at TGO to topcoat interface, as the microstructure lost its strain tolerance due to the full CMAS penetration;

(iii) for double-layer SPPS GZO/YSZ TBCs, the spallation was sporadically spotted close to the PSL/interlayer interface with CMAS trapped half-way in the GZO layer, while the underlying SPPS YSZ layer remained protected and intact; and

(iv) for Al_2O_3/TiO_2-doped YSZ TBCs, CMAS fully penetrated the coatings, causing the whole coatings to come off at the topcoat/TGO interface, yet unlike other TBC systems, TBC-CMAS reactions were visually apparent as detailed patterning occured with the formation of anorthite.

Both the spritz and paste tests were employed in this study to evaluate CMAS-TBC interactions under engine-relevant environments, but rather different results were obtained. The spritz test was preferred at first as it better simulates the periodic slow uptake of particulate impurities in turbine engines; however, the measured TBC lifetime to failure in the CMAS-TBC interaction tests turned out to be primarily related to the stress-relieving microstructure, rather than the infiltration-inhibiting protective surface layer. The paste tests, which represent only a few realistic scenarios, such as sandstorms or long-time CMAS built-up metaling later under extreme operating conditions, succeeded in capturing the inhibition reaction and demonstrated the advantage of introducing the GZO PSLs (**Fig. 7-5**). It was also demonstrated that in the spritz tests the protective mechanisms known for GZO were not effective in protecting the TBC from CMAS infiltration, whereas they were effective in paste tests.

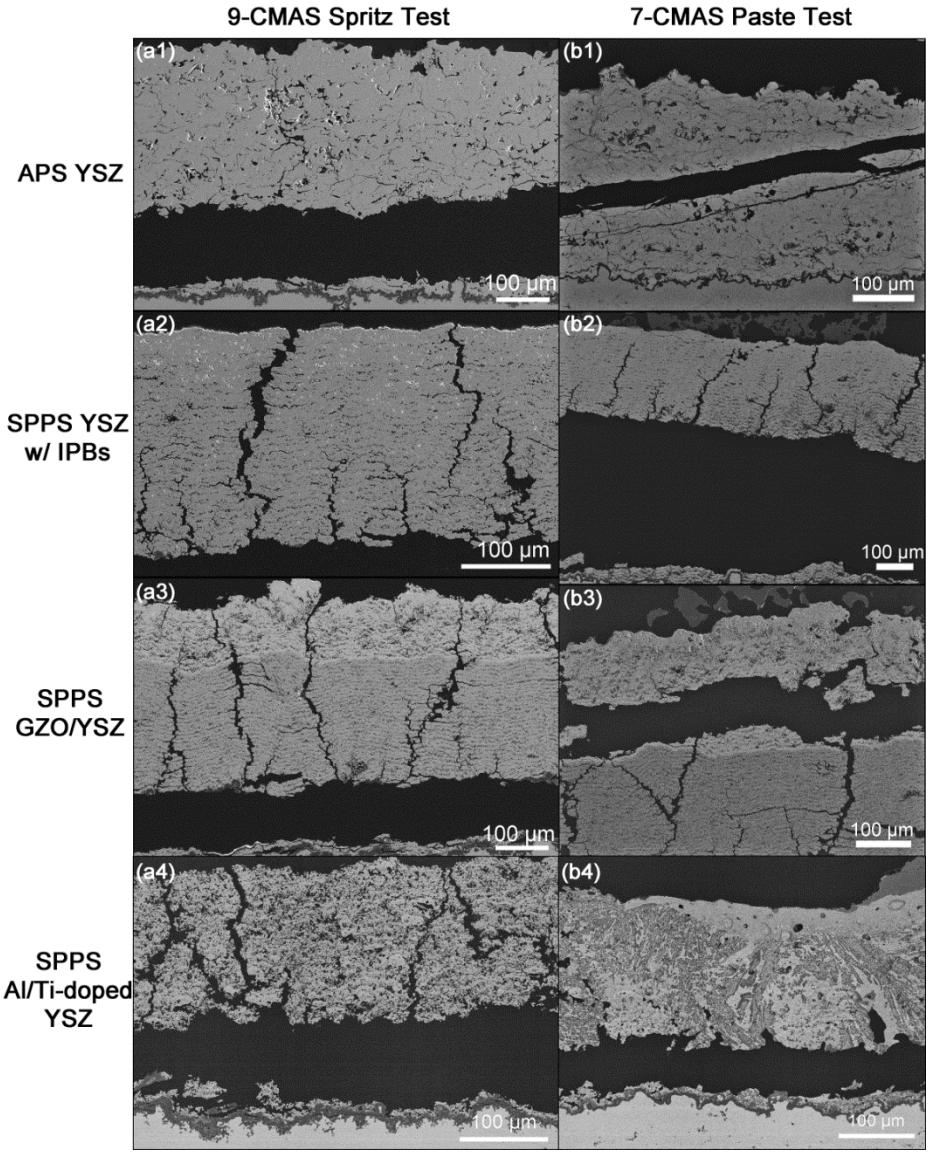

Fig. 7-10 Comparison of failure sites between both CMAS resistance tests

The drastic difference between these two tests raises a question: what leads to the protective mechanism in the GZO PSLs. The amount of CMAS and how the CMAS is applied are likely answers, based on the result of this study. The formation kinetics of blocking phases and CMAS infiltration rates are competing, inter-related factors in the context of CMAS attack. When CMAS is repeatedly applied at a small dose in an isothermal environment (spritz tests), the small CMAS accumulation generally reacts with the PSL surface, leaving a less amount the materials

to attack the underlying section in each spritz, and the occurrence of the blocking reaction is considerably constrained to the coating surface. As spritzing is repeated, the inhibiting reaction, progresses slowly in a layer-by-layer fashion, leading to a continuing attack. Due to the small doses, the CMAS damage is progressive, especially at the bottom half of the topcoat; therefore the test itself exhibits similar results as the thermal cyclic durability test, likely to be governed by the growing stresses on the TGO surface. While in the paste test, the formation kinetics of blocking phases are accelerated by the excessive amount of CMAS paste in the first cycle, and effectively initiates the protective mechanism of GZO, preventing CMAS from further attacking the TBC. In the end, the characterization of CMAS resistance is intricate by itself and largely dependent on the testing conditions. It remains a critical question as to which of these tests if any can be deemed “representative” of engine environments.

Chapter 8. Investigation of TBCs' Resistance to High Temperature Moisture

High temperature moisture is a concern for an advanced TBC system, especially when it is used in the IGCC steam turbine engines.

8.1 The high temperature moisture test on YSZ TBCs

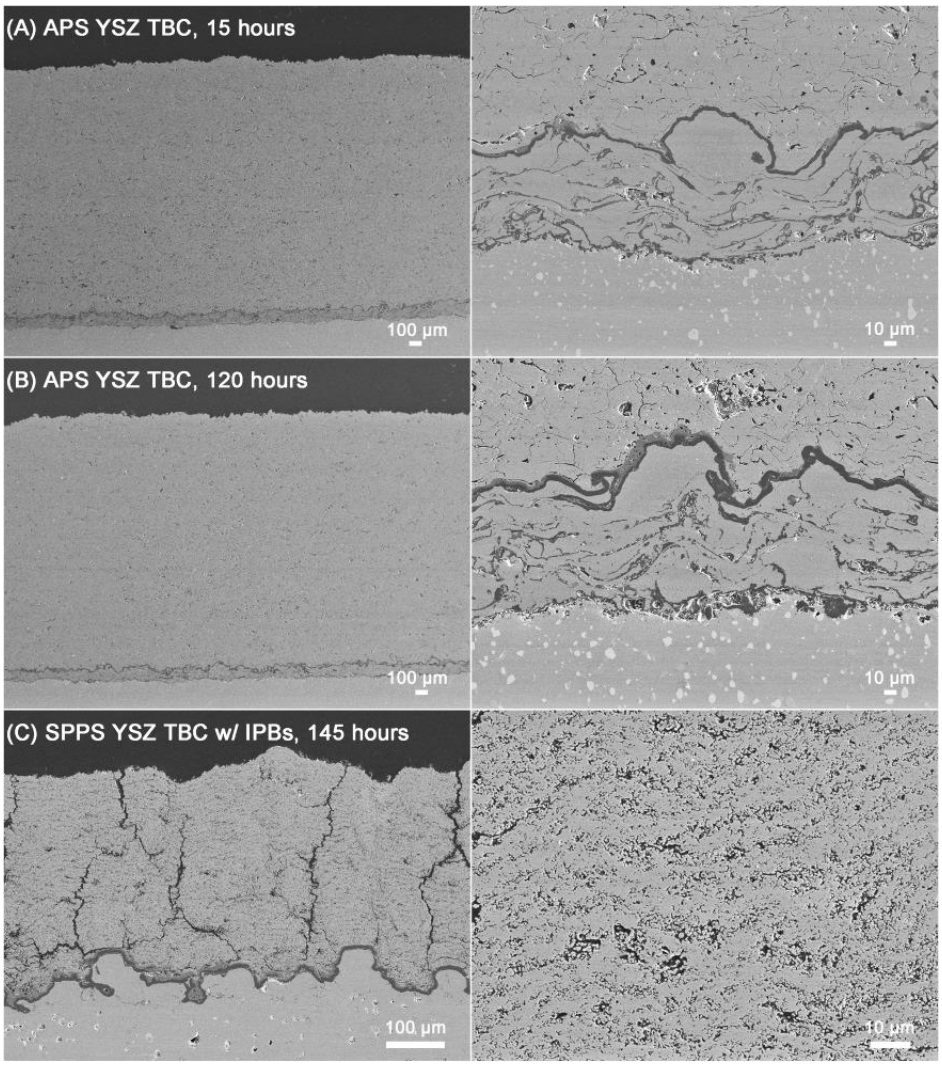

Fig. 8-1 Cross-sectional micrographs of APS and YSZ TBCs tested for 100+ hours under high temperature moisture

Though the superalloy substrates were severely oxidized as evidenced by the formation of cobalt/nickel oxide on the substrate bottom surfaces, the APS YSZ baseline and the SPPS YSZ

TBC with IPBs macroscopically stayed intact after 120-hour and 145-hour exposures to 30% humidity at 1121^{o}C, respectively. SEM cross-sectional characterization confirmed that the microstructures of the both TBCs remained unchanged after the 100+ heat treatment under high temperature moisture (**Fig. 8-1**), including the layered porosity of IPBs.

No phase transformation was observed as well, retaining the primarily *t'*-YSZ phases while a small amount of residual *m*-zirconia remained in the APS YSZ from the original deposition process, as shown in **Fig. 8-2**. Overall, regardless of the deposition method, both YSZ TBCs retain chemical and microstructural stability under high-temperature moisture.

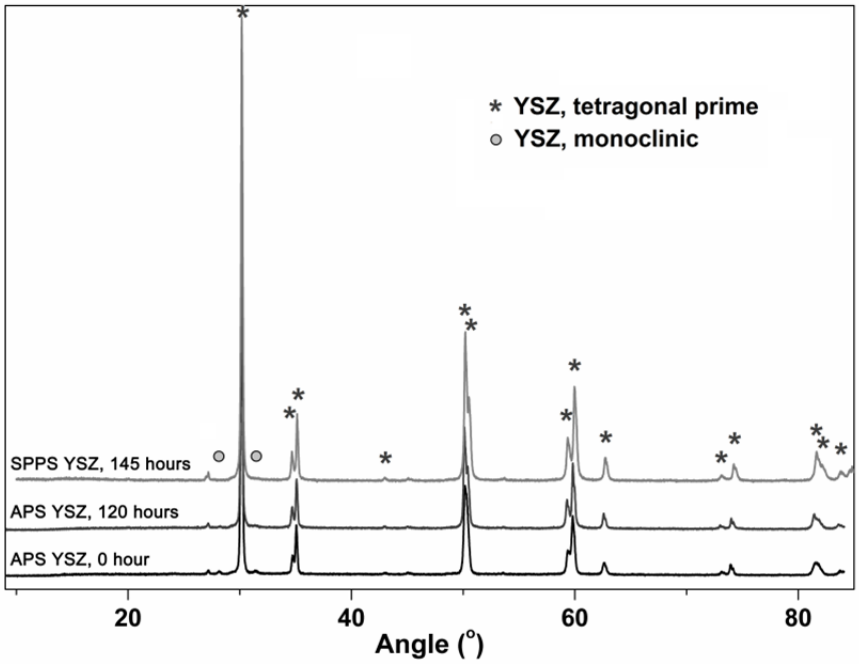

Fig. 8-2 XRD patterns of YSZ TBCs after 100+ hours exposures to high temperature moisture

8.2 The high temperature moisture test on modified YSZ-based TBCs

8.2.1 Double-layer GZO/YSZ SPPS TBCs

After 300 hours of heat treatment in the high temperature moisture rig (**Fig. 2-1**), SEM micrographs showed clear and intact PSL/interlayer and topcoat/TGO interfaces, with the strain

tolerant vertical cracks that ran through both layers unchanged (**Fig. 8-3a**). No change in the diffraction patterns was evident during heat treatment (**Fig. 8-3b**) including the preservation f the predominant fluorite phase, which suggested the phases in the GZO PSLs were stable in the high temperature humid environments. As shown earlier, APS and SPPS YSZ TBCs alone also retained the *t'*-phase under the same moist conditions. As for the interfacial regions between GZO/YSZ, SEM secondary/backscattered signals revealed no observable changes. A smaller size scale interface characterization may be needed using TEM imaging, yet in this limited testing, the double-layer TBCs, consisting of SPPS GZO PSLs and YSZ interlayers, showed no signs of formation of new phases under high temperature steam.

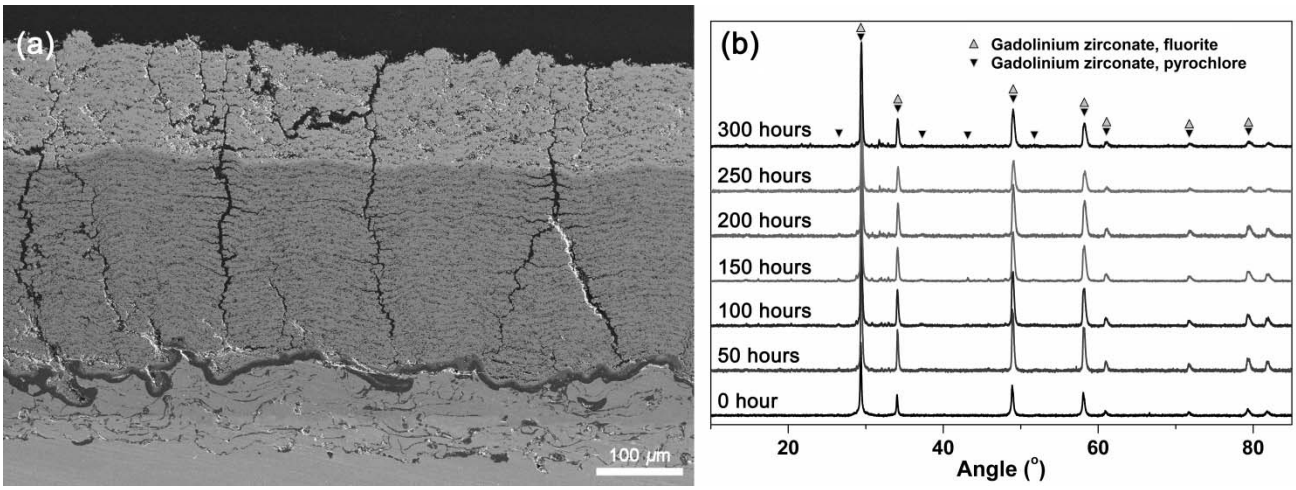

Fig. 8-3 High temperature steam test after 300 hours: (a) cross-section micrograph showing interface stability in the SPPS double-layer microstructure, and (b) overlaid GZO PSL XRD patterns showing the phase stability.

8.2.2 Al_2O_3/TiO_2-doped SPPS YSZ TBCs

Under the same high temperature moist conditions (30% humidity at 1121°C), the detrimental *t'*-YSZ to *m*-YSZ transformation was observed in the Al_2O_3/TiO_2-doped SPPS YSZ TBCs (**Fig. 8-4a**). To better understand the occurrence of this phase transformation, a parallel dry test using the same tube furnace was scheduled, in which all testing parameters were kept unchanged

expect for the disconnection of water vapor. As shown in **Fig. 8-4b**, after being tested for 400 hours, doped YSZ samples were observed with no *t'-m* phase transformation, which indicated the high temperature moisture did somehow accelerate the phase change.

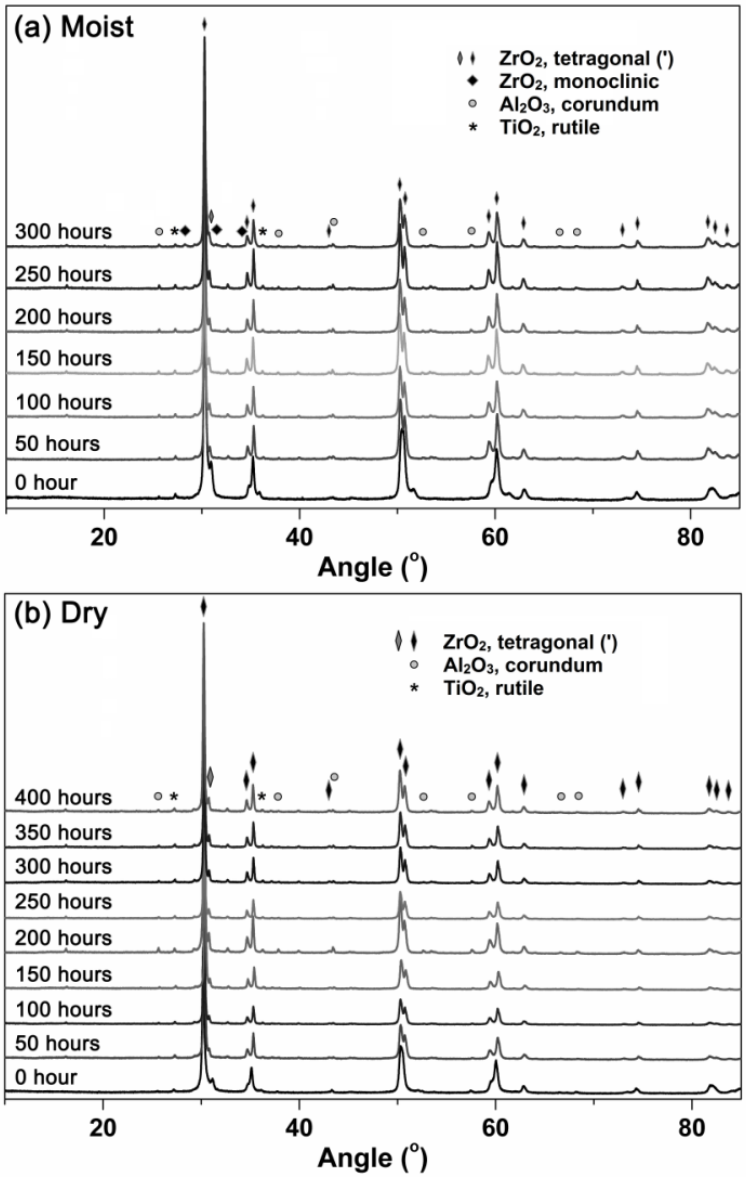

Fig. 8-4 XRD characterization of Al_2O_3/TiO_2-doped YSZ TBCs tested under high temperature (a) moist and (b) dry conditions

Generally speaking, the *t-m* transformation in zirconia is a diffusionless martensitic transformation by nature [163]. After stabilized with yttria, *t'*-YSZ is generally considered to be

non-transformable, yet after 400 hours of annealing at 1200°C, an significant amount of *t-m* phase transformation was still observed in plasma-sprayed *t'*-YSZ coatings [164], due to the yttrium-diffusion induced de-stabilization of zirconia [27]. Even though the phase stability was claimed to be enhanced in the composite SPS Al_2O_3/YSZ TBCs [165], segregation of yttria into the grain boundaries was detected in annealed 9.4mol%-doped YSZ, leading to yttrium-depletion in the YSZ lattice [166].

On a relevant note, a mechanism for *m*-zirconia formation was recently proposed for a CuO-YSZ system as following: CuO transfers oxygen through a CuO/Cu_2O transformation, and the oxygen atom is then transported to the oxygen-vacancy in the YSZ lattice, forcing the yttrium ions to mitigate inward to maintain charge neutrality, while leaving behind the un-stabilized ZrO_2 to transform to monoclinic [167]. Rutile TiO_2, in our case, is a known non-stoichiometric oxide that can exhibit a complex defect structure involving oxygen vacancies. In addition, the oxygen vacancies on the TiO_2 surfaces are found to be active sites for absorption and dissociation of water molecules [168]. As a fast-ion conductor, YSZ can experience a similar *t'-t/c-m* transformation route as in the case of CuO-doped YSZ, in which rutile TiO_2 performs as an active oxygen acceptor/donor, transporting the oxygen ion to the YSZ lattice. This phase transformation is possible to be even accelerated under such humid and oxidizing conditions as the high-temperature moisture test, due to TiO_2's affinity to water. However, more experimental proofs are needed to support this hypothesis regarding the formation of monoclinic phase in Al_2O_3/TiO_2-doped SPPS YSZ TBCs under the high temperature moisture, e.g. to confirm if it is the rutile TiO_2 that is responsible for the high temperature oxygen transfer, or it's actually some other phases. Nonetheless, based on what was observed in both moist and dry high temperature

tube tests, there surely is a concern if Al_2O_3/TiO_2-doped YSZ TBCs would remain phase stable in the moist IGCC environment for the CMAS attack to occur while retaining good durability.

Chapter 9. Conclusions

9.1 Durable low thermal conductivity SPPS YSZ TBCs with IPBs

The SPPS process can produce YSZ TBCs with layered porosity, called as *Inter-Pass Boundaries* (IPBs). By optimizing this microstructural feature, the thermal conductivity of the coating can be further reduced to around 0.6 $W \cdot m^{-1}K^{-1}$, equivalent to an approximately 50% reduction comparing to the commercially standard APS coatings and similar to most second generation TBCs containing more expensive, less tough rare earth containing TBCs. The initial approach used to calculate the thermal conductivity from micrographs using the OOF FEA was found unreliable. Therefore, thermal conductivity was directly measured from the TBC using the laser flash method. Through extensive spray parameter optimization involving hundreds of spray trials and laser flash measurements, the SPPS process has been adjusted to produce YSZ TBCs with 20% porosity or less that reproducibly have an average thermal conductivity of 0.623 $Wm^{-1}K^{-1}$. It has further been demonstrated that the cyclic furnace durability and the erosion resistance of these low-thermal-conductivity coatings is comparable to APS YSZ TBCs used extensively in current generation turbine engines.

9.2 Double-layer GZO/YSZ SPPS TBCs

The SPPS process was successfully employed to deposit a double-layer TBC topcoat, consisting of a CMAS infiltration-inhibiting GZO PSL and an SPPS-deposited YSZ layer with a thermal conductivity that has roughly 50% reduction than a typical APS TBC. The deposited GZO PSLs were composed of low-thermal-conductivity pyrochlore and fluorite phases, while other beneficial microstructural features of the SPPS process, e.g. the strain-tolerant through-thickness

vertical cracks, were incorporated to the double-layer coating as well. The thermal cyclic durability of double-layer SPPS GZO/YSZ TBCs was shown to be comparable to single-layer SPPS YSZ TBCs and superior to the APS YSZ baseline. Unlike previous APS double-layer coatings [142], no failures were observed at the GZO to YSZ interface. It is likely that the stress-relieving vertical cracks play an important role in mitigating the adverse effects of differential sintering. The excellent bonding between the GZO and YSZ layers seen in the SEM photos is also helpful in this regard.

9.3 Al_2O_3/TiO_2-doped SPPS YSZ TBCs

The study of producing doped SPPS YSZ TBCs for enhanced CMAS resistance started with adding increasing amounts of aluminum nitrates to the standard YSZ precursor solution. A clear trend of reduction in exothermic characteristics in the precursors was later discovered and led to highly porous as-sprayed coatings. Several processing modifications were employed to densify the coatings, among which the addition of PVA had the most significant effect, as it not only modified the fluid property but also changed the precursor thermal characteristics positively.

Due to complex physical and chemical natures of titanium precursors, several different precursor solutions were prepared for the doping both Al_2O_3 and TiO_2 into the YSZ matrix. The alcohol-based precursor solutions give generally more dense coatings and responded poorly to processing parameters. The excess heat from the burning of the solvent close to the substrates also created undesirable microstructural defects. In contrast, the aqueous solutions have been showed to provide good process repeatability and a great potential for reproducing the IPB features, and therefore is selected as the precursor solution for the deposition of the doped TBCs.

9.4 Selection of the optimal TBC system for IGCC environments

After an additional modification to the SPPS YSZ-based TBCs to enhance the resistance to CMAS, which involved infiltration of CMAS-blocking materials into coating porosity, all TBC systems produced in this study were evaluated and compared side by side for the optimal properties and performances.

In terms of thermal conductivity, the values for both optimized SPPS YSZ TBCs with IPBs and SPPS GZO PSLs are relatively low, 0.623 and 0.53 $Wm^{-1}K^{-1}$ respectively. Al_2O_3/TiO_2-doped SPPS YSZ TBCs, on the other hand, was measured to be 0.85~1.3 $W{\cdot}m^{-1}K^{-1}$, depending on the coating density. Thermal conductivity of infiltrated SPPS YSZ TBCs, though not measured specifically, will have no doubt to be higher than SPPS IPB YSZ TBCs, as layered porosity is sacrificed to the infiltration of blocking materials.

The high temperature moisture test confirmed the microstructural and phase stability of all YSZ TBCs and the double-layer SPPS GZO/YSZ TBCs (both in each individual layers and at the interfaces, based on limited testing). However, a traceable amount of phase transformation to *m*-ZrO_2 was observed in Al_2O_3/TiO_2-doped YSZ TBCs under high temperature humid conditions for an extended testing period. In comparison, similar tests under dry conditions in the same experiment setup yielded no such detrimental phase transformation, which raised durability concerns for reliable performance of the Al_2O_3/TiO_2-doped TBCs under high temperature moisture. Tentative explanations for this phenomenon have also been suggested.

As for the high temperature resistance to environmental deposits, CMAS, the cross-sectional micrographs as well as the EDS Ca-mapping of all TBC systems under the paste test are summarized in **Fig. 9-1**.

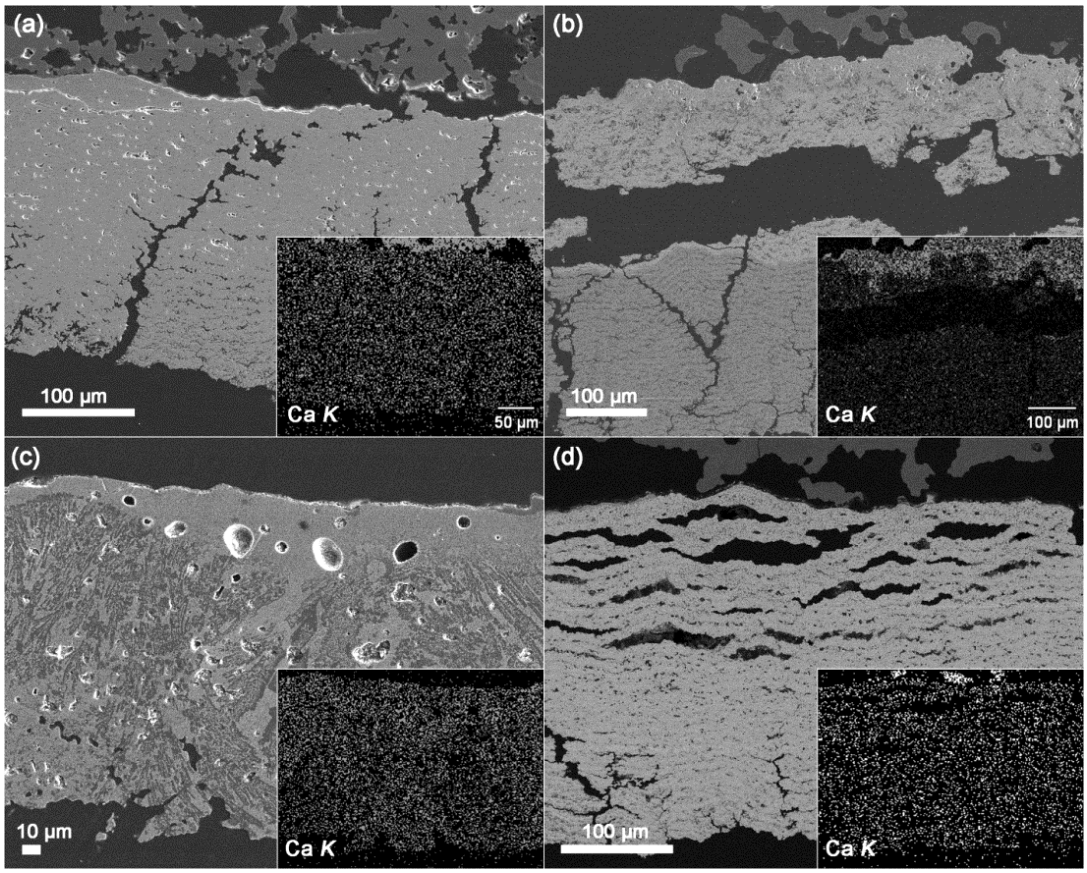

Fig. 9-1 CMAS-infiltration inhibiting reactions in different SPPS YSZ-based TBCs systems: (a) SPPS YSZ with IPBs, (b) double-layer SPPS GZO/YSZ, (c) Al_2O_3/TiO_2-doped SPPS YSZ, and (d) Y_2O_3-infiltrated SPPS YSZ TBCs with IPBs

All TBC systems suffered from the penetration of CMAS in one way or another. Three of the four systems though, excluding the double-layer GZO/YSZ TBCs, experienced spallation at the topcoat/TGO interface and risked losing their thermal-insulating capabilities. The TBC-CMAS interactions varied in each TBC system: (a) in SPPS YSZ with IPBs, CMAS when penetrated through the coating, filled in all layered porosity and cracks, causing the microstructure to lose its strain tolerance and likely the low thermal conductivity; (b) in double-layer SPPS GZO/YSZ TBCs, CMAS was trapped in the GZO surface layer while protecting the underlying SPPS YSZ; (c) the dopants of Al_2O_3 and TiO_2 in YSZ TBCs indeed increased coatings' reactivity to CMAS, but the reaction product of anorthite was found to be ineffective at arresting the CMAS

penetration front; and finally (4) in Y_2O_3-infiltrated SPPS YSZ, the microstructural strain tolerance was compromised which causing spallation to occur along the IPBs.

Based on all the testing results, it has become evident that in order to seek and evaluate potential material modifications for CMAS resistance, one has to consider the every stage of CMAS damages. From the materials properties point of view, the CMAS-resisting candidate materials should exhibit either excellent reactivity to CMAS or completely inertness, which in most cases will be suggested directly by the optical basicity theory. On the other hand, in order for the sacrificing materials to be effective in harnessing the CMAS penetration front, the kinetics of the CMAS inhibiting reaction should always outrun the infiltration/diffusion of CMAS in the TBCs, otherwise no matter how effective the infiltration-inhibiting phase may appear, the reaction will be too slow to be valid as suggested by the Spritz test results. Besides, the stability of inhibiting phases, not only in the presence of CMAS but also at elevated temperatures, can also be a determining factor in terms of overall resistance performance.

In conclusion, of all modified YSZ-based SPPS TBCs, only the double-layer SPPS GZO/YSZ TBCs exhibited a combination of low thermal conductivity, good cyclic durability, excellent high temperature resistance to humidity, and greatly-enhanced CMAS resistance, making it the optimal TBC system in this study to best suit the application in the IGCC environments. The only additional issue to be resolved is to develop a means to avoid producing IPB coatings with occasional weak layers, as part of the quality control. The questions that remain are that all systems were not resistant to CMAS attack in the spritz tests and it is important to know if this is engine relevant.

References

[1] S. Shelley, "IGCC power generation-improving the 'power island'," *Chem. Eng. Prog.,* vol. 104, no. 10, p. 12, 2008.

[2] Anonymous, "U.S. DOE touts new gas turbine for IGCC, NGCC plants," *Gasification News,* vol. 16, no. 13, p. 13, 2013.

[3] D. R. Clarke, M. Oechsner and N. P. Padture, "Thermal barrier coatings for more efficient gas-turbine engines," *MRS Bull.,* vol. 37, no. 10, pp. 891-898, 2012.

[4] R. Rost, "Clean coal technologies on example of Vanttenfall's power plant projects BOXBERG unit R and MOORBURG," Vattenfall, Astana Kazakhstan, 2013.

[5] D. R. Clarke and C. G. Levi, "Materials design for the next generation thermal barrier coatings," *Annu. Rev. Mater. Res.,* vol. 33, no. 1, pp. 383-417, 2003.

[6] J. H. Perepezko, "The hotter the engine, the better," *Science,* vol. 326, no. 5956, pp. 1068-1069, 2009.

[7] National Research Council, "Coatings for high temperature structural materials: trends and opportunities," National Academy of Sciences, Washington DC, 1996.

[8] R. L. Jones, in *Metallurgical and ceramic protective coatings*, London, Chapman and Hall, 1996.

[9] N. P. Padture, M. Gell and E. H. Jordan, "Thermal barrier coatings for gas-turbine engine applications," *Science,* vol. 296, no. 5566, pp. 280-284, 2002.

[10] A. Maricocchi, A. Bartz and D. Wortman, "PVD TBC experience on GE aircraft engines," *J. Therm. Spray Technol.,* vol. 6, no. 2, pp. 193-198, 1997.

[11] A. Feuerstein, J. Knapp, T. Taylor, A. Ashary, A. Bolcavage and N. Hitchman, "Technical and economical aspects of current thermal barrier coating systems for gas turbine engines by thermal spray and EBPVD: A review," *J. Therm. Spray Technol.,* vol. 17, no. 2, pp. 199-213, 2008.

[12] F. Talboom and J. Grafwallner, "Nickel or cobalt base with a coating containing iron, chromium and aluminum". US Patent 3542530, 1970.

[13] D. Evans and R. Elam, "Cobalt base coating for the superalloys". US Patent 3676085, 1972.

[14] G. Goward, D. Boone and F. Pettit, "High temperature oxidation-resistant coating alloy". US Patent 3754903, 1973.

[15] R. Hecht, G. Goward and R. Elam, "High-temperature NiCoCrAlY coatings". US Patent 3928026, 1975.

[16] G. H. Meirer and F. S. Pettit, "The oxidation behavior of intermetallic compounds," *Mater. Sci. Eng., A,* vol. 153, no. 1-2, pp. 548-560, 1992.

[17] P. Kofstad, High temperature corrosion, Amsterdam: Elsevier, 1988.

[18] R. A. Miller, "Oxidation-based model for thermal barrier coatings," *J. Am. Ceram. Soc.,* vol. 67, no. 8, pp. 517-521, 1984.

[19] V. Sergo and D. R. Clarke, "Observation of subcritical spall propagation of a thermal barrier coating," *J. Am. Ceram. Soc.,* vol. 81, no. 12, pp. 3237-3242, 1998.

[20] A. G. Evans, D. R. Mumm, J. W. Hutchinson, G. H. Meier and F. S. Pettit, "Mechanisms controlling the durability of thermal barrier coatings," *Prog. Mater. Sci.,* vol. 46, no. 5, pp. 505-553, 2001.

[21] V. K. Tolpygo and D. R. Clarke, "Surface rumpling of a (Ni,Pt)Al bond coat induced by cyclic oxidation," *Acta Mater.,* vol. 48, no. 13, pp. 3283-3293, 2000.

[22] A. M. Karlsson, J. W. Hutchinson and A. G. Evans, "A fundamental model of cyclic instabilities in thermal barrier systems," *J. Mech. Phys. Solids,* vol. 50, no. 8, pp. 1565-1589, 2002.

[23] V. K. Tolpygo, D. R. Clarke and K. S. Murphy, "Oxidation-induced failure of EB-PVD thermal barrier coatings," *Surf. Coat. Technol.,* Vols. 146-147, pp. 124-131, 2001.

[24] A. G. Evans, D. R. Clarke and C. G. Levi, "The influence of oxides on the performance of advanced gas turbines," *J. Eur. Ceram. Soc.,* vol. 28, pp. 1405-1419, 2008.

[25] D. J. Green, R. H. Hannink and M. V. Swain, Transformation toughening of ceramics, Boca Raton FL: CRC Press, 1989.

[26] S. Stecura, "Optimization of the NiCrAlY/ZrO_2-Y_2O_3 thermal barrier system," *NASA/TM 86905,* 1985.

[27] R. Vassen, A. Stuke and D. Stover, "Recent develpments in the field of thermal barrier coatings," *J. Therm. Spray Technol.,* vol. 18, no. 2, pp. 181-186, 2009.

[28] J. Ilavsky and J. K. Stalick, "Phase composition and its changes during annealing of plasma-sprayed YSZ," *Surf. Coat. Technol.,* vol. 127, no. 2, pp. 120-129, 2000.

[29] U. Schulz, "Phase transformation in EB-PVD yttria partially stabilized zirconia thermal barrier coatings during annealing," *J. Am. Ceram. Soc.,* vol. 83, no. 4, pp. 904-910, 2000.

[30] S. Kraemer, J. Yang and C. G. Levi, "Infiltration-inhibiting reaction of gadolinium zirconate thermal barrier coatings with CMAS melts," *J. Am. Ceram. Soc.,* vol. 91, no. 2, pp. 576-583, 2008.

[31] L. Li, N. Hitchman and J. Knapp, "Failure of thermal barrier coatings subjected to CMAS attack," *J. Therm. Spray Technol.,* vol. 19, no. 1-2, pp. 148-155, 2010.

[32] S. Kraemer, J. Yang and C. G. Levi, "Thermochemical interaction of thermal barrier coatings with molten CaO-MgO-Al_2O_3-SiO_2 (CMAS) deposits," *J. Am. Ceram. Soc.,* vol. 89, no. 10, pp. 3167-3175, 2006.

[33] J. Wu, H.-b. Guo, Y.-z. Gao and S.-k. Gong, "Microstructure and thermo-physical properties of yttria stabilized zirconia coatings with CMAS deposits," *J. Eur. Ceram. Soc.,* vol. 31, no. 10, pp. 1881-1888, 2011.

[34] W. Ma, D. E. Mack, R. Vassen and D. Stover, "Perovskite-type Strontium Zirconate as A New Material for Thermal Barrier Coatings," *J. Am. Ceram. Soc.,* vol. 91, no. 8, pp. 2630-2635, 2008.

[35] W. Ma, D. Mack, J. Malzbender, R. Vassen and D. Stover, "Yb_2O_3 and Gd_2O_3 doped strontium zirconate for thermal barrier coatings," *J. Eur. Ceram. Soc.,* vol. 28, no. 16, pp. 3071-3081, 2008.

[36] R. Vassen, X. Cao, F. Tietz, B. Basu and D. Stover, "Zirconates as new materials for thermal

barrier coatings," *J. Am. Ceram. Soc.,* vol. 83, no. 8, pp. 2023-2028, 2000.

[37] J. Wu, X. Wei, N. P. Padture, P. G. Klemens, M. Gell, E. Garcia, P. Miranzo and M. I. Osendi, "Low-thermal-conductivity rare-earth zriconates for potential thermal-barrier-coating applications," *J. Am. Ceram. Soc.,* vol. 85, no. 12, pp. 3031-3035, 2002.

[38] E. H. Jordan, M. Gell, C. Jiang, J. Wang and B. Nair, "High temperature thermal barrier coating made by the solution precursor plasma spray process," in *ASME Turbo Expo 2014: Turbine Technical Conference and Exposition*, Dusseldorf, Germany, 2014.

[39] Y. J. Su, R. W. Trice, K. T. Faber, H. Wang and W. D. Porter, "Thermal conductivity, phase stability, and oxidation resistance of $Y_3Al_5O_{12}$(YAG)/Y_2O_3-ZrO_2(YSZ) thermal-barrier coatings," *Oxid. Met.,* vol. 61, no. 3, pp. 253-271, 2004.

[40] R. Vassen, Y. Kagawa, R. Subramanian, P. Zombo and D. Zhu, "Testing and evaluation of thermal-barrier coatings," *MRS Bull.,* vol. 37, no. 10, pp. 911-916, 2012.

[41] X. Q. Cao, R. Vassen and D. Stover, "Ceramic materials for thermal barrier coatings," *J. Eur. Ceram. Soc.,* vol. 24, pp. 1-10, 2004.

[42] G. Dwivedi, Y. Tan, V. Viswanathan and S. Sampath, "Process-property relationship for air plasma-sprayed gadolinium zirconate coatings," *J. Therm. Spray Technol.,* vol. 24, no. 3, pp. 454-466, 2015.

[43] A. R. Krause, B. S. Senturk, H. F. Garces, G. Dwivedi, A. L. Ortiz, S. Sampath and N. P. Padture, "$2ZrO_2$:Y_2O_3 thermal barrier coatings resistant to degredation by molten CMAS: part I, optical basicity considerations and processing," *J. Am. Ceram. Soc.,* vol. 97, no. 12, pp. 3943-3949, 2014.

[44] J. A. Duffy, "Acid-base reactions of transition metal oxides in the solid state," *J. Am. Ceram. Soc.,* vol. 80, no. 6, pp. 1416-1420, 1997.

[45] A. Aygun, A. L. Vasiliev, N. P. Padture and X. Ma, "Novel thermal barrier coatings that are resistant to high-temperature attack by glassy deposits," *Acta Mater.,* vol. 55, no. 20, pp. 6734-6745, 2007.

[46] J. A. Duffy, "Optical basicity of titanium (IV) oxide and zirconium (IV) oxide," *J. Am. Ceram. Soc.,* vol. 72, no. 10, pp. 2012-2013, 1989.

[47] C. G. Levi, J. W. Hutchinson, M.-H. Vidal-Setif and C. A. Johnson, "Environmental degradation of thermal barrier coatins by molten deposits," *MRS Bull.,* vol. 37, no. 10, pp. 932-941, 2012.

[48] J. M. Drexler, A. L. Ortiz and N. P. Padture, "Composition effects of thermal barrier coating ceramics on their interaction with molten Ca-Mg-Al-silicate (CMAS) glass," *Acta Mater.,* vol. 60, no. 15, pp. 5437-5447, 2012.

[49] M. J. Maloney, "Thermal barrier coating systems and materials". US Patent 6177200, 4 September 2001.

[50] M. Freling, M. J. Maloney, D. A. Litton, K. W. Schlichting, J. G. Smeggil and D. B. Snow, "Thermal barrier coating compositions, processes for applying same and articles coated with same". US Patent 7455913 B2, 10 January 2008.

[51] M. Freling, K. W. Schlichting, M. J. Maloney, D. A. Litton, J. G. Smeggil and D. B. Snow, "CMAS resistant thermal barrier coating". US Patent 20070172703 A1, 26 July 2007.

[52] D. A. Litton, K. W. Schlichting, M. Freling, J. G. Smeggil, D. B. Snow and M. J. Maloney, "Process of forming durable reactive thermal barrier coatings". US Patent 8343587 B2, 1 January 2013.

[53] D. A. Litton, K. W. Schlichting, M. Freling, J. G. Smeggil, D. B. Snow and M. J. Maloney, "Durable reactive thermal barrier coatings". US Patent 7662489 B2, 16 February 2010.

[54] J. M. Drexler, K. Shinoda, A. L. Ortiz, D. Li, A. L. Vasiliev, A. D. Gledhill, S. Sampath and N. P. Padture, "Air-plasma-sprayed thermal barrier coatings that are resistant to high-temperature attack by glassy deposits," *Acta Mater.,* vol. 58, no. 20, pp. 6835-6844, 2010.

[55] U. Bast and E. Schumann, "Development of Novel Oxide Materials for TBCs," *Ceram. Eng. Sci. Proc.,* vol. 23, no. 4, pp. 525-532, 2002.

[56] S. J. Grisaffe, S. R. Levine and J. S. Clark, "Thermal barrier coatings," in *National Aeronautics and Space Adminitration, NASA-LeRC*, Cleveland OH, 1978.

[57] C. H. Liebert and R. A. Miller, "Ceramic thermal barrier coatings," *Ind. Eng. Chem. Prod. Res. Dev.,* vol. 23, no. 3, pp. 344-349, 1984.

[58] A. Jadhav, N. P. Padture, F. Wu, E. H. Jordan and M. Gell, "Thick ceramic thermal barrier coatings with high durability deposited using solution precursor plasma spray," *Mater. Sci. Eng., A,* vol. 405, no. 1, pp. 313-320, 2005.

[59] C. H. Liebert and S. Stecura, "Ceramic thermal protective coating withstands hostile environment of rotating turbine blades," in *NASA Technical Briefs, NASA-LeRC*, Cleveland OH, 1975.

[60] R. A. Miller, "Thermal barrier coatings for aircraft engines: history and directions," *J. Therm. Spray Technol.,* vol. 6, no. 1, pp. 35-42, 1997.

[61] P. G. Klemens, in *Thermal Conductivity*, vol. 23, K. E. Willis, R. B. Dinwiddie and R. S. Graves, Eds., Lancaster, PA: Technomics, 1993, p. 209.

[62] M. Peters, K. Fritscher, G. Staniek, W. A. Kaysser and U. Schulz, "Design and properties of thermal barrier coatings for advanced turbine engines,"*Materialwiss Werkst,* vol. 28, no. 8, pp. 357-362, 1997.

[63] D. M. Gray, Y. -C. Lau, C. A. Johnson, M. P. Borom and W. A. Nelson, "Thermal barrier coatings having an improved columnar microstructure". US Patent 5830586, 3 November 1998.

[64] M. Gell, E. H. Jordan, M. Telcholz, B. M. Cetegen, N. P. Padture, L. Xie, D. Chen, X. Ma and J. Roth, "Thermal barrier coatings made by the solution precursor plasma spray process," *J. Therm. Spray Technol.,* vol. 17, no. 1, pp. 124-135, 2008.

[65] P. Fauchais, A. Joulia, S. Goutier, C. Chazelas, M. Vardelle, A. Vardelle and S. Rossignol, "Suspension and solution plasma spraying," *J. Phys. D: Appl. Phys.,* vol. 46, no. 22, p. 224015, 2013.

[66] D. Chen, E. H. Jordan and M. Gell, "The solution precursor plasma coatings: influence of solvent type," *Plasma Chem. Plasma Process.,* vol. 30, pp. 111-119, 2010.

[67] C. K. Muoto, E. H. Jordan, M. Gell and M. Aindow, "Identification of desirable precursor properties for solution precursor plasma spray," *J. Therm. Spray Technol.,* vol. 20, no. 4, p. 802, 2011.

[68] B. D. White, O. Kesler and L. Rose, "Air plasma spray processing and electrochemical characterization of SOFC composite cathodes," *J. Power Sources,* vol. 178, no. 1, pp. 334-343, 2008.

[69] S. Janisson, E. Meillot, A. Vardelle, J. F. Coudert, B. Pateyron and P. Faurchais, "Plasma spraying using Ar-He-H_2 gas mixtures," *J. Therm. Spray Technol.,* vol. 8, no. 4, pp. 554-552, 1999.

[70] R. Tomaszek, L. Pawlowski, L. Gengenmbre, J. Laureyns and A. Le Maguer, "Microstructure of suspension plasma sprayed multilayer coatings of hydroxyapatite and titanium oxide," *Surf. Coat. Technol.,* vol. 201, no. 16-17, pp. 7432-7440, 2007.

[71] E. H. Jordan, M. Gell, P. Bonzani, D. Chen, S. Basu, B. M. Cetegen, F. Wu and X. Ma, "Making dense coatings with the solution precursor plasma spray process," in *Thermal Spray 2007: Global Coating Solution*, Materials Park OH, ASM International, 2007, pp. 463-470.

[72] L. Pawlowski, "Suspension and solution thermal spray coatings," *Surf. Coat. Technol.,* vol. 203, no. 19, pp. 2807-2829, 2009.

[73] A. Ozturk and B. M. Cetegen, "Modeling of plasma assisted formation of precipitates in zirconium containing liquid precursor droplets," *Mater. Sci. Eng., A,* vol. 384, no. 1, pp. 331-351, 2004.

[74] R. Etchart-Salas, V. Rat, J. F. Coudert, P. Faurchais, N. Caron, K. Wittman and S. Alexandre, "Influence of plasma instabilies in ceramic suspension plasma spraying," *J. Therm. Spray Technol.,* vol. 16, no. 5, pp. 857-865, 2007.

[75] A. Ozturk and B. M. Cetegen, "Modeling of axially and transversely injected precursor droplets into a plasma environment," *Int. J. Heat Mass Transfer,* vol. 48, no. 21, pp. 4367-4383, 2005.

[76] M. D. Teicholz, The fabrication of dense, thick coatings using the solution precursor plasma spray process, Storrs CT: University of Connecticut Libraries, 2008.

[77] F. Tarasi, M. Medraj, A. Dolatabadi, J. Oberste-Berghaus and C. Moreau, "Effective parameters in axial injection suspension plasma spray process of alumina-zirconia ceramics," *J. Therm. Spray Technol.,* vol. 17, no. 5-6, pp. 685-691, 2008.

[78] D. Waldbillig and O. Kesler, "Characterization of metal-supported axial injection plasma sprayed solid oxide fuel cells with aqueous suspension plasma sprayed electrolyte layers," *J. Power Sources,* vol. 191, pp. 320-329, 2009.

[79] S. Basu, E. H. Jordan and B. M. Cetegen, "Fluid mechanics and heat transfer of liquid precursor droplets injected into high-temperature plasmas," *J. Therm. Spray Technol.,* vol. 17, no. 1, pp. 60-, 2008.

[80] C. Marchand, M. Vardelle, G. Mariaux and A. Vardelle, "Injection and aerodynamic fragmentation of liquid precursors under plasma spray conditions," in *2nd International workshop on Suspension and Solution Thermal Spraying*, Tours France, 2008.

[81] T. Bhatia, A. Ozturk, L. Xie, E. H. Jordan, B. M. Cetegen, M. Gell, X. Ma and N. P. Padture, "Mechansims of ceramic coating deposition in solution-precursor plasma spray," *J. Mater. Res.,* vol. 17, no. 9, pp. 2363-2372, 2002.

[82] A. Saha, S. Seal, B. M. Cetegen, E. H. Jordan, A. Ozturk and S. Basu, "Thermo-physical processes in cerium nitrate precursor droplets injected into high temperature plasma," *Surf. Coat. Technol.,* vol. 203, no. 15, pp. 2081-2091, 2009.

[83] M. C. Yuen and L. W. Chen, "On drag of evaporating liquid," *Combust. Sci. Technol.,* vol. 14, pp. 147-154, 1976.

[84] S. Basu and B. M. Cetegen, "Modeling of thermo-physical processes in liquid ceramic precursor droplets injected into a plasma jet," *Int. J. Heat Mass Transfer,* vol. 50, no. 17-18, pp. 3278-3290, 2007.

[85] E. Pfender, "Particle behavior in thermal plasmas," *Plasma Chem. Plasma Process.,* vol. 9, no. 1, pp. 167S-194S, 1989.

[86] C. Delbos, J. Fazilleau, V. Rat, J. F. Coudert, P. Fauchais and B. Pateyron, "Phenomena involved in suspension plasma spraying part 2: zirconia particle treatment and coating formation," *Plasma Chem. Plasma Process.,* vol. 26, no. 4, pp. 393-414, 2006.

[87] P. Fauchais, R. Etchart-Salas, V. Rat, J. F. Coudert, N. Caron and K. Wittmann-Teneze, "Parameters controlling liquid plasma spraying: solutions, sols, or suspensions," *J. Therm. Spray Technol.,* vol. 17, no. 1, pp. 31-59, 2008.

[88] K. VanEvery, M. J. Krane, R. W. Trice, H. Wang, W. Porter, M. Besser, D. Sordelet, J. Ilavsky and J. Almer, "Column formation in suspension plasma-sprayed coatings and resultant thermal properties," *J. Therm. Spray Technol.,* vol. 20, no. 4, pp. 817-828, 2011.

[89] H. Zhang, X. Y. Wang, L. L. Zheng and X. Y. Jiang, "Studies of splat morphology and rapid solidification during thermal spraying," *Int. J. Heat Mass Transfer,* vol. 44, no. 24, pp. 4579-4592, 2001.

[90] J. Cedelle, M. Vardelle and P. Fauchais, "Influence of stainless steel substrate preheating on surface topography and on millimeter- and micrometer-sized splat formation," *Surf. Coat. Technol.,* vol. 201, pp. 1373-1382, 2006.

[91] P. Fauchais, A. Vardelle, M. Vardelle and M. Fukumoto, "Knowledge concerning splat formation: an invited review," *J. Therm. Spray Technol.,* vol. 13, no. 3, pp. 337-360, 2004.

[92] L. Xie, X. Ma, E. H. Jordan, N. P. Padture, D. T. Xiao and M. Gell, "Identification of coating deposition mechanisms in the solution-precursor plasma-spray process using model spray experiments," *Mater. Sci. Eng., A,* vol. 362, no. 1, pp. 204-212, 2003.

[93] E. H. Jordan, L. Xie, X. Ma, N. P. Padture, B. Cetegen, A. Ozturk, J. Roth, T. D. Xiao and P. E. Bryant, "Superior thermal barrier coatings using solution precursor plasma spray," *J. Therm. Spray Technol.,* vol. 13, no. 1, pp. 57-65, 2004.

[94] A. Joulia, G. Bolelli, E. Gualtieri, L. Lusvarghi, S. Valeri, M. Varelle, S. Rossignol and A. Vardelle, "Comparing the deposition mechanisms in suspension plasma spray (SPS) and solution precursor plasma spray (SPPS) deposition of yttria-stabilized zirconia (YSZ)," *J. Eur. Ceram. Soc.,* vol. 34, no. 15, pp. 3925-3940, 2014.

[95] D. Chen, E. H. Jordan and M. Gell, "Effect of solution concentration on splat formation and coating microstructure using the solution precursor plasma spray process," *Surf. Coat. Technol.,* vol. 202, no. 10, pp. 2132-2138, 2008.

[96] L. Li, B. Kharas, H. Zhang and S. Sampath, "Suppression of crystallization during high velocity impact quenching of alumina droplets observations and characterization," *Mater. Sci. Eng., A,* vol. 456, no. 1, pp. 35-42, 2007.

[97] L. L. Shaw, D. Goberman, R. Ren, M. Gell, S. Jiang, Y. Wang, D. T. Xiao and P. R. Strutt, "The dependency of microstructure and properties of nanostructured coatings on plasma spray conditions," *Surf. Coat. Technol.,* vol. 130, no. 1, pp. 1-8, 2000.

[98] L. Xie, D. Chen, E. H. Jordan, A. Ozturk, F. Wu, X. Ma, B. M. Cetegen and M. Gell, "Formation of vertical cracks in solution-precursor plasma-sprayed thermal barrier coatings," *Surf. Coat. Technol.,* vol. 201, no. 3, pp. 1058-1064, 2006.

[99] E. H. Jordan, L. Xie, M. Gell, N. P. Padture, B. Cetegen, A. Ozturk, X. Ma, J. Roth, T. D. Xiao and P. E. Bryant, "Superior thermal barrier coatings using solution precursor plasma spray," *J. Therm. Spray Technol.,* vol. 13, no. 1, pp. 57-65, 2004.

[100] A. D. Jadhav, N. P. Padture, E. H. Jordan, M. Gell, P. Miranzo and E. R. Fuller Jr., "Low-thermal-conductivity plasma-sprayed thermal barrier coatings with engineered microstructures," *Acta Mater.,* vol. 54, no. 12, pp. 3343-3349, 2006.

[101] N. P. Padture, K. W. Schlichting, T. Bhatia, A. Ozturk, B. Cetegen, E. H. Jordan, M. Gell, S. Jiang, T. D. Xiao, P. R. Strutt, E. Garcia, P. Miranzo and M. I. Osendi, "Towards durable thermal barrier coatings with novel microstructures deposited by solution-precursor plasma spray," *Acta Mater.,* vol. 49, no. 12, pp. 2251-2257, 2001.

[102] X. Ma, F. Wu, J. Roth, M. Gell and E. H. Jordan, "Low thermal conductivity thermal barrier coatings deposited by the solution plasma spray process," *Surf. Coat. Technol.,* vol. 201, no. 7, pp. 4447-4452, 2006.

[103] M. Gell, L. Xie, E. H. Jordan and N. P. Padture, "Mechanisms of spallation of solution precursor plasma spray thermal barrier coatings," *Surf. Coat. Technol.,* vol. 188, pp. 101-106, 2004.

[104] M. Gell, L. Xie, X. Ma, E. H. Jordan and N. P. Padture, "Highly durable thermal barrier coatings made by the solution precursor plasma spray process," *Surf. Coat. Technol.,* vol. 177, pp. 97-102, 2004.

[105] L. Xie, E. H. Jordan, N. P. Padture and M. Gell, "Phase and microstructural stability of solution precursor plasma sprayed thermal barrier coatings," *Mater. Sci. Eng., A,* vol. 381, no. 1, pp. 189-195, 2004.

[106] D. Chen, M. Gell, E. H. Jordan, E. Cao and X. Ma, "Thermal stability of air plasma spray and solution precursor plasma spray thermal barrier coatings," *J. Am. Ceram. Soc.,* vol. 90, no. 10, pp. 3160-3166, 2007.

[107] A. D. Jadhav and N. P. Padture, "Mechanical properties of solution-precursor plasma-sprayed thermal barrier coatings," *Surf. Coat. Technol.,* vol. 202, no. 20, pp. 4976-4979, 2008.

[108] D. Chen, E. H. Jordan, M. Gell and M. Xingqi, "Dense TiO_2 coating using the solution precursor plasma spray process," *J. Am. Ceram. Soc.,* vol. 91, no. 3, pp. 865-872, 2008.

[109] D. Chen, E. H. Jordan and M. Gell, "Porous TiO_2 coating using the solution precursor plasma spray process," *Surf. Coat. Technol.,* vol. 202, no. 24, pp. 6113 - 6119, 2008.

[110] W. Z. Wang, T. Coyle and D. Zhao, "Preparation of Lanthanum Zirconate Coatings by the Solution Precursor Plasma Spray," *J. Therm. Spray Technol.,* vol. 23, no. 5, pp. 827 - 832, 2014.

[111] D. Chen, E. H. Jordan, M. W. Renfro and M. Gell, "Dy:YAG Phosphor Coating Using the Solution Precursor Plasma Spray Process," *J. Am. Ceram. Soc.,* vol. 92, no. 1, pp. 286-271, 2009.

[112] D. Chen, E. H. Jordan, M. W. Renfro and M. Gell, "Solution Precursor Plasma Spray Eu: Y_2O_3 Phosphor Coating," *Int. J. Appl. Ceram. Technol.,* vol. 9, no. 3, pp. 636 - 641, 2012.

[113] Y. Wang and T. W. Coyle, "Solution precursor plasma spray of porous $La_{1-x}Sr_xMnO_3$ perovskite coatings for SOFC cathode application," *J. Fuel Cell Sci. Technol.,* vol. 8, no. 2, p. 021005, 2010.

[114] Y. Wang and T. W. Coyle, "Solution Precursor Plasma Spray of Nickel-Yittia Stabilized Zirconia Anodes for Solid Oxide Fuel Cell Application," *J. Therm. Spray Technol.,* vol. 16, no. 5, pp. 898-904, 2007.

[115] M. Gell, F. Wu, E. H. Jordan, N. P. Padture, B. M. Cetegen, L. Xie, A. Ozturk, E. Cao, A. Jadhav and X. Ma, "The solution precursor plasma spray process for making highly durable thermal barrier coatings," in *ASME Turbo Expo 2005: Power for Land, Sea, and Air (GT2005)*, Reno Nevada, 2005.

[116] R. M. Leckie, S. Kraemer, M. Ruhle and C. G. Levi, "Thermochemical compatibility between alumina and ZrO_2-$GdO_{3/2}$ thermal barrier coatings," *Acta Mater.,* vol. 53, no. 11, pp. 3281-3292, 2005.

[117] J. Wu, N. P. Padture and M. Gell, "High-temperature chemical stability of low thermal conductivity ZrO_2-$GdO_{1.5}$ thermal barrier ceramics in contact with α-Al_2O_3," *Scr. Mater.,* vol. 50, pp. 1315-1318, 2004.

[118] W. Braue, "Environmental stability of the YSZ layer and the YSZ/TGO interface of an in-service EB-PVD coated high-pressure turbine blade," *J. Mater. Sci.,* vol. 44, no. 7, pp. 1664-1675, 2009.

[119] J. M. Drexler, C.-H. Chen, A. D. Glenhill, K. Shinoda, S. Sampath and N. P. Padture, "Plasma sprayed gadolinium zirconate thermal barrier coatings that are resistant to damage by molten Ca-Mg-Al-silicate glass," *Surf. Coat. Technol.,* vol. 206, no. 19-20, pp. 3911-3916, 2012.

[120] A. Bolcavage, A. Feuerstein, J. Foster and P. Moore, "Thermal shock testing of thermal barrier coating/bondcoat systems," *J. Mater. Eng. Perform.,* vol. 13, no. 4, pp. 389-397, 2004.

[121] T. Steinke, D. Sebold, D. E. Mack, R. Vassen and D. Stover, "A novel test approach for plasma-sprayed coatings tested simultaneously under CMAS and thermal gradient cycling conditions," *Surf. Coat. Technol.,* vol. 205, no. 7, pp. 2287-2295, 2010.

[122] E. H. Jordan, C. Jiang, J. Roth and M. Gell, "Low thermal conductivity yttria-stabilized zirconia thermal barrier coatings using the solution precursor plasma spray process," *J. Therm. Spray Technol.,* vol. 23, no. 5, pp. 849-859, 2014.

[123] R. E. Taylor, "Thermal conductivity determination of thermal barrier coatings," *Mater. Sci. Eng., A,* vol. 245, no. 2, pp. 160-167, 1998.

[124] B. Borawski, J. Singh, J. A. Todd and D. E. Wolfe, "Multi-layer coating design architecture for optimum particulate erosion resistance," *Wear,* vol. 271, no. 11, pp. 2782-2792, 2011.

[125] D. E. Wolfe, B. M. Gabriel and M. W. Reedy, "Nanolayer (Ti,Cr)N coatings for hard particle erosion resistance," *Surf. Coat. Technol.,* vol. 205, no. 19, pp. 4569-4576, 2011.

[126] ASTM C633-13, "Standard test method for adhesion or cohesion strength of thermal spray coatings," ASTM International, West Conshohocken, PA, 2013.

[127] F. Wu, E. H. Jordan, X. Ma and M. Gell, "Thermally grown oxide growth behavior and spallation lives of solution precursor plasma spray thermal barrier coatings," *Surf. Coat. Technol.,* vol. 202,

no. 9, pp. 1628-1635, 2008.

[128] J. R. Davis, "Environmental stability: bond coat stability," in *Handbook of Thermal Spray Technology*, Materials Park, ASM International, 2004, p. 270.

[129] R. Wellman, G. Whitman and J. R. Nicholls, "CMAS corrosion of EB-PVD TBCs: identifying the minimum level to initiate damage," *Int. J. Refract. Met. Hard Mater.,* vol. 28, no. 1, pp. 124-132, 2010.

[130] W. Zhao and B. Gleeson, "Steam effects on the oxidation behavior of Al_2O_3-scale forming Ni-based alloys," *Oxid. Met.,* vol. 79, no. 5, pp. 613-625, 2013.

[131] R. Rampon, O. Marchand, C. Filiatre and G. Bertrand, "Influence of suspension characteristics on coatings microstructure obtained by suspension plasma spraying," *Surf. Coat. Technol.,* vol. 202, no. 18, pp. 4337-4342, 2008.

[132] S. A. Langer, E. R. Fuller Jr. and W. C. Carter, "OOF: an image-based finite-element analysis of material microstructures," *Comput. Sci. Eng.,* vol. 3, no. 3, pp. 15-23, 2001.

[133] L. Xie, X. Ma, A. Ozturk, E. H. Jordan, N. P. Padture, B. M. Cetegen, D. T. Xiao and M. Gell, "Processing parameter effects on solution precursor plasma spray patterns," *Surf. Coat. Technol.,* vol. 183, pp. 51-61, 2004.

[134] M. P. Bacos, J. M. Dorvaux, S. Landais, O. Lavigne, R. Mevrel, M. Poulain, C. Rio and M. H. Vidal-Setif, "10-Year-Activities at Onera on Advanced Thermal Barrier Coatings," *Aerospace Lab Journal,* Vols. AL 03-04, no. 3, pp. 1-14, 2011.

[135] W. J. Parker, R. J. Jenkins, C. P. Butler and G. L. Abbott, "Flash method of determining thermal diffusivity, heat capacity and thermal conductivity," *J. Appl. Phys.,* vol. 32, no. 9, pp. 1679-1984, 1961.

[136] H. S. Carslaw and J. C. Jaeger, Conduction of heat in solids, New York: Oxford University Press, 1959.

[137] Y. Tan, J. P. Longtin, S. Sampath and D. Zhu, "Temperature-gradient effects in thermal barrier coatings: an investigation through modeling, high heat flex test and embedded sensor," *J. Am. Ceram. Soc.,* vol. 93, no. 10, pp. 3418-3426, 2010.

[138] C. K. Muoto, E. H. Jordan, M. Gell and M. Aindow, "Effects of precursor chemistry on the structural characteristics ofY_2O_3-MgO nanocomposites synthesized by a combined sol-gel/thermal decomposition route," *J. Am. Ceram. Soc.,* vol. 94, no. 2, p. 372–381, 2011.

[139] S. R. Jain, K. C. Adiga and V. R. Pai Verneker, "A new approach to thermochemical calculations of condensed fuel-oxidizer mixtures," *Combust. Flame,* vol. 40, no. C, pp. 71-79, 1981.

[140] D. Lee, T. W. Kim and K. S. Lee, "Design of thermal barrier coatings using gadolinium zirconate ceramis: a study on gadolinium zirconate/YSZ bilayers," *J. Ceram. Soc. Jpn.,* vol. 117, no. 5, pp. 550-554, 2009.

[141] D. R. Clarke and S. R. Phillpot, "Thermal barrier coating materials," *Mater. Today,* vol. 8, no. 6, pp. 22-29, 2005.

[142] E. Bakan, D. E. Mack, G. Mauer and R. Vassen, "Gadolinium zirconate/YSZ thermal barrier coatings: plasma spraying, microstructure, and thermal cycling behavior," *J. Am. Ceram. Soc.,* vol.

97, no. 12, pp. 4045-4051, 2014.

[143] L. Bianchi, A. C. Leger, M. Vardelle, A. Vardelle and P. Fauchais, "Splat formation and cooling of plasma-sprayed zirconia," *Thin Solid Films,* vol. 305, no. 1, pp. 35-47, 1997.

[144] A. U. Munawar, U. Schulz, G. Cerri and H. Lau, "Microstructure and cyclic lifetime of Gd and Dy-containing EB-PVD TBCs deposited as single and double-layer on various bond coats," *Surf. Coat. Technol.,* vol. 245, pp. 92-101, 2014.

[145] A. L. Vasiliev and N. P. Padture, "Coatings of metastable ceramics deposited by solution-precursro plasma spray: II. ternary ZrO_2-Y_2O_3-Al_2O_3 system," *Acta Mater.,* vol. 54, no. 18, pp. 4921-4928, 2006.

[146] D. Chen, E. H. Jordan, M. Gell and X. Ma, "Dense alumina-zirconia coatings using the solution precursor plasma spray process," *J. Am. Ceram. Soc.,* vol. 91, no. 2, pp. 359-365, 2008.

[147] C. Tekmen, Y. Tsunekawa and M. Okumiya, "Effect of plasma spray parameters on in-flight particle characteristics and in-situ alumina formation," *Surf. Coat. Technol.,* vol. 203, no. 3, pp. 223-228, 2008.

[148] N. Sanpo, J. Wang, A. S. M. Ang and C. C. Berndt, "Influence of the different organic chelating agents on the topography, physical properties and phase of SPPS-deposited spinel ferrite splats," *Appl. Surf. Sci.,* vol. 8, pp. 171-178, 2013.

[149] S. M. Lakiza and L. M. Lopato, "Stable and metastable phase relations in the system Alumina-Zirconia-Yttria," *J. Am. Ceram. Soc.,* vol. 80, no. 4, pp. 893-902, 1997.

[150] B. S. Senturk, H. F. Garces, A. L. Ortiz, G. Dwivedi, S. Sampath and N. P. Padture, "CMAS-Resistant Plasma Sprayed Thermal Barrier Coatings Based on Y_2O_3-Stabilized ZrO_2 with Al^{3+} and Ti^{4+} Solute Additions," *J. Therm. Spray Technol.,* vol. 23, no. 4, pp. 708 - 715, 2014.

[151] W. Braue and P. Mechnich, "Recession of an EB-PVD YSZ coated turbine blade by $CaSO_4$ and Fe, Ti-rich CMAS-type deposits," *J. Am. Ceram. Soc.,* vol. 94, no. 12, pp. 4483-4489, 2011.

[152] J. Knuuttila, P. Sorsa and T. Mantyla, "Sealing of thermal spray coatings by impregnation," *J. Therm. Spray Technol.,* vol. 8, no. 2, pp. 249-257, 1999.

[153] E. S. Newman, "Behavior of calcium sulfate at high temperatures," *J. Res. Natl. Bur. Stand.,* vol. 27, pp. 191-196, 1941.

[154] H. Du, "Thermodynamic assessment of the K_2SO_4-Na_2SO_4-$MgSO_4$-$CaSO_4$ system," *J. Phase Equilib.,* vol. 21, no. 1, pp. 6-18, 2000.

[155] J. L. Smialek, F. A. Archer and R. G. Garlick, "Turbine airfoil degradation in the Persian Gulf War," *JOM [H.W. Wilson - AST],* vol. 46, p. 39, 1994.

[156] M. P. Borom, C. A. Johnson and L. A. Peluso, "Role of environmental deposits and operating surface temperatures in spallation of air plasma sprayed thermal barrier coatings," *Surf. Coat. Technol.,* Vols. 86-87, no. Part 1, pp. 116-126, 1996.

[157] J. M. Drexler, A. D. Gledhill, K. Shinoda, A. L. Vasiliev, K. M. Reddy, S. Sampath and N. P. Padture, "Jet engine coatings for resisting volcanic ash damage," *Adv. Mater.,* vol. 23, no. 21, pp. 2419-2424, 2011.

[158] A. R. Krause, H. F. Garces, B. S. Senturk, N. P. Padture and D. J. Green, "$2ZrO_2 \cdot Y_2O_3$ thermal

barrier coatings resistant to degradation by molten CMAS: part II, interactions with sand and fly ash," *J. Am. Ceram. Soc.,* vol. 97, no. 12, pp. 3950 - 3957, 2014.

[159] H. E. Taylor and F. E. Lichte, "Chemical composition of Mount St. Helens volcanic ash," *Geophys. Res. Lett.,* vol. 7, no. 11, pp. 949-952, 1980.

[160] W. Chesner, R. Collins, M. MacKay and J. Emery, "User guidelines for waste and byproduct materials in pavement construction," Federal Highway Administration, McLean VA, 1999.

[161] A. K. Rai, R. S. Bhattacharya, D. E. Wolfe and T. J. Eden, "CMAS-Resistant Thermal Barrier Coatings," *Int. J. Appl. Ceram. Technol.,* vol. 7, no. 5, pp. 662-674, 2010.

[162] R. Srinivasan, R. J. De Angelis, G. Ice and B. Davis, "Identification of tetragonal and cubic structures of zirconia using synchrotron x-radiation source," *J. Mater. Res.,* vol. 6, no. 6, pp. 1287-1292, 1991.

[163] J. Chevalier, L. Gremillard, A. V. Virkar and D. R. Clarke, "The tetragonal-monoclinic transformation in zirconia: lesson learned and future trends," *J. Am. Ceram. Soc.,* vol. 92, no. 9, pp. 1901-1920, 2009.

[164] J. Ilavsky, J. K. Stalick and J. Wallace, "Thermal spray yttria-stabilized zirconia phase changes during annealing," *J. Therm. Spray Technol.,* vol. 10, no. 3, pp. 497-501, 2001.

[165] T. Tarasi, M. Medraj, A. Dolatabadi, J. Oberste-Berghaus and C. Moreau, "Phase formation and transformation in alumina/YSZ nanocomposite coating deposited by suspension plasma spray process," *J. Therm. Spray Technol.,* vol. 19, no. 4, pp. 787-795, 2010.

[166] S. Nazarpour, C. Lopez-Gandara, C. Zamani, J. M. Fernandez-Sanjuan, F. M. Ramos and A. Cirera, "Phase transformation studies on YSZ doped with alumina. Part 2: yttria segregation," *J. Alloys Compd.,* vol. 505, no. 2, pp. 534-541, 2010.

[167] A. A. Bokov and A. V. Nikonov, "Formation mechanism of monoclinic ZrO_2 at the contact of YSZ with CuO," *Inorg. Mater.,* vol. 51, no. 6, pp. 553-558, 2015.

[168] O. Bikonadoa, C. L. Pang, R. Ithnin, C. A. Muryn, H. Onishi and G. Thornton, "Direct visualization of defect-mediated dissociation of water on TiO_2(110)," *Nat. Mater.,* vol. 5, no. 3, pp. 189-192, 2006.

[169] D. Chen, E. H. Jordan and M. Gell, "Effect of solution concentration on splat formation and coating microstructure using the solution precursor plasma spray process," *Surf. Coat. Technol.,* vol. 202, no. 10, pp. 2132-2138, 2008.